

# Analytical Solution for Low-Thrust Transfer Orbits using Bang-Bang Control without Gravity Losses

Livia Ionescu  
June 13, 2019

Delft University of Technology

Cover image: Low-thrust trajectory. Artistic style transfer with Composition VIII by Wassily Kandinsky (1923). Rendered with <https://deepart.io/>

# Analytical Solution for Low-Thrust Transfer Orbits using Bang-Bang Control without Gravity Losses

by

**Livia Ionescu**

in partial fulfillment of the requirements for the degree of

**Master of Science**  
in Aerospace Engineering

at Delft University of Technology,  
to be defended publicly on Thursday June 13, 2019 at 2:00 PM.

Supervisor: Ir. R. Noomen  
Thesis committee: Dr. ir. E.J.O. Schrama  
Ir. R. Noomen  
Dr. J.L.A. Dubbeldam

An electronic version of this thesis is available at <http://repository.tudelft.nl/>.



# Preface

The ever expanding universe is a driving force for curious and inquisitive engineers to keep discovering new things about it from fresh perspectives. Through solid research, improvements in space technology are continuously made possible. This thesis seeks to improve the efficiency of the optimization process for orbit transfers by offering an analytical solution for low thrust transfer orbits. In addition, two constraints are set on the thrust acceleration. Firstly, only bang-bang control is allowed for the thrust profile. Secondly, no radial thrust acceleration is allowed. The proposed model is believed to provide good first-order estimates to accelerate the search for an optimal solution.

First of all, I would like to thank my supervisor Ron Noomen for his endless patience, motivating words and advice and guidance throughout the research process. I am extremely grateful for the way he always challenged my points of view on the topic and his support truly helped me to finish my thesis in its current state. Secondly, I am thankful to Dominic Dirx for his technical support whenever I had questions about the TU Delft open source software Tudat. I would also like to thank Ernst Schrama and Johan Dubbeldam for being part of my defence committee.

Lastly, I would like to thank my family and friends. My family, for all the love and support they have given me during this journey in my life. My friends, for getting me through all the difficulties I encountered and making my studies a true delight. Without you, this thesis work would not have been possible.

*Livia Ionescu  
Delft, June 2019*



# Summary

This thesis research has focused on developing an analytical solution for low-thrust transfer orbits. Low-thrust propulsion is an attractive option for space manoeuvres and transfers, since it provides a large specific impulse and hence efficient use of propellant. Thus, the propellant mass can be decreased, which brings advantages such as higher payload mass and extended mission life.

Two constraints have been posed on the thrust acceleration, which often appear as a result of optimal solutions. Firstly, only bang-bang control is allowed, thus the rocket engine can only be turned on or off. Secondly, no radial thrust is allowed, such that no gravity losses occur.

To describe the trajectory, three different sets of coordinates have been considered, namely spherical coordinates, Kepler orbital elements and modified equinoctial elements. The latter set was chosen, as it excludes singularities at zero eccentricity and zero inclination and offers a system of first-order differential equations. To simplify the dynamics, no perturbations other than the thrust force have been assumed to act on the spacecraft. This assumption is valid if the thrust acceleration is not too small. Furthermore, circular orbits have been assumed. That is, the eccentricity of the orbit is set to zero. While this seems as a substantial restriction on the developed method, it is shown that the analytical solution provides very reasonable results for eccentricities smaller than 0.2.

Analytical solutions have been derived with both the true longitude and time as independent variable. However, the time-based analytical solutions provided better results, thus these have been selected for further analysis. An attempt has been made to improve the analytical solutions by adding some additional assumptions (some variables were allowed to vary and more parameters were used), but these did not yield better results. Furthermore, separate analytical expressions have been developed when no in-plane thrust acts on the spacecraft. The original analytical derivations contained a singularity for this case, and thus did not allow a solution.

For the implementation of the bang-bang control, each individual revolution around the central body is allowed to have two thrust arcs and two coasts arcs, where the analytical solutions have been used to describe the motion of the spacecraft during the thrust arcs. By cleverly choosing the switching points where the rocket engine is turned on and off, the transfer orbit is achieved in an efficient way.

The performance of the developed algorithm has been assessed for different input parameters. More specifically, different magnitudes of thrust accelerations have been analyzed. Furthermore, the lengths of the thrust and coast arcs, together with the direction of the thrust force, have been varied to evaluate the applicability of the algorithm. Lastly, the algorithm has been tested with the introduction of a stop criterion, which determines the required propellant and time of flight to arrive at a set target element.

The algorithm has proved to give results with relatively good accuracy for orbits with an eccentricity smaller than 0.2. For example, if a case is considered with a thrust acceleration of  $10^{-4}$  m/s<sup>2</sup> and an transfer time of 10 years, the average result in the semi-major axis is approximately 0.65%. Also the results for the inclination show a small difference of 0.17 degrees on average. The difference in eccentricity is 0.006, which can be neglected for first-order estimates. Also the results of the longitude of the ascending node and the argument of latitude show good accuracies. However, if the time of flight becomes excessively large (i.e. beyond 10-20 years), the algorithm is not able to provide a solution within reasonable errors. Also, should the thrust acceleration become too high (e.g.  $10^{-3}$  m/s<sup>2</sup>), the inaccuracies of the results increase. These larger inaccuracies are due to the eccentricity, which then increases more rapidly and reaches the given limit faster. Finally, the developed method seems unfit to determine the argument of periapsis.

The developed algorithm has only been tested for transfers on the Solar System scale (i.e. heliocentric orbit). A recommendation for future work would be to extend this analysis to geocentric orbits. Furthermore, the algorithm could be used in an optimization process. Then, the parameters for the transfer orbit could be determined and an optimal trajectory could be achieved.

# Contents

<b>Preface</b>	<b>iii</b>
<b>Summary</b>	<b>vi</b>
<b>List of Abbreviations</b>	<b>1</b>
<b>List of Symbols</b>	<b>3</b>
<b>1 Introduction</b>	<b>5</b>
<b>2 Heritage</b>	<b>7</b>
2.1 Shape-Based Methods . . . . .	7
2.2 Gravity Losses . . . . .	15
2.3 Bang-Bang Control . . . . .	16
<b>3 Astrodynamics</b>	<b>21</b>
3.1 Perturbing Accelerations . . . . .	21
3.2 Equations of Motion . . . . .	23
<b>4 Analytical Solution using True Longitude</b>	<b>29</b>
4.1 General Solution . . . . .	29
4.2 Special Functions: Sine and Cosine Integral . . . . .	31
4.3 Tuning the Numerical Integrator . . . . .	34
4.4 Results and Discussion . . . . .	36
<b>5 Analytical Solution using Time</b>	<b>43</b>
5.1 General Solution . . . . .	43
5.2 Thrust Perpendicular to the Orbital Plane . . . . .	45
5.3 Results and Discussion . . . . .	46
5.4 Variations . . . . .	54
<b>6 Algorithm Development</b>	<b>59</b>
6.1 Bang-Bang Control . . . . .	59
6.2 Results and Discussion . . . . .	62
<b>7 Performance Assessment</b>	<b>65</b>
7.1 Fixed Time Periods . . . . .	65
7.2 Stop Criterion . . . . .	70
<b>8 Conclusions and Recommendations</b>	<b>79</b>
8.1 Conclusions . . . . .	79
8.2 Recommendations . . . . .	80
<b>Bibliography</b>	<b>81</b>



# List of Abbreviations

AU	Astronomical Unit
DITAN	Direct Interplanetary Trajectory Analysis
DU	Distance Unit
EoM	Equation of Motion
ESA	European Space Agency
FFS	Finite Fourier Series
GEO	Geostationary Earth Orbit
GOCE	Gravity Field and Steady-State Ocean Circulation Explorer
LEO	Low Earth Orbit
MPD	Magnetoplasmadynamic
NASA	National Aeronautics and Space Administration
OSCAR-40	Orbiting Satellite Carrying Amateur Radio-40
PPT	Pulsed Plasma Thruster
SFU	Space Flyer Unit
SMART-1	Small Missions for Advanced Research in Technology-1
TET-1	Technologie Erprobungs Träger-1
TOF	Time Of Flight
TU	Time Unit
Tudat	TU Delft Astrodynamics Toolbox



# List of Symbols

## Latin

<i>Symbol</i>	<i>Meaning</i>	<i>Unit</i>
$a$	Semi-major axis	m
$a_p$	Propulsive acceleration	$m/s^2$
$e$	Eccentricity	-
$f_N$	Thrust acceleration in transverse direction	$m/s^2$
$f_S$	Thrust acceleration in radial direction	$m/s^2$
$f_{tot}$	Total thrust acceleration	$m/s^2$
$f_W$	Thrust acceleration perpendicular to orbital plane	$m/s^2$
$f$	Modified equinoctial element	-
$F$	Force	N
$g$	Modified equinoctial element	-
$g_0$	Standard gravitational acceleration at sea-level	$m/s^2$
$h$	Modified equinoctial element	-
$i$	Inclination	deg
$I_{sp}$	Specific impulse	s
$k$	Modified equinoctial element	-
$L$	True longitude	deg
$\dot{m}$	Mass flow	kg/s
$M_0$	Initial mass	kg
$M_f$	Final mass	kg
$p$	Semi-latus rectum	m
$r$	Radial distance	m
$t$	Time	s
$T_a$	Thrust acceleration	$m/s^2$
$\tau_{aa}$	Thrust arc angle	deg
$u$	Argument of latitude	deg
$u$	Thrust acceleration	$m/s^2$
$V_j$	Exhaust velocity	m/s
$x$	First component of the Cartesian coordinates	m
$y$	Second component of the Cartesian coordinates	m
$z$	Third component of the Cartesian coordinates	m
$z$	Third component of the cylindrical coordinates	m

## Greek

<i>Symbol</i>	<i>Meaning</i>	<i>Unit</i>
$\alpha$	Steering angle	deg
$\gamma$	Flight path angle	deg
$\theta$	Polar angle (polar coordinates)	deg
$\theta$	Azimuth angle (spherical coordinates)	deg
$\theta$	True anomaly	deg
$\mu$	Gravitational parameter	$m^3/s^2$
$\phi$	Polar angle (spherical coordinates)	deg
$\Omega$	Longitude of the ascending node	deg
$\omega$	Argument of pericenter	deg



# 1

## Introduction

Low-thrust electric propulsion has acquired an increased interest in recent years. An advantages of this type of propulsion when compared to high-thrust propulsion, is the very high specific impulse, reducing the required propellant for a transfer trajectory. Thus, apart from the fact that more payload can be taken aboard, the mission lifetime can also be extended and the launch can be cheaper [1].

Already in 1911, Tsiolkovsky mentioned in a publication the large exhaust velocities that could be achieved by electrons in cathode rays [2]. Also Goddard described the use of cathode rays for electric propulsion in his notes at an even earlier date in 1906 [2]. However, the first mission using electric propulsion for major manoeuvres, although using ions instead of electrons, did not fly until 1998, when the National Aeronautics and Space Administration (NASA) launched the Deep Space 1 mission [2]. Other missions followed, such as Small Missions for Advanced Research in Technology-1 (SMART-1), Gravity Field and Steady-State Ocean Circulation Explorer (GOCE) and Bepi Colombo launched by the European Space Agency (ESA). However, low-thrust propulsion also comes with a disadvantage. Since only a small acceleration force is applied on the spacecraft, more time is required to perform the desired orbit change. Differently from chemical propulsion, the effect of which can be modelled as instantaneous changes in velocity, low-thrust propulsion has to be continuously active in order to obtain the required impulse change. Impulsive thrusting assumes two impulses at the start and end of the transfer orbit, while the transfer orbit itself is modelled as a Kepler orbit. This is easy to propagate as the elements remain constant. Thus, only two thrust vectors have to be optimized. Low-thrust continuous thrusting requires the thrust vectors at each instance in time [3]. This makes the optimization more challenging, as no comprehensive analytical expression is available to model the trajectory.

The aim of this thesis research is to investigate an analytical solution for low-thrust transfer orbits. It is assumed that no exact solution will be found, thus the resulting expression would only offer a first-order estimate of the transfer trajectory. However, such first-order estimates prove to be useful for preliminary mission design and subsequent more accurate numerical optimization processes, which need a good initial guess in order to converge (within reasonable time). From these high-accuracy optimizations, it is known that optimal solutions often include bang-bang control, i.e. the rocket engine is either on or off, and zero radial accelerations, to reduce gravity losses. These two constraints on the thrust acceleration will be directly implemented in the developed method, in an attempt to arrive faster and more efficiently at the optimal solution. Also, the resulting transfer orbit is expected to lie closer to the true optimum. Considering the discussion above, the research question can be formulated as:

*Is it possible to develop an analytical solution for low-thrust trajectories while assuming bang-bang control without gravity losses?*

From this research question, two sub-questions can be formulated:

- *What is the accuracy of the developed solution?*
- *To what extent is the developed solution applicable?*

This report is structured as follows. Chapter 2 describes previous work done on analytical expressions for low-thrust orbits, bang-bang control and gravity losses. Secondly, the astrodynamics of the problem and the chosen set of coordinates are discussed in Chapter 3. The next two chapters are dedicated to finding the analytical solutions. While Chapter 4 derives the equations with respect to true longitude, Chapter 5 uses time as the independent variable. Next, the development of the algorithm is explained in Chapter 6, where the bang-bang control thrust profile is implemented. Then, the performance of the developed method is assessed in Chapter 7. Note that the newly developed algorithm is not applied in a mission design environment yet. In Chapter 8, conclusions are drawn and recommendations are made for future work.

# 2

## Heritage

Low-thrust transfer orbits are particularly more difficult to optimize than transfer orbits induced by a short, high-impulse thrust force from the engine. While for the latter it can be assumed that the thrust force is applied instantaneously, such that the transfer orbit itself is by a first-order estimation a Kepler orbit, low-thrust propulsion continuously provides a thrusting force on the spacecraft, making the dynamics more complicated and finding optimal solutions more difficult.

The aim of this thesis project is to develop an optimization method that efficiently delivers a first-order estimate of a low-thrust transfer orbit. For an efficient optimization process, an analytical solution of the Equations of Motion (EoMs) is attractive. Without the need for a computationally expensive numerical integration of the satellite's position in orbit, the transfer orbit can be optimized more quickly. Furthermore, bang-bang control will be used exclusively and the radial thrust force will be eliminated.

Analytical solution for low-thrust transfers have been studied before. So-called shape-based methods assume the orbit to have a certain shape, which is given by an analytical expression. An optimization process then determines the parameters to comply with certain mission requirements (e.g. departure and target orbit, total transfer time etc.). Various shape-based methods have been developed. An overview is given in Section 2.1. Transfer orbits without radial thrust have also been a subject of study before. Section 2.2 elaborates on one such study, which arrives at an analytical solution for two-dimensional orbits. Finally, also bang-bang control has been used in combination with low-thrust transfers before. Frequently this is achieved with Lawden's primer vector theory. An example is shown in Section 2.3.

### 2.1. Shape-Based Methods

Multiple shape-based methods have been developed over the years. A short overview of the most important characteristics is given in Table 2.1. The inverse polynomials shaping method has been originally developed for two-dimensional cases, and was later extended to three dimensions. Hereafter, each method is discussed briefly.

Table 2.1: Comparison of the various shape-based methods.

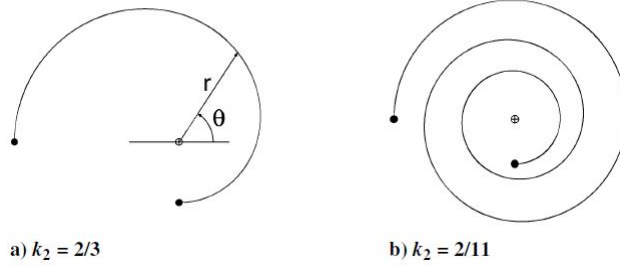
Method	Assumed thrust direction	Thrust constraint	Dimensions	Ref.
Exposins	Tangential	None	2	[4]
Pseudo-equinoctial elements	None	Maximum thrust acceleration limit	3	[5]
Inverse polynomials	Tangential	None	2 or 3	[6] [7]
Spherical shaping	None	None	3	[8]
Finite Fourier series	Tangential	Maximum allowed value is limited, approximate on-off thrusting can be achieved	2	[9] [10] [11]
Hodographic shaping	None	Thrust acceleration can be limited but is not done in the paper	3	[12]

### Exponential Sinusoids

The very first shape-based method was introduced by Petropoulos and Longuski in [4], which was based on the PhD dissertation of Petropoulos [13]. A computational implementation of this method was given in a succeeding paper [14]. Petropoulos assumed that the shape of the trajectory could be represented by an exponential sinusoid, or exposin. This shaping function is shown in Equation 2.1.

$$r = k_0 e^{k_1 \sin(k_2 \theta + \phi)} \quad (2.1)$$

In the above equation  $r$  and  $\theta$  are the radial distance and polar angle as defined for the polar coordinates and  $k_0, k_1, k_2$  and  $\phi$  are constants. Examples of the sinusoidal shape for two values of  $k_2$  are shown in Figure 2.1.

Figure 2.1: Example of the exposin shape for two different values of  $k_2$  [14].

This shape function forms a convenient basis to solve for the EoMs expressed in polar coordinates, as shown in Equations 2.2 and 2.3.

$$\ddot{r} - r\dot{\theta}^2 + \frac{\mu}{r^2} = F \sin(\alpha) \quad (2.2)$$

$$\frac{1}{r} \frac{d}{dt}(r^2 \dot{\theta}) = F \cos(\alpha) \quad (2.3)$$

In the above equations,  $F$  represent the thrust acceleration, while  $\alpha$  defines the angle of the thrust with respect to the local horizon.  $\mu$  is the gravitational parameter of the main attracting body and  $r$  is the radial distance.

If the thrust acceleration is assumed to point in the tangential direction (along or opposite to the velocity vector), the EoMs can be solved to find an expression for the angular rate and normalized thrust acceleration as a function of the shaping parameters  $k_1, k_2$  and  $k_3$ . These are shown in Equations 2.4 and 2.5.

$$\dot{\theta}^2 = \left(\frac{\mu}{r^3}\right) \frac{1}{\tan^2(\gamma) + k_1 k_2^2 s + 1} \quad (2.4)$$

$$a = \frac{(-1)^n \tan \gamma}{2 \cos \gamma} \left[ \frac{1}{\tan^2 \gamma + k_1 k_2^2 s + 1} - \frac{k_2^2 (1 - 2k_1 s)}{(\tan^2 \gamma + k_1 k_2^2 s + 1)^2} \right] \quad (2.5)$$

with,

$$s = \sin(k_2 \theta + \phi) \quad (2.6)$$

Also, the flight path angle can be expressed as in Equation 2.7.

$$\tan(\gamma) = k_1 k_2 \cos(k_2 \theta + \phi) \quad (2.7)$$

The additional constraint  $|k_1 k_2^2| < 1$  excludes unfeasible solutions. However, with the current method, the TOF constraint can only be achieved by forward targeting. Izzo [15] used the exposins to solve Lambert's problem. A reduction in free variables was achieved by fixing  $k_2$ . Also, the free variable  $\phi$  is changed to the initial flight path angle  $\gamma_1$  using Equation 2.7 (with  $\theta_1 = 0$ ). If the parameters  $k_1$  and  $k_2$  are used to satisfy the initial and final positions, then the last free parameter  $\gamma_1$  can be used to satisfy the TOF constraint. The range of the search space for  $\gamma_1$  is given by the additional constraint for  $k_1$  and  $k_2$  as discussed above. Then, when the number of revolutions is chosen, the three parameters can be computed to satisfy the three boundary conditions. A drawback of this shape-based method is that no constraints on the maximum thrust acceleration can be set, which can result in unfeasible thrust profiles. Also, the method is limited to planar problems (although a patch was introduced later, but with errors).

### Pseudo-Equinoctial Elements

Rather than shaping the radius of the spacecraft during the transfer, as done with the exponential sinusoids, the orbital elements can be shaped. De Pascale and Vasile [5] used the modified equinoctial elements (see Chapter 3) as the basis for their shaping functions. The advantage of using orbital elements is that the problem is automatically defined in three dimensions, thus not constraining the solutions to in-plane transfers.

Firstly, the independent variable  $t$  was changed to true longitude  $L$ , such that the number of revolutions required by low-thrust transfer orbits is better represented. Then, by assuming that the orbit shows perturbative motion induced by the low-thrust propulsion only, the elements are approximated as shown in Equation 2.8.

$$\tilde{\alpha}_i = \tilde{\alpha}_{0i} + E_i(L, \boldsymbol{\lambda}) \quad (2.8)$$

In the above equation,  $\tilde{\alpha}_{0i}$  is the initial value of element  $i$ , and  $E_i(L, \boldsymbol{\lambda})$  is the shaping function describing the change in elements over time. The elements  $\tilde{\alpha}_i$  are called the pseudo-equinoctial elements, since these are an approximation of the actual modified equinoctial elements. They only satisfy the EoMs as given by Gauss' form of Lagrange's planetary equations when the thrust acceleration is zero.

Two shaping functions are considered, representing two types of low-thrust propulsion. The first one is shown in Equation 2.9. This shape, called the linear-trigonometric shape, can be associated with solar electric propulsion, where the thrust decreases quadratically with the distance to the Sun. The parameters  $\boldsymbol{\lambda} = [\lambda_1, \lambda_2, \lambda_3]^T$  determine the shape of the elements, with  $\lambda_1$  shaping the element  $p$ ,  $\lambda_2$  shaping the elements  $f$  and  $g$  and  $\lambda_3$  shaping the elements  $h$  and  $k$ . The parameters  $\tilde{\boldsymbol{\alpha}}_1$  are determined by the final state of the spacecraft.

$$\tilde{\boldsymbol{\alpha}} = \tilde{\boldsymbol{\alpha}}_0 + \tilde{\boldsymbol{\alpha}}_1(L - L_0) + \boldsymbol{\lambda} \sin(L - L_0 + \phi) \quad (2.9)$$

The second shaping function, representing nuclear electric propulsion systems that provide constant thrust, is shown in Equation 2.10 and is called the exponential trigonometric shape.

$$\tilde{\boldsymbol{\alpha}} = \tilde{\boldsymbol{\alpha}}_0 + \tilde{\boldsymbol{\alpha}}_1 e^{\lambda(L-L_0)} \sin[\omega(L - L_0) + \phi] \quad (2.10)$$

The frequency and phase parameters  $\omega$  and  $\phi$  in Equations 2.9 and 2.10 were found empirically. Moreover,  $\omega$  was found to be close to zero and was dropped altogether, reducing Equation 2.10 to an exponential shape.

The free constants present in the pseudo-equinoctial elements shaping functions are  $\tilde{\alpha}_0$ ,  $\tilde{\alpha}_1$  and  $\lambda$ . The first two sets,  $\tilde{\alpha}_0$  and  $\tilde{\alpha}_1$ , are used to satisfy the boundary conditions. The remaining three shaping parameters  $\lambda_1$ ,  $\lambda_2$  and  $\lambda_3$  are used to satisfy the thrust constraints. The required thrust acceleration is obtained when using the general EoM for perturbed motion:

$$\mathbf{u} = \ddot{\mathbf{r}} + \mu \frac{\mathbf{r}}{r^3} \quad (2.11)$$

The change in variables introduces an additional constraint for the transfer time, visualized in Equation 2.12. In this equation,  $T$  is the required time of flight.

$$T = \int_{L_0}^{L_f} \frac{dt}{dL} dL \quad (2.12)$$

When the propagated and shaped elements were compared, it was found that the shapes give a good approximation of the elements. Although the exponential shape did not capture the oscillatory motion, it did show the correct mean behaviour. The solutions for the elements  $f$  and  $g$  for the two different functions are shown in Figures 2.2 and 2.3. When applied to an optimization problem, the shape-based elements in combination with an evolutionary algorithm produce good results in terms of  $\Delta V$  and TOF, although being suboptimal.

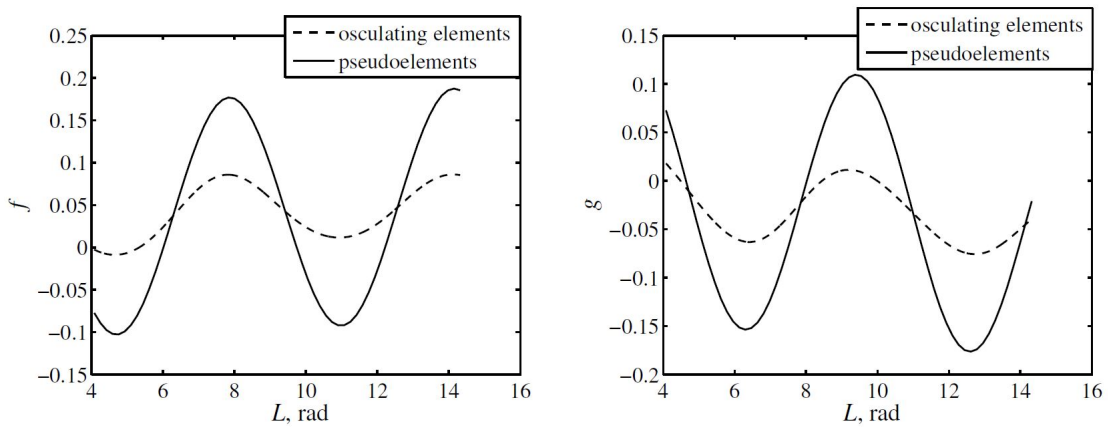


Figure 2.2: The comparison for the elements  $f$  and  $g$  using the linear-trigonometric shape [5].

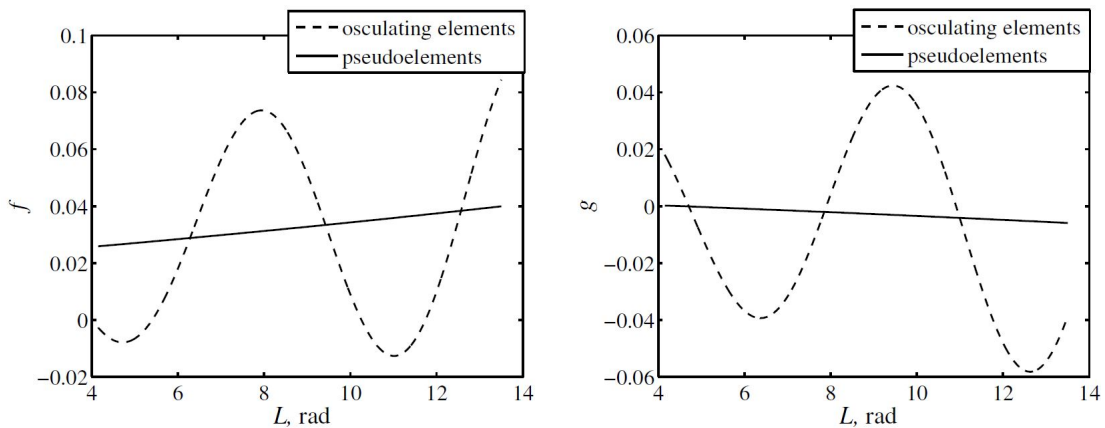


Figure 2.3: The comparison for the elements  $f$  and  $g$  using the exponential shape [5].

### Inverse Polynomials

This shape-based method has been developed by Wall and Conway [6] and is similar to the exponential sinusoids shape-based method. The shape of the trajectory is approximated by an inverse polynomial, as shown in Equation 2.13.

$$r = \frac{1}{a + b\theta + c\theta^2 + d\theta^3 + e\theta^4 + f\theta^5} \quad (2.13)$$

The same EoMs expressed in polar coordinates (Equations 2.2 and 2.3) are used to solve for the shape parameters  $a$ ,  $b$ ,  $c$ ,  $d$  and  $e$ . Six parameters have been chosen in order to satisfy six boundary conditions. The boundary conditions concern the initial and final positions, the initial and final flight path angles and initial and final angular velocities. Again, the thrust acceleration is assumed to point in the tangential direction. This simplifies the EoMs so that a solution can be found for the angular motion, as shown in Equation 2.14.

$$\dot{\theta}^2 = \frac{\mu}{r^4} \frac{1}{[(1/r) + 2c + 6d\theta + 12e\theta^2 + 20f\theta^3]} \quad (2.14)$$

The flight path angle can be determined with Equation 2.15.

$$\tan(\gamma) = -r \cdot (b + 2c\theta + 3d\theta^2 + 4e\theta^3 + 5f\theta^4) \quad (2.15)$$

Using Equations 2.13, 2.14 and 2.15 and the six boundary conditions, the six shape parameters can be determined by solving a set of linear equations. The thrust time is found by numerically integrating the result of Equation 2.14.

To solve the Lambert problem, an additional parameter is needed to meet the time constraint. This extra parameter is achieved by simply expanding the polynomial:

$$r = \frac{1}{a + b\theta + c\theta^2 + d\theta^3 + e\theta^4 + f\theta^5 + g\theta^6} \quad (2.16)$$

The six parameters satisfying the boundary conditions can once again be found directly by solving a system of linear equations. The last parameter though, satisfying the time constraint, has to be found iteratively using a root-finding algorithm.

The method has been extended to three dimensions in [7], by adding the third component of the cylindrical coordinates:

$$\ddot{z} = -\frac{\mu}{s^3}z + T_{az} \quad (2.17)$$

where,

$$s = \sqrt{r^2 + z^2} \quad (2.18)$$

The shaping function for this component is shown in Equation 2.19.

$$z(\theta) = a_z + b_z\theta + c_z\theta^{q-1} + d_z\theta^q \quad (2.19)$$

It is however assumed that  $z$  is relatively small compared to  $r$  in order to arrive at a solution. Consequently, the method has a limited range for inclination changes, being only valid for inclination changes of less than 15 degrees.

The above method is used in combination with a genetic algorithm in order to search for an optimum. For a transfer from Earth to Mars, the shape-based optimal solution gave a final mass that only differed 0.5% from the true optimal solution. The resulting transfer orbit can be seen in Figure 2.4. However, since the thrust acceleration is not constrained, the resulting thrust acceleration profile may require thrust accelerations that are out of range of the mission design variables.

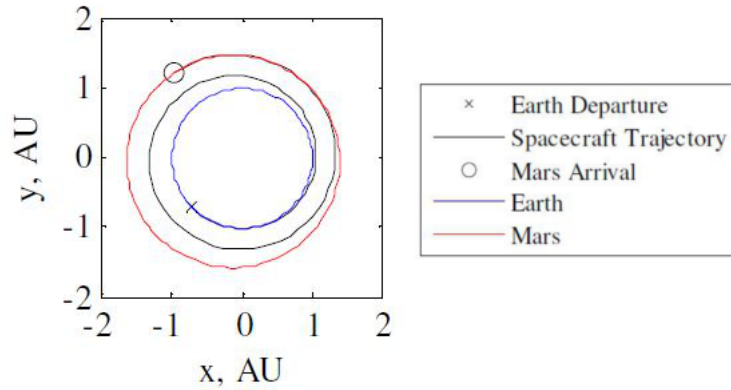


Figure 2.4: Example of the inverse polynomial shape: Earth-Mars rendezvous trajectory (modified from [7]).

### Spherical Shaping

The spherical shaping method has been developed by Novak and Vasile [8]. Their starting point is the parameterization of the spherical coordinates  $r$ ,  $\theta$  and  $\phi$  (radius, azimuth angle and elevation angle). However,  $\theta$  is chosen as the independent parameter. Thus, instead of a shaping function for  $\theta$ , a function of time expressed in  $\theta$  is formulated. The three shaping function are denoted as  $r = R(\theta)$ ,  $\phi = \Phi(\theta)$  and  $t = T(\theta)$ .

The EoMs that will need to be resolved with these shaping functions are shown in Equation 2.20.

$$\dot{\theta}^2 \frac{d^2 \mathbf{r}}{d\theta^2} + \ddot{\theta} \frac{d\mathbf{r}}{d\theta} = -\mu \frac{\mathbf{r}}{r^3} + \mathbf{u} \quad (2.20)$$

The shaping functions for  $r$  and  $\phi$  are shown in Equations 2.21 and 2.22, respectively. These are chosen in such a way that  $r$  is similar to the radius expressed in Kepler elements and that  $\phi$  is oscillating.

$$R = \frac{1}{a_0 + a_1\theta + a_2\theta^2 + (a_3 + a_4\theta) \cos(\theta) + (a_5 + a_6\theta) \sin(\theta)} \quad (2.21)$$

$$\Phi = (b_0 + b_1\theta) \cos(\theta) + (b_2 + b_3\theta) \sin(\theta) \quad (2.22)$$

The evolution of the time  $T(\theta)$  is more difficult to shape, however. Therefore, the following relationship for the derivative is set:

$$T' = \sqrt{\frac{DR^2}{\mu}} \quad (2.23)$$

where,

$$D = -r'' + 2 \frac{r'^2}{r} + r' \phi' \frac{\phi'' - \sin \phi \cos \phi}{\phi'^2 + \cos^2 \phi} + r(\phi'^2 + \cos^2 \phi) \quad (2.24)$$

Equation 2.24 has been derived by analyzing the relationship between the angular rate  $\dot{\theta}$  and the thrust acceleration in the normal direction. Thus, the time function is completely defined by the shaping functions  $R(\theta)$  and  $\Phi(\theta)$ . Also, by defining the time function as in Equation 2.23, it follows from the EoMs that the thrust acceleration in normal direction is zero.

The spherical shaping method has been compared with the pseudo-equinoctial shaping method and the results from the Direct Interplanetary Trajectory Analysis (DITAN) tool. In general, the spherical shaping method produces better results than the pseudo-equinoctial shaping method, although at the cost of larger computation time. Also, the results are relatively close to the optimized results from DITAN.

### Finite Fourier Series

Instead of fixing the shape of the trajectory with a specific shaping function, one can also approximate the trajectory by a sum of basis functions. Taheri and Abdelkhalik [9] introduced a shape-based method using the finite Fourier series (FFS) as basis functions. Approximating the trajectory by a sum of basis functions can be classified as a pseudo-spectral method. This has also been developed for ordinary polynomials in [16].

The functions of the distance and polar angle are expressed as a function of time with FFS as shown in Equations 2.25 and 2.26. Both the radius and the polar angle are set as a function of time to yield:

$$r(t) = \frac{a_0}{2} + \sum_{n=1}^{n_r} \left( a_n \cos\left(\frac{n\pi}{T}t\right) + b_n \sin\left(\frac{n\pi}{T}t\right) \right) \quad (2.25)$$

$$\theta(t) = \frac{c_0}{2} + \sum_{n=1}^{n_\theta} \left( c_n \cos\left(\frac{n\pi}{T}t\right) + d_n \sin\left(\frac{n\pi}{T}t\right) \right) \quad (2.26)$$

The number of Fourier terms is determined by  $n_r$  and  $n_\theta$  for  $r(t)$  and  $\theta(t)$ , respectively. The time of flight is denoted as  $T$ .

Equations 2.25 and 2.26 are used to solve the EoMs for perturbed satellite motion that are expressed in polar coordinates. Once again, tangential thrust is assumed to simplify the derivation. Then, the two EoMs can be rewritten to form a combined EoM, as shown in Equation 2.27.

$$r^2(\dot{\theta}\dot{r} - \dot{r}\dot{\theta}) + \dot{\theta}(\mu - 2r\dot{r}^2) - (r\dot{\theta})^3 = 0 \quad (2.27)$$

After Equations 2.25 and 2.26 are substituted in the above EoM, the FFS coefficients can be solved. In order to do this, the above equation is evaluated at a number of discretization points to form a nonlinear programming problem. In addition, the coefficients need to be initialized, which is done by assuming very simplistic shapes for the trajectory that satisfy the boundary conditions. The number of discretization points and Fourier terms are case-dependent, however a range has been determined that can be used for most transfer problems.

While the computation of the coefficients might seem computationally expensive, especially when compared with the earlier discussed methods, the computation times are similar to those of the time-constrained inverse polynomial shaping method. An advantage of the FFS shaping method is that the thrust acceleration can be constrained. This is shown in Equation 2.28. In this case, a feasible solution is not always present. This yields longer computation times.

$$C : \left( \frac{T_a}{T_{a,max}} \right)^2 \leq 1 \quad (2.28)$$

In addition, the FFS method has been further developed to include approximate on-off thrusting [10]. The thrust acceleration constraint is then defined as follows:

$$C : \frac{T_a}{T_{a,max}} + \sigma_i = 1 \quad (2.29)$$

In the above equation,  $\sigma_i$  is a slack variable that can be either 0, 1 or 2, depending on the magnitude and direction of the thrust. The resulting thrust profile for an Earth-Mars transfer is shown in Figure 2.5, where 1 DU = 149,598,000 km and  $2\pi$  TU = 1 year. However, using this thrust constraint, the computation time increases by an order of three to four.

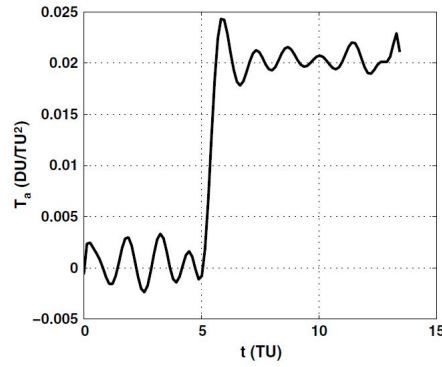


Figure 2.5: The approximate on-off thrust profile for an Earth-Mars transfer resulting from the FFS shaping method [10].

Finally, the FFS method has been proven to work even for restricted three-body problems [11]. Since the FFS method does not assume a particular shape, it is suitable to represent these kind of trajectories, which are significantly different from spirals.

### Hodographic Shaping

The hodographic-shaping method has been developed by Gondelach and Noomen [12]. For this method, the shape of the velocity as represented by a hodograph has been parameterized, instead of the shape of the position of the spacecraft. An example of the hodographic shape with the corresponding trajectory is shown in Figure 2.6, where  $V_t$  and  $V_r$  are the velocity in tangential and radial direction, respectively. Also, the EoMs are expressed in cylindrical coordinates directly, allowing the problem to be solved in three dimensions.

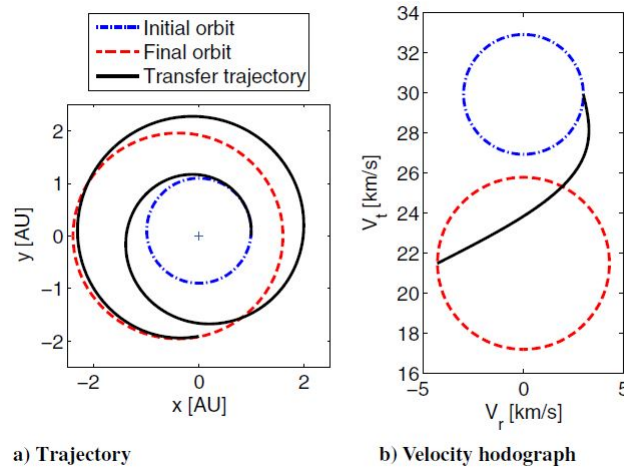


Figure 2.6: Example of the hodographic shape: a) the trajectory and b) velocity hodograph [12].

The velocities are expressed as a sum of simple base functions, such as sine or power function. The requirement is that the integration of these functions is straightforward. The minimum number of base functions  $n$  depends on the number of boundary conditions, since each base functions introduces a free parameter  $c_i$ .

The independent variable of the velocity functions can be either time or polar angle. The shape function expressed in time is shown in Equation 2.30.

$$V(t) = \sum_{i=1}^n c_i v_i(t) \quad (2.30)$$

Nine boundary conditions have been established in order to solve for the transfer problem, namely the initial velocity, the final velocity and the travelled distance (in three dimensions). Since the shape

functions are linear, the coefficients can be determined without the need for iteration, resulting in reduced computation time.

The velocity can also be shaped as a function of polar angle. However, since the transverse direction is defined as the polar angle, the time is defined as a function of polar angle. The time of flight can then be easily determined by integrating the resulting function to the final polar angle. Again, the boundary conditions include the initial and final conditions, and the difference in position. For the time shape function, the time of flight is taken instead of the travelled distance.

If more than three coefficients per velocity direction are taken, extra degrees of freedom are introduced. These can be used to optimize the  $\Delta V$ , or to satisfy thrust acceleration constraints.

The final results in velocities have been compared to numerically propagated trajectories. For the numerical propagation, the accelerations resulting from the hodographic method are used as input. The differences in results were small, with the position differing less than 1000 km and the velocity less than 0.1 m/s. Furthermore, the hodograph shape functions have been used for optimization problems, which are compared to results from the direct trajectory analysis tool DITAN, but also to the results from the pseudo-equinoctial and spherical shaping methods. Good results for  $\Delta V$  and the maximum required thrust acceleration were found, however trajectories with many revolutions performed worse.

## 2.2. Gravity Losses

Eliminating the radial thrust component as a possible solution for the thrust vector will simultaneously impose zero gravity losses during transfer. Quarta and Mengali [17] have studied this type of transfer for the planar case. Assuming a constant thrust, the EoMs expressed in polar coordinates can be written as in Equations 2.31.

$$\dot{r} = u \quad (2.31a)$$

$$\dot{\theta} = \frac{v}{r} \quad (2.31b)$$

$$\dot{u} = -\frac{\mu}{r^2} + \frac{v^2}{r} \quad (2.31c)$$

$$\dot{v} = -\frac{uv}{r} + \tau a_p \quad (2.31d)$$

These EoMs seem different from the EoMs given in Section 2.1 for polar coordinates, but are actually an alternative form. By substituting Equations 2.31a and 2.31b into Equations 2.31c and 2.31d the exact same formulation will be found.

For the derivation, no coast arcs are considered. However, the direction of the acceleration can be either along the velocity or in the opposite direction. Thus, in Equation 2.31d,  $\tau$  is either 1 or -1, but never zero. It is furthermore assumed that the satellite starts in a circular parking orbit.

The system of differential equations is simplified by a change of variable, using the semi-latus rectum instead of time as independent variable. Also, the dimensionless variables that are shown in Equations 2.32 are substituted.

$$\tilde{r} = \frac{r}{r_0} \quad (2.32a)$$

$$y = \tilde{r}^2 \quad (2.32b)$$

$$\tilde{a}_p = \frac{a_p}{(m/r_0^2)} \quad (2.32c)$$

$$\tilde{p} = \frac{p}{r_0} \quad (2.32d)$$

Then, the relationship shown in Equation 2.33 can be found, where the prime indicates the derivative with respect to the dimensionless semi-latus rectum.

$$(2\tilde{p}y'' + y')(\tau\tilde{a}_py)^2 = \tilde{p} - \sqrt{y} \quad (2.33)$$

The assumption can now be made that the term  $\tilde{a}_py$  is much smaller than 1, since the thrust acceleration is small. This is valid as long as  $y$  does not increase too much. This means that the position

of the spacecraft in orbit may not diverge too much from the initial distance  $r_0$ . This assumption results in Equation 2.34.

$$\sqrt{y} \simeq \tilde{p} \quad (2.34)$$

The radius of the trajectory can then be approximated by the Equation 2.35, where  $\tilde{t}$  is the dimensionless time defined as  $t/\sqrt{r_0^3/\mu}$ .

$$\tilde{r} \simeq \frac{1}{(1 - \tau \tilde{a}_p \tilde{t})^2} \quad (2.35)$$

This radial and circumferential velocity can then be approximated in the following way:

$$\tilde{u} \simeq 2\tau \tilde{a}_p \sqrt{\tilde{p}^3} \quad (2.36a)$$

$$\tilde{v} \simeq \frac{1}{\sqrt{\tilde{p}}} \quad (2.36b)$$

The above analysis only holds if  $\tilde{a}$  and  $y$  are indeed relatively small. To quantify the accuracy of the solution found, the following condition can be defined:

$$\left| \frac{\sqrt{y_m}}{\tilde{p}} - 1 \right| = \epsilon \quad (2.37)$$

In the above equation,  $\sqrt{y_m} = \tilde{r}_m$  is the maximum value the dimensionless radial distance can take for the solution to still be within the accuracy of a given  $\epsilon$ . The change in  $\tilde{r}$  over time can be obtained by numerically integrating Equation 2.33. The results for various values of  $\epsilon$  and  $a_p$  are shown in Figure 2.7. Lower values of acceleration allow for higher maximum radii for the same level of accuracy. Since the thrust acceleration is constant, the required  $\Delta V$  is directly dependent on the time of flight. If the radius is approximated by the analytical solution within a certain range that is defined by  $\epsilon$ , this will also influence the required time of flight, since these are related by Equation 2.35. Thus, both the required  $\Delta V$  and TOF are influenced directly by the accuracy defined by  $\epsilon$ .

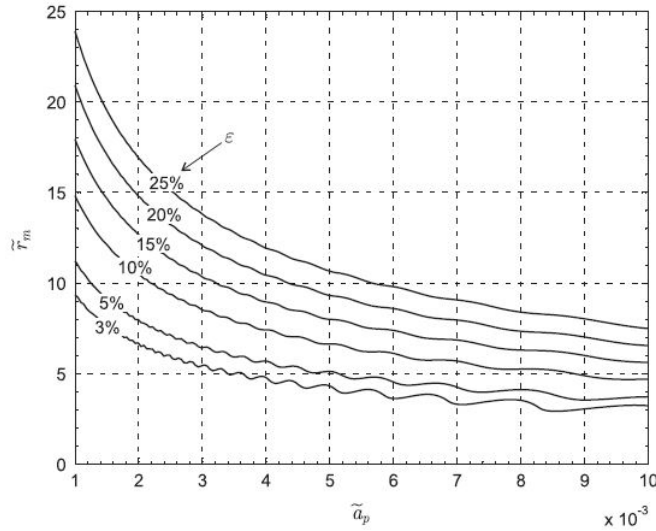


Figure 2.7: The maximum dimensionless radius as a function of the dimensionless propulsive acceleration, for different values of  $\epsilon$  [17].

### 2.3. Bang-Bang Control

Bang-bang control implies that the total thrust acceleration is either zero or maximum during flight. This is also referred to as on-off thrust. This thrust profile often appears as the optimum profile when fuel consumption is minimized [18]. In Figure 2.8, an example of a transfer orbit with coasting and

thrusting arcs is shown. Here, a trajectory from Earth to Mars is optimized [18]. In order to do this, Lawden's primer vector theory has been used, based on the calculus of variations.

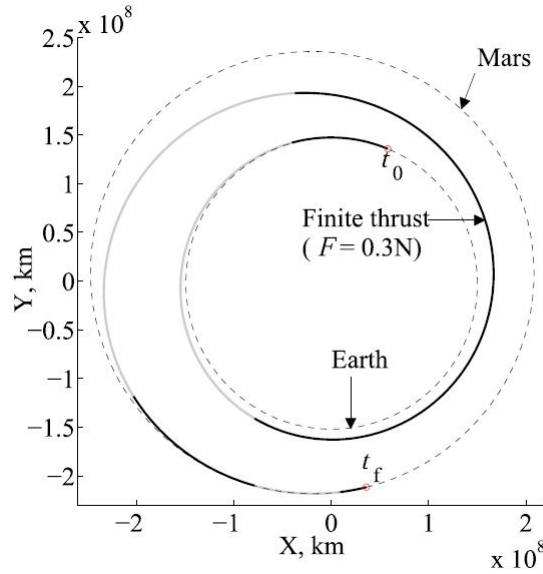


Figure 2.8: Earth-Mars transfer orbit with thrust (black) and coast (grey) arcs [18].

The objective of the transfer problem was to minimize the propellant consumption or equivalently maximize the final mass of the spacecraft. This can be formulated as shown in Equation 2.38, which is the design performance index. In this equation,  $m(t_f)$  is the final mass of the satellite. Note that the problem is defined to minimize the performance index, thus a minus sign is added to the final mass.

$$J = \min[-m(t_f)] \quad (2.38)$$

Then, the EoMs are defined as shown in Equations 2.39 to 2.41. In these equations,  $\alpha$  is the unit vector denoting the direction of the thrust,  $I_{sp}$  is the specific impulse,  $g_0$  is the standard gravitational acceleration at sea-level and  $\dot{m}$  is the mass flow.

$$\dot{\mathbf{r}} = \mathbf{v} \quad (2.39)$$

$$\dot{\mathbf{v}} = -\frac{\mu}{r^3}\mathbf{r} + \frac{F}{m}\alpha \quad (2.40)$$

$$\dot{m} = -\frac{F}{g_0 I_{sp}} \quad (2.41)$$

In order to optimize Equation 2.38, three co-state variables are introduced, namely  $\lambda_r$ ,  $\lambda_v$  and  $\lambda_m$ . These are used to construct the Hamiltonian function, as shown in Equation 2.42.

$$H = \lambda_r^T \dot{\mathbf{r}} + \lambda_v^T \dot{\mathbf{v}} + \lambda_m \dot{m} \quad (2.42)$$

The optimal thrusting direction then follows from Equation 2.43

$$\alpha^* = -\frac{\lambda_v}{\|\lambda_v\|} \quad (2.43)$$

In addition, the switching moments are determined by using the switching function  $S$  as shown in Equation 2.44. These moments are chosen according to the conditions shown in Equation 2.45,  $F$  being a constant thrust amplitude [18].

$$S = \frac{\partial H}{\partial F} = \frac{\lambda_v^T \alpha^*}{m} - \frac{\lambda_m}{g_0 I_{sp}} = -\frac{\|\lambda_v\|}{m} - \frac{\lambda_m}{g_0 I_{sp}} \quad (2.44)$$

$$\begin{cases} F^* = 0 & \text{if } S > 0 \text{ (coasting arc)} \\ F^* = F & \text{if } S < 0 \text{ (thrusting arc)} \end{cases} \quad (2.45)$$

The optimal bang-bang structure in Figure 2.8 has been achieved with a continuation technique on the thrust amplitude. In order to do so, first a solution for the optimal transfer with minimum thrust is calculated. Starting from Lambert's problem, the co-state variables for a two-impulse transfer are obtained. Then, the minimum-thrust transfer is determined by gradually decreasing the thrust amplitude, until the rocket engine has to be on continuously for a feasible trajectory. This final thrust amplitude is then the minimum required thrust amplitude. Note that the corresponding switching function does not necessarily comply with Equation 2.45, that is  $S \leq 0$  (because no coast arcs are present). Therefore, a positive constant is used to scale the co-state variables, such that switching function becomes less or equal to zero for the entire transfer.

The minimum thrust amplitude is then used as the initial amplitude for the continuation technique. The gradual increase in thrust amplitude is determined with Equation 2.46, where  $c$  is an adaptive constant.

$$F_{n+1} = (1 + c)F_n, \quad n = 0, 1, 2, \dots \quad (2.46)$$

For each thrust amplitude, the sequence of thrust arcs and coast arcs and the switching moments are derived from the corresponding switching function. This continuation process is stopped when the length of the thrust arcs is small enough to be negligible, so that they can be approximated by an impulse.

For the optimization of the transfer from Earth to Mars, the behaviour of the switching functions is shown in Figure 2.9. Three cases are presented: the minimum thrust amplitude, where  $S \leq 0$ , the impulsive thrust, where  $S \geq 0$  (the impulses are applied at the points where  $S = 0$ ), and a thrust amplitude in between these two extremes, where a bang-bang thrust profile is present. For this last case, where the thrust amplitude is equal to 0.3 N, five thrust arcs and three coast arcs can be derived from Figure 2.9. Also, the switching moments can be determined using this figure. The total time of flight is a given parameter for the optimization process (and in this case set to 793 days). Note that this case corresponds to the trajectory shown in Figure 2.8.

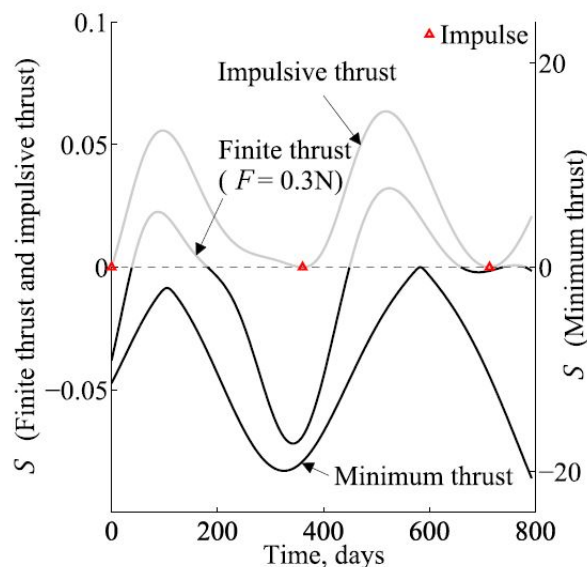


Figure 2.9: The behaviour of switching functions for the minimum, finite and impulsive thrust cases.[18].

The final mass for the Earth-Mars transfer with a thrust amplitude of 0.3 N is equal to 1649.22 kg. The required  $\Delta V$  can then be computed using Tsiolkovsky's equation as shown in Equation 2.47 [19].

$$\Delta V = V_j \ln \left( \frac{M_0}{M_e} \right) \quad (2.47)$$

In this equation,  $M_0$  and  $M_e$  are the initial mass and final mass, respectively, and  $V_j$  is the exhaust velocity, defined by Equation 2.48 [20].

$$V_j = I_{sp} g_0 \quad (2.48)$$

For the Earth-Mars transfer problem described above,  $I_{sp} = 3000$  s and  $M_0 = 2000$  kg. Then, it follows that  $\Delta V = 5.68$  km/s.



# 3

## Astrodynamics

As discussed in the previous chapter, having an analytical expression for the motion of the spacecraft would increase the optimization efficiency. Apart from developing an analytical solution, two other concepts will be used to potentially increase the efficiency of the optimization process. Often it is assumed that the thrust of a spacecraft is directed tangentially, aligned with the velocity vector. A great number of shape-based methods discussed in the previous chapter make use of such an assumption. However, having tangential thrust means that a (small) component of the thrust force (the magnitude depends on the flight path angle) will be directed in the radial direction, towards the center of gravity of the main attracting body. This introduces gravity losses, which indicates that the propellant is being used inefficiently. Therefore, a possible way to arrive at a first-order solution that is closer to the true optimal solution is to assume from the start that no gravity losses are allowed, i.e. that no thrust component will be directed radially.

Furthermore, optimal solutions often include bang-bang control or a similar thrust profile, that is, the rocket engine is either on or off, and the thrust level is fixed. This will be discussed in more detail in Chapter 6. In this chapter, the most important features regarding the astrodynamics of the problem will be discussed and the basis will be set for deriving an analytical solution. In Section 3.1, the perturbing accelerations that act on the spacecraft are analyzed and a selection is made of which accelerations are taken into account. In Section 3.2, a suitable coordinate system is chosen and the EoMs are set up.

### 3.1. Perturbing Accelerations

The analytical solution can be found by integrating the EoMs. These can be represented in a number of ways. But before setting up the EoMs, it is important to specify which forces acting on the spacecraft will be taken into consideration. Besides the central gravity of the main attracting body and the thrust force provided by the engine, there are many perturbing forces acting on the spacecraft, such as solar radiation pressure, atmospheric drag and third-body perturbations. However, one has to keep in mind that an analytical solution is sought, and therefore the EoMs would eventually be too complex to solve if too many forces are taken into account.

The magnitude of the thrust acceleration can be obtained by an analysis of existing low-thrust engines. Three main categories can be distinguished for low-thrust propulsion systems, depending on their working principle: electrothermal propulsion systems, including resistojets and arcjets, electrostatic propulsion systems, including ion thrusters, and electromagnetic propulsion system, including magnetoplasmadynamic (MPD) thrusters, pulsed plasma (PPT) thrusters and Hall-effect thrusters [1] [21]. Table 3.1 gives a summary of the most important characteristics of these thrusters.

Table 3.1: Characteristics of various electric propulsion systems (modified from [1]).

Type	Thrust (mN)	Specific Impulse (sec)	Thrust Duration	Kinetic Power per Unit Thrust (W/mN)	Flown in Space Mission
Resistojet (thermal)	200-300	200-350	Months	0.5-6	TET-1 (2012) [22]
Arcjet (thermal)	200-1000	400-800	Months	2-3	OSCAR-40 (2000) [23]
Ion thruster	0.01-500	1500-8000	Years	10-70	SES-15 (2017) [24]
Solid PPT	0.05-10	600-2000	Years	10-50	Pegasus (2017) [25]
MPD	0.001-2000	2000-5000	Weeks	100	SFU (1995) [26]
Hall thruster	0.01-2000	1500-2000	Months	100	Asiasat-9 (2017) [27]

The accelerations that the thruster provides can be deducted from Table 3.1. However, MPD thrusters will not be taken into account, since these have not been flown frequently and are only experimental. If a spacecraft mass of 1000 kg is assumed, it follows from Table 3.1 that the acceleration can range from  $10^{-8}$  m/s<sup>2</sup> to  $10^{-3}$  m/s<sup>2</sup>.

The magnitude of the perturbing accelerations near Earth is shown in Figure 3.1. This figure also indicates the range of the low-thrust accelerations.

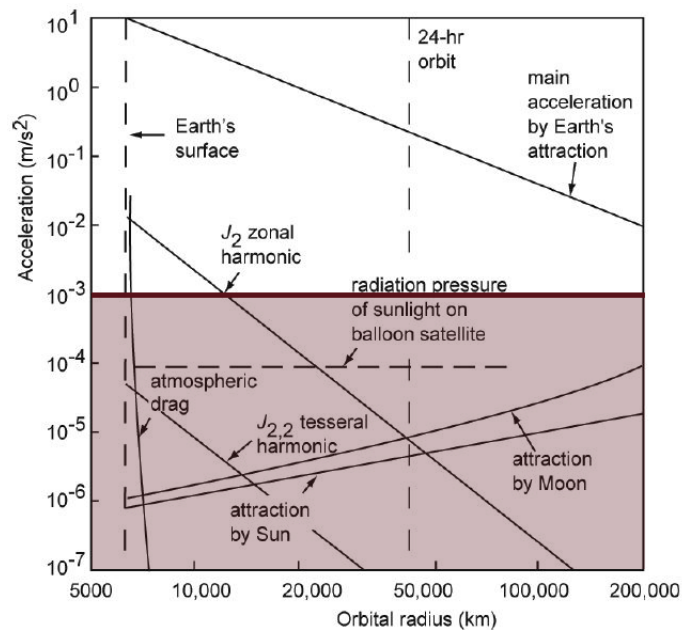


Figure 3.1: Overview of the main perturbing accelerations for a geocentric orbit with respect to low-thrust propulsion (highlighted region) (modified from [19]).

Atmospheric drag is only significant for orbits relatively close to the Earth, and decreases rapidly with increasing altitude. Also the  $J_{2,2}$  perturbation decreases as the orbital radius increases. The  $J_2$  perturbation remains significant however, for a larger range of altitudes. Also, the third-body perturbations from the Moon and Sun increase as the spacecraft moves away from the Earth. Thus, the influence of the perturbing accelerations on the motion of the spacecraft depends heavily on the orbital radius. However, the thrust magnitude can be chosen in such a way, that it becomes relatively larger than the remaining perturbations. For example, the SMART-1 mission, which achieved a low-thrust transfer from the Earth to the Moon, had a thrust acceleration in the order of  $10^{-4}$  m/s<sup>2</sup>. Then, only the  $J_2$  perturbation will bring a large factor of inaccuracy when ignored in modelling a geocentric orbit.

For heliocentric orbits, the main perturbations are shown in Figure 3.2. Again, the highlighted area indicates the range of the thrust acceleration. From this figure, it is clear that the third-body perturbations only become significant if the spacecraft approaches a particular celestial body. Also, the solar radiation pressure decreases as the distance to the Sun increases. For outward transfer orbits

from Earth, the thrust acceleration forms the most important source of perturbation, assuming the acceleration is not too small (e.g. in the order of  $10^{-4} \text{ m/s}^2$ ).

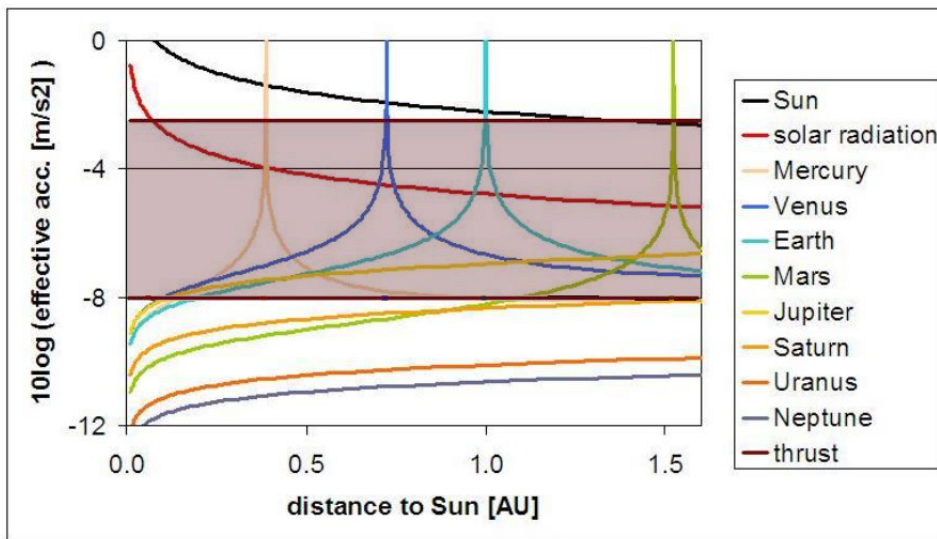


Figure 3.2: Overview of the main perturbing accelerations for a heliocentric orbit with respect to low-thrust propulsion (dark red region) (modified from [28]).

In conclusion, only the thrust force and the central gravity force of the main attracting body will be taken into account. For heliocentric orbits, this assumption is fair as long as the spacecraft does not enter the sphere of influence of a planet during the transfer and keeps a distance of at least 0.5 AU with respect to the Sun. For geocentric orbits, the inaccuracy might be significant for very low orbits, but nevertheless should give a reasonable first-order estimate.

### 3.2. Equations of Motion

With the acting forces now established, the EoMs of the spacecraft can be set up. To increase the applicability of the derived solution, a three-dimensional coordinate system is desired. The most basic coordinate system is the Cartesian coordinate system, which is defined by three orthogonal axes  $x$ ,  $y$  and  $z$ , see Figure 3.3.

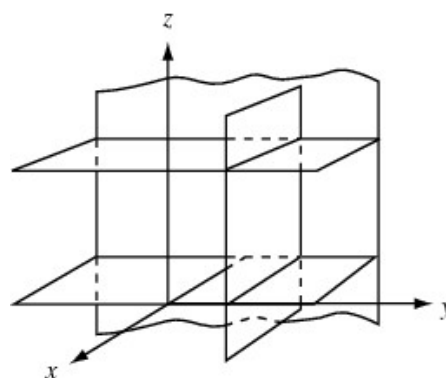


Figure 3.3: Cartesian Coordinate System [29].

The EoMs in Cartesian coordinates are showed in Equations 3.1, where  $f_x$ ,  $f_y$  and  $f_z$  are the thrust accelerations in the  $x$ -,  $y$ - and  $z$ -direction, respectively.

$$\ddot{x} + \mu \frac{x}{r^2} = f_x \tag{3.1a}$$

$$\ddot{y} + \mu \frac{y}{r^2} = f_y \quad (3.1b)$$

$$\ddot{z} + \mu \frac{z}{r^2} = f_z \quad (3.1c)$$

The above EoMs have the disadvantage that the radial thrust acceleration is not explicitly stated, thus setting this thrust component to zero is not straightforward. Another possible representation of the EoMs can be given in spherical coordinates. The definition of the spherical coordinates is shown in Figure 3.4. The description of the axes is given below.

- $r$  is the radial distance from the origin
- $\theta$  is the azimuth angle, between the x-axis and the line from the origin to the projection of the point on the x-y plane
- $\phi$  is the polar angle, between the positive z-axis and the line from the origin to the point

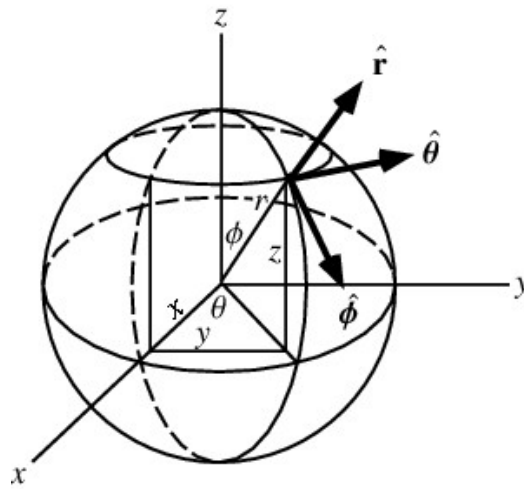


Figure 3.4: Spherical Coordinate System [30].

The EoMs expressed in spherical coordinates are given in Equations 3.2 [31], where  $f_r$ ,  $f_\phi$  and  $f_\theta$  represent the thrust accelerations in the  $\hat{r}$ -,  $\hat{\phi}$ - and  $\hat{\theta}$ -direction as shown in Figure 3.4.

$$\ddot{r} - r\dot{\phi}^2 - r\dot{\theta}^2 \sin^2(\phi) + \frac{\mu}{r^2} = f_r \quad (3.2a)$$

$$r\ddot{\phi} + 2\dot{r}\dot{\phi} - r\dot{\theta}^2 \sin(\phi) \cos(\phi) = f_\phi \quad (3.2b)$$

$$r\ddot{\theta} \sin(\phi) + 2\dot{r}\dot{\theta} \sin(\phi) + 2r\dot{\phi}\dot{\theta} \cos(\phi) = f_\theta \quad (3.2c)$$

The spherical coordinates are convenient, since the acceleration in the radial direction is explicitly stated in the first equation of motion. This makes it easy to satisfy the first constraint (no gravity losses allowed), by setting  $f_r$  equal to zero. However, these equations make a complex set to solve, since they are highly non-linear and coupled second-order differential equations. Finding expressions for  $r$ ,  $\theta$  and  $\phi$  that comply with these equations is quite challenging, if possible at all.

A satellite's orbit can also be described by using the Kepler orbital elements. For an unperturbed orbit, these elements remain constant over time (apart from the last element). The elements are defined as described below.

- $a$  is the semi-major axis of the orbit
- $e$  is the eccentricity of the orbit

- $i$  is the inclination, which is the angle between the orbital plane and the reference frame
- $\omega$  is the argument of pericenter, which is measured from the ascending node to the pericenter of the orbit
- $\Omega$  is the longitude of the ascending node, which is measured from a reference direction in the reference frame to the ascending node (the point where the spacecraft crosses the reference frame traveling from South to North) of the orbit
- $\theta$  is the true anomaly, the angle between the pericenter and the spacecraft in the orbital plane

The definitions of  $a$  and  $e$  are shown in Figure 3.5, while the definitions of  $i$ ,  $\omega$ ,  $\Omega$  and  $\theta$  are shown in Figure 3.6.

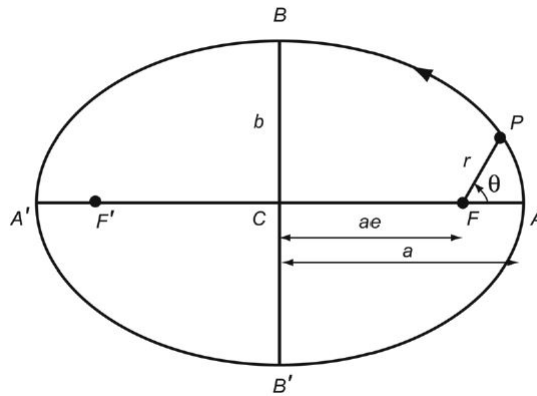


Figure 3.5: Definition of semi-major axis and eccentricity [19].

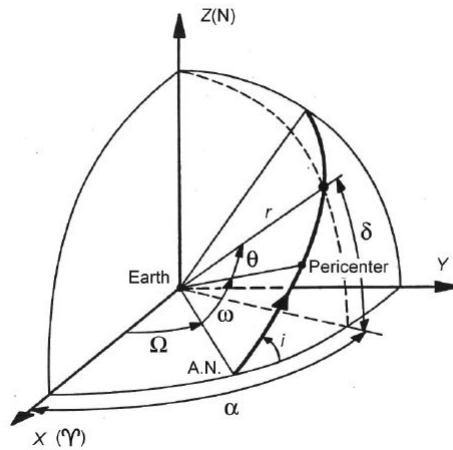


Figure 3.6: Definition of inclination, argument of periapsis, longitude of the ascending node and true anomaly [19].

The EoMs expressed in Kepler elements are given by Gauss' form of the Lagrange planetary equations, as shown in Equations 3.3 [19].

$$\frac{da}{dt} = 2 \frac{a^2}{\sqrt{\mu p}} \left[ f_S e \sin(\theta) + f_N \frac{p}{r} \right] \quad (3.3a)$$

$$\frac{de}{dt} = \sqrt{\frac{p}{\mu}} \left[ f_S \sin(\theta) + f_N (\cos(E) + \cos(\theta)) \right] \quad (3.3b)$$

$$\frac{di}{dt} = f_W \frac{r}{\sqrt{\mu p}} \cos(u) \quad (3.3c)$$

$$\frac{d\omega}{dt} = -\sqrt{\frac{p}{\mu}} \left[ f_W \frac{r}{p} \cot(i) \sin(u) + \frac{1}{e} \left[ f_S \cos(\theta) - f_N \left( 1 + \frac{r}{p} \right) \sin(\theta) \right] \right] \quad (3.3d)$$

$$\frac{d\Omega}{dt} = f_W \frac{r}{\sqrt{\mu p} \sin(i)} \sin(u) \quad (3.3e)$$

$$\frac{dM}{dt} = n - f_S \left[ \frac{2r}{\sqrt{\mu a}} - \frac{1-e^2}{e} \sqrt{\frac{a}{\mu}} \cos(\theta) \right] - f_N \frac{1-e^2}{e} \sqrt{\frac{a}{\mu}} \left( 1 + \frac{r}{p} \right) \sin(\theta) \quad (3.3f)$$

The directions of the thrust accelerations  $f_S$ ,  $f_N$  and  $f_W$  are shown in Figure 3.7.

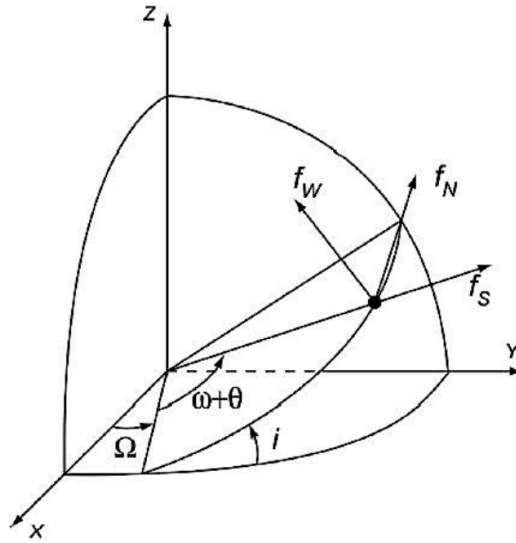


Figure 3.7: Directions of the accelerations in the Gauss' form of the planetary equations [19].

This set of equations has an advantage over the spherical coordinates by being first-order differential equations, rather than second-order. The radial thrust acceleration can again be set to zero directly. However, these equations have the disadvantage of containing singularities for orbits with zero eccentricity and zero inclination. It would therefore be advantageous to find a set of first-order differential equations without these singularities. This problem has been studied by Walker et al., who developed the modified equinoctial elements as an alternative for the Kepler elements. The definition of the modified equinoctial elements is shown in Equation 3.4 [32]. Note that the first parameter  $p$  is the semi-latus rectum, and the last parameter  $L$  is the true longitude.

$$p = a(1 - e^2) \quad (3.4a)$$

$$f = e \cos(\omega + \Omega) \quad (3.4b)$$

$$g = e \sin(\omega + \Omega) \quad (3.4c)$$

$$h = \tan(i/2) \cos(\Omega) \quad (3.4d)$$

$$k = \tan(i/2) \sin(\Omega) \quad (3.4e)$$

$$L = \Omega + \omega + \theta \quad (3.4f)$$

For converting the modified equinoctial elements to Kepler elements, Equations 3.5 can be used [33]. Note that the argument of latitude  $u$  is mentioned rather than the true anomaly  $\theta$ , since the true anomaly is not defined for circular orbits. The four-quadrant inverse tangent is used for the conversion of the argument of periaapsis, the longitude of the ascending node and the argument of latitude.

$$a = \frac{p}{1 - f^2 - g^2} \quad (3.5a)$$

$$e = \sqrt{f^2 + g^2} \quad (3.5b)$$

$$i = 2 \operatorname{atan}(\sqrt{h^2 + k^2}) \quad (3.5c)$$

$$\omega = \operatorname{atan2}(g, f) - \operatorname{atan2}(k, h) \quad (3.5d)$$

$$\Omega = \operatorname{atan2}(k, h) \quad (3.5e)$$

$$u = L - \operatorname{atan2}(k, h) \quad (3.5f)$$

The equations of motion expressed in modified equinoctial elements, derived from Lagrange's planetary equations, are shown in Equations 3.6 [32].

$$\frac{dp}{dt} = 2 \frac{p}{w} \sqrt{\frac{p}{\mu}} f_N \quad (3.6a)$$

$$\frac{df}{dt} = \sqrt{\frac{p}{\mu}} \left[ \sin(L) f_S + \frac{1}{w} ((w+1) \cos(L) + f) f_N - \frac{g}{w} (h \sin(L) - k \cos(L)) f_W \right] \quad (3.6b)$$

$$\frac{dg}{dt} = \sqrt{\frac{p}{\mu}} \left[ -\cos(L) f_S + \frac{1}{w} ((w+1) \sin(L) + g) f_N - \frac{f}{w} (h \sin(L) - k \cos(L)) f_W \right] \quad (3.6c)$$

$$\frac{dh}{dt} = \sqrt{\frac{p}{\mu}} \frac{(s^2 \cos(L))}{2w} f_W \quad (3.6d)$$

$$\frac{dk}{dt} = \sqrt{\frac{p}{\mu}} \frac{(s^2 \sin(L))}{2w} f_W \quad (3.6e)$$

$$\frac{dL}{dt} = \sqrt{\frac{p}{\mu}} \frac{1}{w} (h \sin(L) - k \cos(L)) f_W + \sqrt{\mu p} \left( \frac{w}{p} \right)^2 \quad (3.6f)$$

with,

$$w = 1 + f \cos(L) + g \sin(L) \quad (3.7a)$$

$$s^2 = 1 + h^2 + k^2 \quad (3.7b)$$

These form a convenient set of equations as basis for an analytical solution, but need to be further simplified before starting the derivation. The first simplification occurs naturally by implementation of the zero-radial-thrust constraint, i.e. setting  $f_S$  to zero. However, the equations remain strongly coupled. In an attempt to decouple them, one could assume the eccentricity to be approximately zero. Since only low-thrust transfers are taken into consideration, one can presume that the change in eccentricity at any moment of time during the transfer is close to zero. This would also imply that only circular-to-circular orbit transfers are suitable for the to-be-developed method.

Setting the eccentricity approximately to zero has the following implications:

$$f \approx 0 \quad (3.8a)$$

$$g \approx 0 \quad (3.8b)$$

$$w \approx 1 \quad (3.8c)$$

Another point of simplification can be found when considering the course of the true longitude  $L$ . When looking closely at its derivative with respect to time (Equation 3.6f), an oscillatory and non-oscillatory term can be distinguished. Since low-thrust transfer orbits usually entail a long transfer time,

one can expect that the oscillatory behaviour cancels out over time, and is left with the non-oscillatory term, representing the mean motion. Thus, one can consider only the mean motion.

Therefore, the simplified EoMs become:

$$\frac{dp}{dt} = 2p \sqrt{\frac{p}{\mu}} f_N \quad (3.9a)$$

$$\frac{df}{dt} = \sqrt{\frac{p}{\mu}} 2 \cos(L) f_N \quad (3.9b)$$

$$\frac{dg}{dt} = \sqrt{\frac{p}{\mu}} 2 \sin(L) f_N \quad (3.9c)$$

$$\frac{dh}{dt} = \sqrt{\frac{p}{\mu}} \frac{(1 + h^2 + k^2) \cos(L)}{2} f_W \quad (3.9d)$$

$$\frac{dk}{dt} = \sqrt{\frac{p}{\mu}} \frac{(1 + h^2 + k^2) \sin(L)}{2} f_W \quad (3.9e)$$

$$\frac{dL}{dt} = \sqrt{\mu p} \left(\frac{1}{p}\right)^2 \quad (3.9f)$$

The above equations apply for moments when the engine is on, i.e. during a thrust arc. However, bang-bang control implies the rocket engine can be turned off, too. These coast arcs will be introduced in Chapter 6. Furthermore, the total thrust acceleration  $f_{tot}$  is constant during a thrust arc. Therefore, the thrust acceleration in transverse direction  $f_N$  and perpendicular to the orbital plane  $f_W$  are decomposed from the total thrust by the steering angle  $\alpha$  (Equations 3.10 and 3.11). This angle is defined in Figure 3.8. Finally, a last simplification is made by setting the steering angle  $\alpha$  also as a constant during each individual thrust arc.

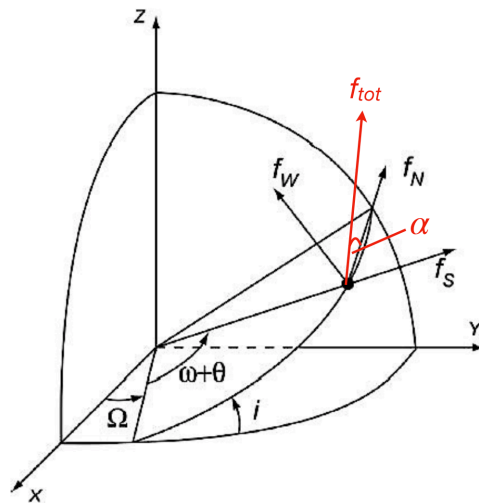


Figure 3.8: Definition of the steering angle (modified from [19]).

$$f_N = f_{tot} \cos(\alpha) \quad (3.10)$$

$$f_W = f_{tot} \sin(\alpha) \quad (3.11)$$

# 4

## Analytical Solution using True Longitude

In this chapter, an analytical solution for low-thrust transfer orbits is investigated. In the previous chapter, the EoMs expressed in modified equinoctial elements have been chosen as the basis for the analytical solution. Moreover, assumptions and simplifications have been applied to facilitate the analytical solution so that no use of a numerical integrator is required. At first glance, Equations 3.9 seem to depend on the true longitude  $L$ , rather than on time  $t$ . Therefore, as a first attempt the functions are integrated with respect to  $L$  rather than  $t$ . In Section 4.1 this derivation is presented. Section 4.2 describes the characteristics of some special functions that appear in the analytical solutions. It is important to understand these functions as their behaviour influences the applicability of the resulting solution. The accuracy of the analytical solutions are assessed using a numerical integrator. The tuning of the numerical integrator is discussed in Section 4.3. Finally, the results are shown and discussed in Section 4.4.

### 4.1. General Solution

In order to arrive at an analytical solution expressed as a function of true longitude, the differential equations as shown in Equations 3.9 have to be expressed as a derivative with respect to  $L$  instead of  $t$ . This can be achieved by dividing each equation by  $dL/dt$ , such that the dependency on  $t$  disappears. In the previous chapter, it has been decided that only mean motion will be taken into account. This significantly facilitates the change of variables. The resulting EoMs are all expressed as a function of  $L$ , as shown in Equations 4.1.

$$\frac{dp}{dL} = 2\frac{p^3}{\mu}f_N \quad (4.1a)$$

$$\frac{df}{dL} = 2\frac{p^2}{\mu}\cos(L)f_N \quad (4.1b)$$

$$\frac{dg}{dL} = 2\frac{p^2}{\mu}\sin(L)f_N \quad (4.1c)$$

$$\frac{dh}{dL} = \frac{p^2}{2\mu}(1 + h^2 + k^2)\cos(L)f_W \quad (4.1d)$$

$$\frac{dk}{dL} = \frac{p^2}{2\mu}(1 + h^2 + k^2)\sin(L)f_W \quad (4.1e)$$

Note that both  $f_N$  and  $f_W$  are assumed to be constant during each individual thrust arc. Thus, Equation 4.1a can be solved by separation of variables, as shown in Equation 4.2.

$$\frac{dp}{p^3} = \frac{2f_N}{\mu}dL \quad (4.2)$$

Integration leads to:

$$-\frac{1}{2p^2} = \frac{2f_N}{\mu}L + C_p \quad (4.3)$$

which can be rearranged as:

$$p^2 = \frac{\mu}{-4f_N L - 2\mu C_p} \quad (4.4)$$

or,

$$p(L) = \sqrt{\frac{-\mu}{4f_N L + 2\mu C_p}} \quad (4.5)$$

The integration constant  $C_p$  is obtained with the initial condition  $p(L_0) = p_0$ :

$$C_p = -\frac{1}{2p_0^2} - \frac{2}{\mu}f_N L_0 \quad (4.6)$$

The remaining differential equations for  $f$ ,  $g$ ,  $h$  and  $k$  (Equations 4.1b - 4.1e) all contain the term  $p^2$ , which can now be expressed with Equation 4.4. Firstly, this expression is substituted in the differential equations for  $f$  and  $g$ . After rearranging the terms, the resulting differential equations can be expressed as shown in Equations 4.7 and 4.8.

$$\frac{df}{dL} = -f_N \frac{\cos(L)}{2f_N L + \mu C_p} \quad (4.7)$$

$$\frac{dg}{dL} = -f_N \frac{\sin(L)}{2f_N L + \mu C_p} \quad (4.8)$$

The differential equations for  $f$  and  $g$  are now completely uncoupled and depend only on the variable  $L$ . Thus, these can be directly integrated analytically. When neglecting the scaling factors, one can see that the integral for  $df/dL$  has the following form:

$$\int \frac{\cos(x)}{ax + b} dx \quad (4.9)$$

The primitive of this function is obtained with Wolfram Mathematica and is shown in Equation 4.10.

$$\int \frac{\cos(x)}{ax + b} dx = \frac{\cos(b/a)Ci(b/a + x)}{a} + \frac{\sin(b/a)Si(b/a + x)}{a} + C \quad (4.10)$$

Two special functions appear in this primitive, namely  $Si(x)$  and  $Ci(x)$ . These will be discussed in more detail in Section 4.2.

Applying the above generalization to Equation 4.7 results in an expression for  $f$  as shown in Equation 4.11.

$$f(L) = -\frac{1}{2} \left[ \cos\left(\frac{\mu C_p}{2f_N}\right) Ci\left(\frac{\mu C_p}{2f_N} + L\right) + \sin\left(\frac{\mu C_p}{2f_N}\right) Si\left(\frac{\mu C_p}{2f_N} + L\right) \right] + C_f \quad (4.11)$$

Again, the constant  $C_f$  can be found by using the initial condition  $f(L_0) = f_0$ .

$$C_f = f_0 + \frac{1}{2} \left[ \cos\left(\frac{\mu C_p}{2f_N}\right) Ci\left(\frac{\mu C_p}{2f_N} + L_0\right) + \sin\left(\frac{\mu C_p}{2f_N}\right) Si\left(\frac{\mu C_p}{2f_N} + L_0\right) \right] \quad (4.12)$$

The differential equation of  $g$  takes a similar form, with the primitive shown in Equation 4.13.

$$\int \frac{\sin(x)}{ax + b} dx = \frac{\cos(b/a)Si(b/a + x)}{a} - \frac{\sin(b/a)Ci(b/a + x)}{a} + C \quad (4.13)$$

The expression for  $g$  is then given by Equation 4.14.

$$g(L) = -\frac{1}{2} \left[ \cos\left(\frac{\mu C_p}{2f_N}\right) Si\left(\frac{\mu C_p}{2f_N} + L\right) - \sin\left(\frac{\mu C_p}{2f_N}\right) Ci\left(\frac{\mu C_p}{2f_N} + L\right) \right] + C_g \quad (4.14)$$

The integration coefficient is given by Equation 4.15.

$$C_g = g_0 + \frac{1}{2} \left[ \cos\left(\frac{\mu C_p}{2f_N}\right) Si\left(\frac{\mu C_p}{2f_N} + L_0\right) + \sin\left(\frac{\mu C_p}{2f_N}\right) Ci\left(\frac{\mu C_p}{2f_N} + L_0\right) \right] \quad (4.15)$$

Finally, the elements  $h$  and  $k$  remain to be integrated. Substituting Equation 4.4 in Equations 4.1d and 4.1e and rearranging the terms results in Equations 4.16 and 4.17.

$$\frac{dh}{dL} = -f_W(1 + h^2 + k^2) \frac{\cos(L)}{8f_N L + 4\mu C_p} \quad (4.16)$$

$$\frac{dk}{dL} = -f_W(1 + h^2 + k^2) \frac{\sin(L)}{8f_N L + 4\mu C_p} \quad (4.17)$$

However, these are still coupled by the term  $(1 + h^2 + k^2)$ . Using Equations 3.4d and 3.4e, this term can be rewritten as  $1 + \tan^2(i/2)$ . The behaviour of this term shows little variation over time, especially when the inclination does not vary too much over time. However, although the modified equinoctial elements do not have a singularity at zero inclination, they do have a singularity at  $i = 180$  degrees, in which case the tangent goes to infinity. Nevertheless, as a first approximation and without considering inclinations near 180 degrees, the term can be set to its initial value  $(1 + h_0^2 + k_0^2)$ . In this way, the equations decouple and are integrated as:

$$h(L) = C_h - \frac{1}{8} \tan(\alpha)(1 + h_0^2 + k_0^2) \left[ \cos\left(\frac{\mu C_p}{2f_N}\right) Ci\left(\frac{\mu C_p}{2f_N} + L\right) + \sin\left(\frac{\mu C_p}{2f_N}\right) Si\left(\frac{\mu C_p}{2f_N} + L\right) \right] \quad (4.18)$$

with,

$$C_h = h_0 + \frac{1}{8} \tan(\alpha)(1 + h_0^2 + k_0^2) \left[ \cos\left(\frac{\mu C_p}{2f_N}\right) Ci\left(\frac{\mu C_p}{2f_N} + L\right) + \sin\left(\frac{\mu C_p}{2f_N}\right) Si\left(\frac{\mu C_p}{2f_N} + L\right) \right] \quad (4.19)$$

and,

$$k(L) = C_k - \frac{1}{8} \tan(\alpha)(1 + h_0^2 + k_0^2) \left[ \cos\left(\frac{\mu C_p}{2f_N}\right) Si\left(\frac{\mu C_p}{2f_N} + L\right) - \sin\left(\frac{\mu C_p}{2f_N}\right) Ci\left(\frac{\mu C_p}{2f_N} + L\right) \right] \quad (4.20)$$

with,

$$C_k = k_0 + \frac{1}{8} \tan(\alpha)(1 + h_0^2 + k_0^2) \left[ \cos\left(\frac{\mu C_p}{2f_N}\right) Si\left(\frac{\mu C_p}{2f_N} + L\right) - \sin\left(\frac{\mu C_p}{2f_N}\right) Ci\left(\frac{\mu C_p}{2f_N} + L\right) \right] \quad (4.21)$$

## 4.2. Special Functions: Sine and Cosine Integral

In the resulting equations for  $f$ ,  $g$ ,  $h$  and  $k$ , as discussed in the previous section, the special functions  $Si(x)$  and  $Ci(x)$  appear. These are the sine and cosine integral, respectively, and their definition is shown in Equations 4.22 and 4.23 [34].

$$Si(x) = \int_0^x \frac{\sin(s)}{s} ds \quad (4.22)$$

$$Ci(x) = -\int_x^\infty \frac{\cos(s)}{s} ds \quad (4.23)$$

The cosine integral can also be expressed as [35]:

$$Ci(x) = \gamma + \ln(x) + \int_0^x \frac{\cos(s) - 1}{s} ds \quad (4.24)$$

In the above equation,  $\gamma$  is Euler's constant (0.577) and  $0 < \arg x < \pi$ . For negative  $x$ , the following properties hold [35][36]:

$$Si(-x) = -Si(x) \quad (4.25)$$

$$Ci(-x) = Ci(x) \pm i\pi \quad (4.26)$$

The property in Equation 4.26 can be explained by looking at Equation 4.24. If the argument of the cosine integral is negative,  $\ln(x)$  has a negative argument too. This can be rewritten as follows:

$$\ln(-x) = \ln(-1) + \ln(x) \quad (4.27)$$

In the real plane,  $\ln(-1)$  is not defined. However, in the imaginary plane, the following relationship holds:

$$-1 = e^{\pm i\pi} \quad (4.28)$$

Then, it logically follows that:

$$\ln(-1) = \pm i\pi \quad (4.29)$$

Notice that  $i\pi$  can either be positive or negative; both represent an angle of 180 degrees, rotating either clockwise or counterclockwise in the imaginary plane, but arriving at the same value  $-1 + 0i$ . For the remaining of this section, the positive value will be taken. The two functions are plotted in Figure 4.1.

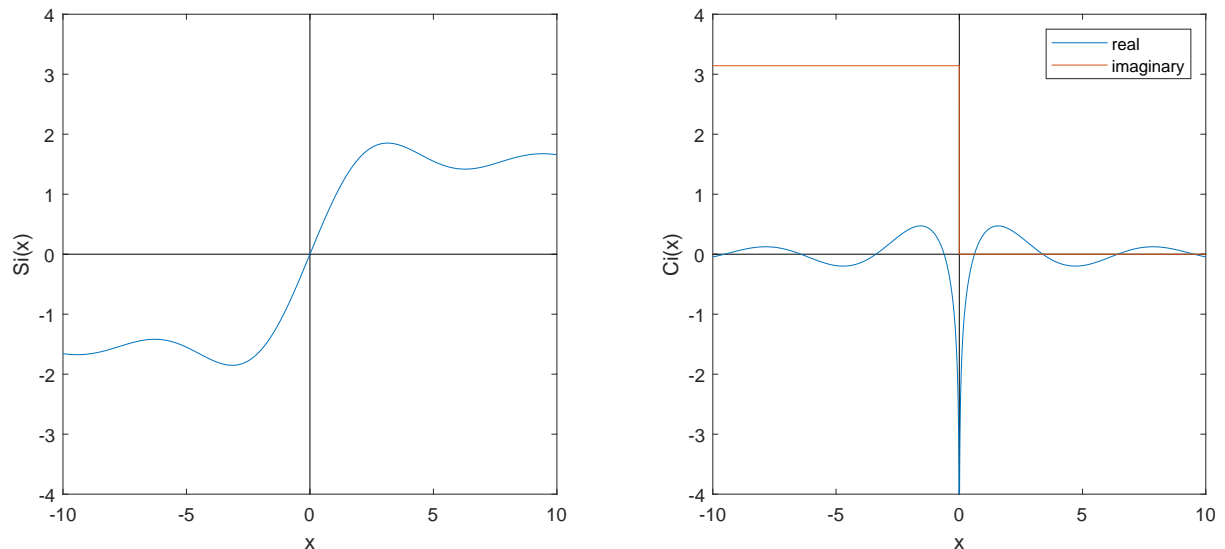
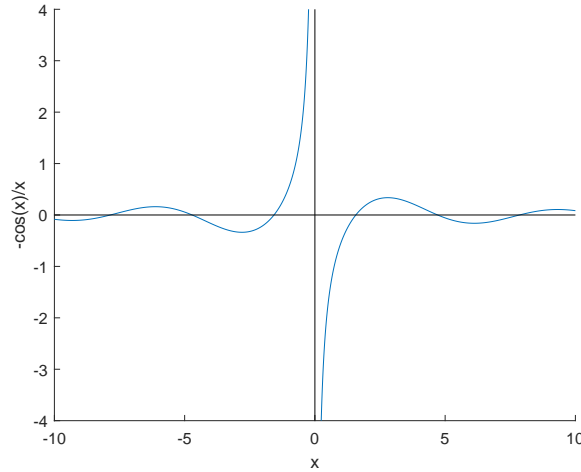


Figure 4.1: The special functions  $Si(x)$  and  $Ci(x)$ .

Since imaginary numbers do not occur in the real world, it is worth to further look into the cosine integral before limiting the solutions to positive arguments only. The function  $\frac{-\cos(x)}{x}$ , which is integrated to arrive at the cosine integral (see Equation 4.23), is plotted in Figure 4.2.

Figure 4.2: A snapshot of the function  $-\cos(x)/x$ .

Looking at Figure 4.2, it can be seen that this function is odd, having the following property:

$$f(x) = -f(-x) \quad (4.30)$$

It is therefore expected that if this function is integrated from  $-x$  to  $+x$ , the resulting value will be zero. However, a singularity appears at  $x = 0$ , where a vertical asymptote is present. This is where the imaginary number comes in when integrating the function from  $x < 0$  to infinity.

The singularity can be avoided by using the Cauchy's principal value, which is defined as shown in Equation 4.31, with  $a \leq c \leq b$  [37].

$$PV \left[ \int_a^b f(x) dx \right] = \lim_{\epsilon \rightarrow 0^+} \left[ \int_a^{c-\epsilon} f(x) dx + \int_{c+\epsilon}^b f(x) dx \right] \quad (4.31)$$

If the cosine integral has a negative argument, the integral can be split as:

$$Ci(-x) = - \int_{-x}^{\infty} \frac{\cos(s)}{s} ds = - \int_{-x}^x \frac{\cos(s)}{s} ds - \int_x^{\infty} \frac{\cos(s)}{s} ds \quad (4.32)$$

The principal value of  $Ci(-x)$  is then found by taking the principal value of the first integral, which contains the singularity at  $x = 0$ :

$$\begin{aligned} PV \left[ Ci(-x) \right] &= PV \left[ - \int_{-x}^x \frac{\cos(s)}{s} ds \right] - \int_x^{\text{inf}} \frac{\cos(s)}{s} ds = \dots \\ &= \lim_{\epsilon \rightarrow 0^+} \left[ - \int_{-x}^{0-\epsilon} \frac{\cos(s)}{s} ds - \int_{0+\epsilon}^x \frac{\cos(s)}{s} ds \right] - \int_x^{\text{inf}} \frac{\cos(s)}{s} ds = \dots \\ &= 0 - \int_x^{\text{inf}} \frac{\cos(s)}{s} ds = Ci(x) \end{aligned} \quad (4.33)$$

Since the function  $\frac{-\cos(x)}{x}$  is odd, the limit becomes zero, such that the remaining function is equal to  $Ci(x)$ , i.e. the positive argument. Thus, in the practical implementation of the cosine integral, the absolute value of the argument will be taken when evaluating the function. To test this proposal, a few function evaluations of the cosine integral are shown in Table 4.1, which shows that the positive and negative argument produce indeed the same results, not taking into consideration the imaginary part.

Table 4.1: Some function evaluations on the cosine integral.

x	Ci(x)	Ci(-x)
1	0.3374	0.3374 + 3.1416i
5	-0.1900	-0.1900 + 3.1416i
10	-0.0455	-0.0455 + 3.1416i
20	0.0444	0.0444 + 3.1416i
25	-0.0068	-0.0068 + 3.1416i

### 4.3. Tuning the Numerical Integrator

In order to assess the accuracy of the solutions obtained in Section 4.1, these will be compared to a numerical propagation of the trajectory. The numerical propagation will be done with Tudat (TU Delft Astrodynamics Toolbox). A variable step-size Runge-Kutta-Fehlberg 7(8) has been chosen for the integration, and Cowell's method will be used for the propagation to ensure robustness. A reference trajectory will be used throughout this report, the parameters of which are summarised in Table 4.2.

Table 4.2: The input parameters for the numerical reference trajectory.

parameter	value
$\mu_{sun}$	$1.327 \cdot 10^{20} \text{ m}^3/\text{s}^2$
a	$149.60 \cdot 10^9 \text{ m}$
e	0.0
i	20.0 deg
$\omega$	0.0 deg
$\Omega$	15.0 deg
$\nu$	0.0 deg
TOF	5 years
$\alpha$	20.0 deg
$f_{tot}$	$10^{-4} \text{ m/s}^2$

A spacecraft in orbit around the Sun is simulated, with its initial semi-major axis being equivalent to Earth's. The initial eccentricity is set to zero, since this is one of the assumptions made in Chapter 3. The argument of periapsis is also set to zero, although one has to keep in mind that this parameter is undefined for circular orbits. The inclination and longitude of the ascending node values are taken randomly. A relative long transfer time of 5 years is taken, since low-thrust transfers often tend to span several years. The steering angle is set to a value between -90 deg and 90 deg, such that the transfer orbit spirals outward, towards the outer Solar System. Finally, the thrust acceleration is set to  $10^{-4} \text{ m/s}^2$ .

The initial step size is set to 100 s, but is controlled by the error tolerance during the integration, since a variable step size is used. The error tolerance thus also defines the accuracy. Figure 4.3 shows the resulting modified equinoctial elements for tolerances ranging from  $10^{-1}$  to  $10^{-16}$ . The minimum and maximum step sizes are set to  $10^{-5}$  and  $10^{10}$ , respectively. Although the time of flight is set to 5 years, some of the numerical integrations in Figure 4.3 seem to stop at a later moment in time. This can be explained by the large step sizes that occurs at high tolerances. The integrator checks after every step if the final time has been achieved. However, if the step size is very large, the next moment in time at which the termination condition is checked is already far from the given time of flight. If a smaller step size is used, as is the case for lower tolerances, this overshoot is significantly smaller.

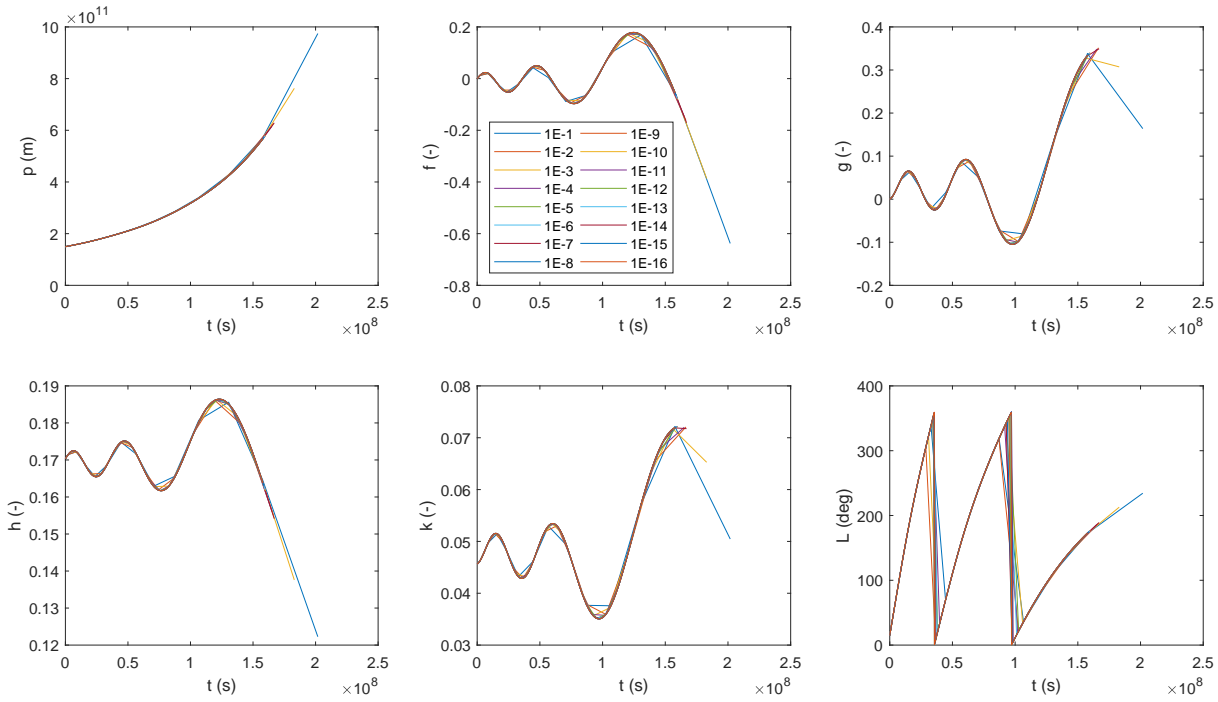
Figure 4.3: Numerical integration results for tolerances ranging from  $10^{-1}$  to  $10^{-16}$ .

Table 4.3 shows the maximum differences between two consecutive runs with different tolerances. Since a variable-step-size integrator is used, spline interpolation is used to be able to compare the resulting states at close but different epochs. As the tolerance decreases, i.e. the accuracy increases, the differences become increasingly smaller. Between tolerance  $10^{-15}$  and  $10^{-16}$ , the difference has become negligible. The difference in element  $p$  might seem quite large still, but is relatively insignificant compared to the scale of the problem ( $p \sim 10^{11}$  m). It can be concluded that an error tolerance of  $10^{-15}$  is sufficiently accurate for an assessment of the quality of the analytical solution, and thus this tolerance will be used for the remaining numerical integrations.

Table 4.3: The maximum differences in modified equinoctial elements between two numerical integrations with different tolerances.

tol. run 1	tol. run 2	$\Delta p$ (m)	$\Delta f$ (-)	$\Delta g$ (-)	$\Delta h$ (-)	$\Delta k$ (-)	$\Delta L$ (deg)
1E-1	1E-2	3.94E+09	9.35E-03	1.18E-02	5.51E-04	8.93E-04	1.56
1E-2	1E-3	1.07E+09	1.33E-02	8.03E-02	6.53E-04	8.21E-03	1.11
1E-3	1E-4	3.12E+08	9.03E-04	2.98E-03	1.36E-04	2.89E-04	8.01E-02
1E-4	1E-5	7.11E+07	7.27E-05	2.18E-03	1.11E-05	2.23E-04	8.53E-03
1E-5	1E-6	1.45E+07	1.01E-04	6.31E-04	6.03E-06	6.42E-05	5.00E-03
1E-6	1E-7	1.15E+08	6.72E-04	3.53E-03	9.22E-05	3.60E-04	4.93E-03
1E-7	1E-8	2.23E+06	2.52E-05	4.46E-05	2.92E-06	4.59E-06	2.39E-04
1E-8	1E-9	8.38E+05	7.16E-06	2.41E-05	8.88E-07	2.47E-06	5.14E-05
1E-9	1E-10	3.45E+05	3.34E-06	8.57E-06	4.01E-07	8.78E-07	1.79E-05
1E-10	1E-11	1.20E+05	1.26E-06	2.53E-06	1.48E-07	2.61E-07	9.64E-06
1E-11	1E-12	1.04E+05	1.10E-06	2.11E-06	1.29E-07	2.17E-07	9.30E-06
1E-12	1E-13	4.38E+05	4.61E-06	9.13E-06	5.41E-07	9.38E-07	3.76E-05
1E-13	1E-14	8.62E+03	9.48E-08	1.55E-07	1.10E-08	1.60E-08	9.47E-07
1E-14	1E-15	2.61E+04	2.84E-07	4.95E-07	3.30E-08	5.10E-08	2.67E-06
1E-15	1E-16	4.33E+02	4.78E-09	7.62E-09	5.53E-10	7.86E-10	4.90E-08

With the numerical integration established, the behaviour of the term  $(1 + h^2 + k^2)$  can now be analyzed in more detail. In Section 4.1, this term has been assumed to be constant and equal to its initial value. Figure 4.4 shows that indeed this term does not vary much in time, with its maximum error being approximately 0.006 or 0.63%. Thus, it is expected that this assumption will still provide sufficiently accurate results.

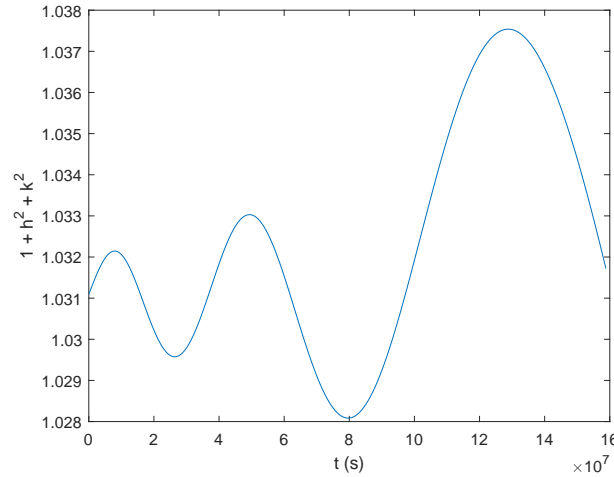


Figure 4.4: The behaviour of the term  $1 + h^2 + k^2$ .

#### 4.4. Results and Discussion

The analytical solution derived in Section 4.1 is implemented in C++. The GNU Scientific Library (GSL) is used for the special functions  $\text{Si}(x)$  and  $\text{Ci}(x)$ . The analytical results are compared to the numerical propagation, which is performed as discussed in the previous section. According to the range of thrust accelerations observed in Chapter 3, three thrust accelerations are selected for comparison:  $10^{-5}$ ,  $10^{-4}$  and  $10^{-3}$   $\text{m/s}^2$ . The remaining input parameters are taken from Table 4.2.

In Figure 4.5, the modified equinoctial elements from both the numerical and the analytical solution are shown. The analytical solution seems to follow the numerical one reasonably well. The largest deviation can be seen in the element  $k$ , where the maximum absolute difference is around  $1.3 \cdot 10^{-4}$ . For  $p$ , the maximum difference is approximately  $1.2 \cdot 10^7$  km. Since the order of magnitude of the absolute differences varies greatly, it is helpful to look at the relative differences as well. These are computed using Equation 4.34, where  $x$  represents an arbitrary element.

$$\%diff = \frac{x_{analytical} - x_{numerical}}{x_{numerical}} \cdot 100\% \quad (4.34)$$

The relative difference for  $p$  is then 0.0075%, which is considered to be a good accuracy. The relative difference for  $k$  is 0.28%, which is also considered to be good, regarding that  $k$  shows the largest deviation in Figure 4.5.

To get a better physical understanding of the transfer orbit, the modified equinoctial elements are converted to Kepler elements. These are shown in Figure 4.6. Here, the largest deviation is noticed for the element  $\Omega$ . This corresponds to the large deviation of  $k$  of the modified equinoctial elements, since  $\Omega$  depends on this element (Equation 3.5e). The elements  $i$  and  $\omega$  also depend on  $k$  (Equations 3.5c and 3.5d), but the deviations are less visible for these elements. Still, the largest error for the Kepler elements occurs for  $\omega$ , being 4.1%. Overall, the differences between the numerical and analytical solutions are relatively small, with the maximum differences for  $a$  and  $i$  being just 0.01%. The maximum difference for the eccentricity is  $2.27 \cdot 10^{-4}$ , which can be regarded as negligible for first-order estimates.

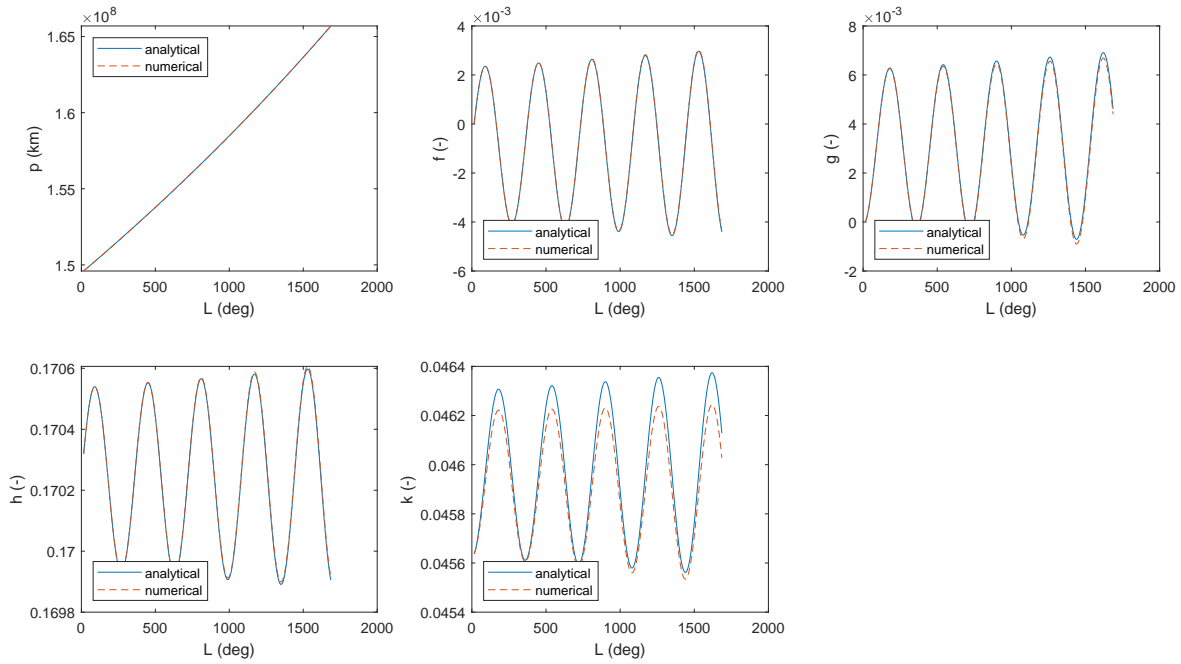


Figure 4.5: The modified equinoctial elements as a function of true longitude for a thrust acceleration of  $10^{-5} \text{ m/s}^2$ .

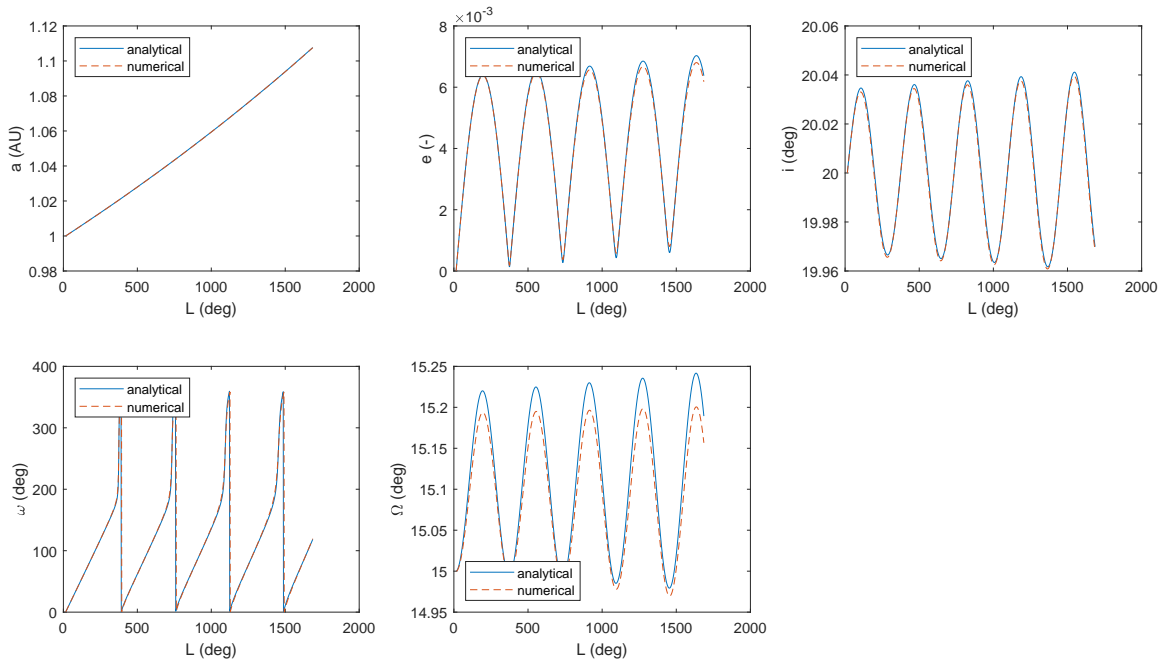


Figure 4.6: The Kepler elements as a function of true longitude for a thrust acceleration of  $10^{-5} \text{ m/s}^2$ .

Exploiting the analytical solution further, its behaviour is also analyzed for the higher thrust acceleration value of  $10^{-4} \text{ m/s}^2$ . Figure 4.7 shows the comparison in modified equinoctial elements, while the Kepler elements are shown in Figure 4.8. Larger differences are noticed in this case, especially towards the end of the propagation. The difference in semi-major axis goes up to 136.1%, and also the differences for  $\omega$  and  $\Omega$  are fairly high, being 13.6% and 53.0%. The difference for the inclination,

however, is 4.4%, which is relatively small compared to the other elements. It should be noticed that the inclination does not vary as much over time as  $\omega$  and  $\Omega$  do. Furthermore, the analytical solution seems to be continuously diverging, thus the difference would have been larger, if the time of flight would have been longer.

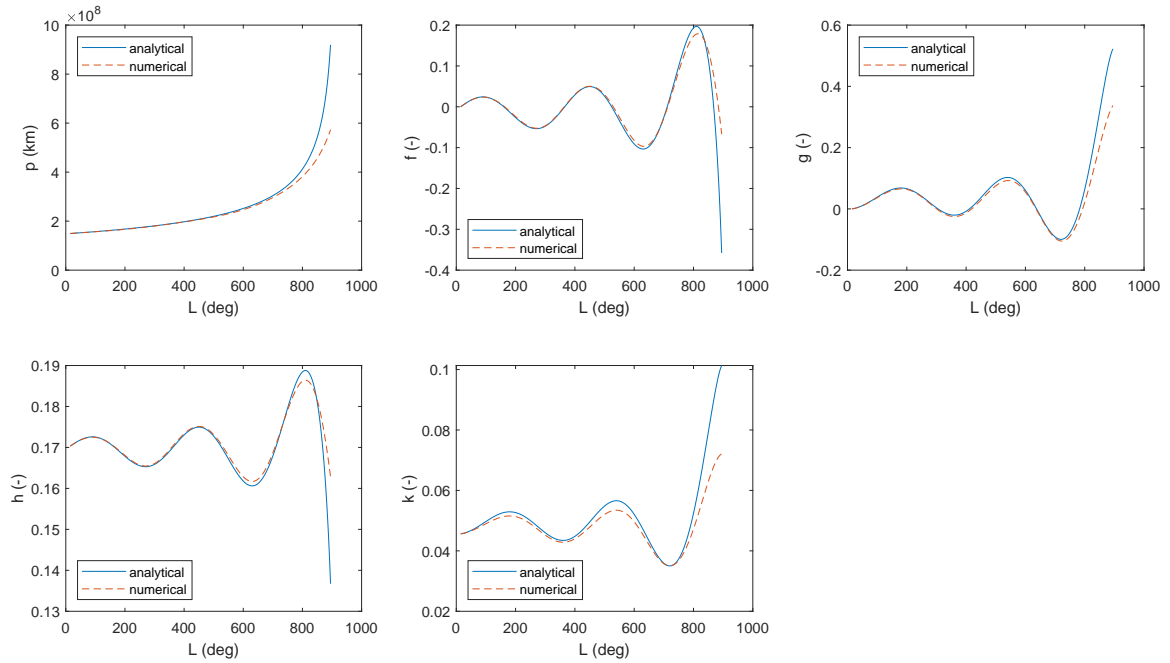


Figure 4.7: Modified equinoctial elements as a function of true longitude for a thrust acceleration of  $10^{-4}$  m/s<sup>2</sup>.

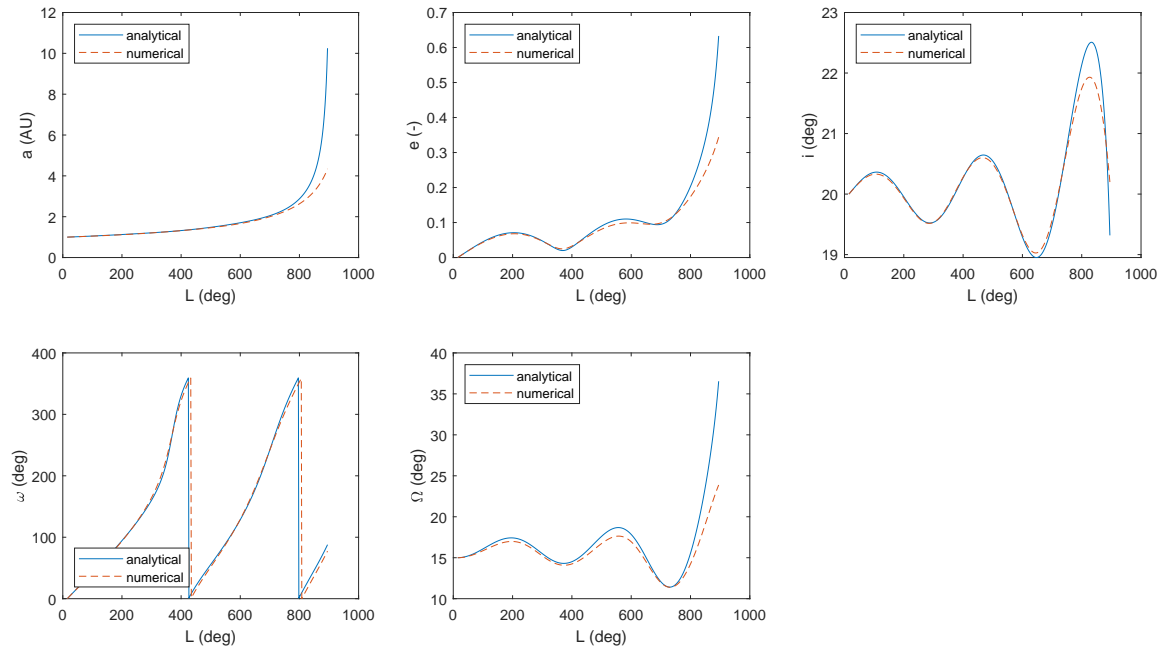


Figure 4.8: Kepler elements as a function of true longitude for a thrust acceleration of  $10^{-4}$  m/s<sup>2</sup>.

The analytical solutions for the case in Figures 4.7 and 4.8 clearly do not follow the numerical solution well. It seems like the analytical solution is tending towards extreme behaviour towards the end of the simulation. Looking more closely at the derivation in Section 4.1, it is noticed that the solution for  $p$  (Equation 4.5) only exists for  $4f_N L + 2\mu C_p < 0$ . The denominator is indeed initially negative ( $C_p$  is negative, conform Equation 4.6) but depends on the positive and increasing value of  $L$ . Thus, as the denominator approaches zero, the solution starts behaving asymptotically. Should the denominator cross zero and become positive, then the solution for  $p$  will become imaginary, since the square-root of a negative number will be taken. The squared solution for  $p$  is used in all subsequent derivations, such that all elements exhibit this asymptotic behaviour as the denominator approaches zero. Another parameter influencing the denominator is the thrust acceleration. The higher the thrust acceleration, the faster the denominator becomes positive.

The denominator for all three thrust accelerations is plotted in Figure 4.9. For  $f_{tot} = 10^{-5} \text{ m/s}^2$ , the denominator stays clear from the value zero, and therefore no extreme behaviour is noticed in Figures 4.5 and 4.6. For  $f_{tot} = 10^{-4} \text{ m/s}^2$  however, the slope of the denominator is significantly higher and approaches zero towards the end of the simulation, corresponding to the behaviours seen in Figures 4.7 and 4.8. For  $f_{tot} = 10^{-3} \text{ m/s}^2$ , the denominator crosses the zero value at just over  $L = 100$  degrees and becomes positive. Thus, it is expected that  $p$  will tend to infinity at this time as well and no physically reasonable solutions will be available from  $L = 100$  degrees onwards (actually, already slightly before).

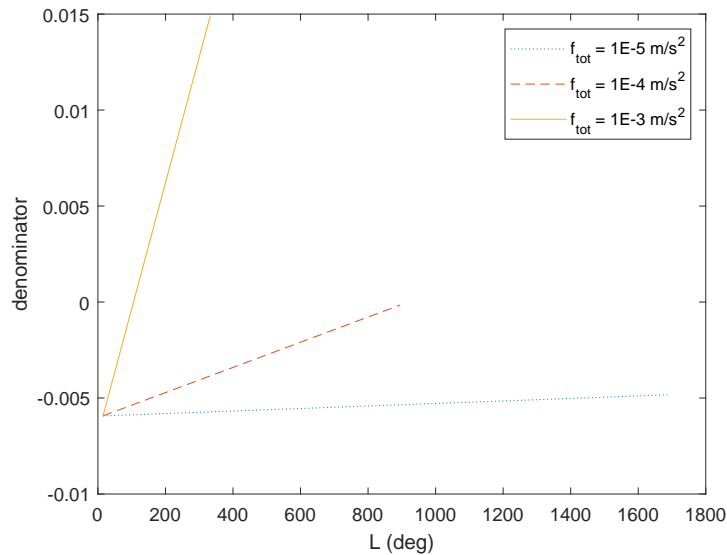


Figure 4.9: The denominator of Equation 4.5 for the thrust accelerations of  $10^{-5}$ ,  $10^{-4}$  and  $10^{-3} \text{ m/s}^2$ .

However, when analyzing the results for  $f_{tot} = 10^{-3} \text{ m/s}^2$ , which are depicted in Figure 4.10, it is not only the analytical solution that displays an interesting development. In addition, the numerical propagation shows some rather extreme behaviour, too. Translating the modified equinoctial elements into the more intuitive Kepler elements (Figure 4.11), one can see an exponential rise in eccentricity occurring after approximately 200 degrees. Another phenomenon has taken place during the transfer: the orbit has gone from elliptic through parabolic to become a very eccentric hyperbolic orbit. Also the semi-major axis shows this transition by the sharp peak that is noticeable when the eccentricity goes through one, after which it becomes negative. This can be more clearly seen in Figure 4.12, where the semi-major axis and eccentricity plots are zoomed in to provide a better picture of this point of interest. In this zoomed-in plot of the semi-major axis, it can also be seen that the prediction of the analytical solution stopping at just over  $L = 100$  degrees is justified. The remaining elements show a sharp peak at this point, indicating that the denominator has gone through zero, but do continue afterwards to produce (inaccurate) results. The reason for this is that although the solution  $p(L)$  contains a square root, the remaining elements contain the squared variable  $p^2$ , eliminating the square root and only having a singularity when the denominator is zero. Also, it is noticed that the analytical solution runs

'ahead' of the numerical solution, reaching the hyperbolic state around 100 degrees earlier. This is in agreement with the results for  $f_{tot} = 10^{-4} \text{ m/s}^2$  (Figure 4.8), where the analytical solution diverged increasingly towards the end, heading much faster towards  $e = 1$ .

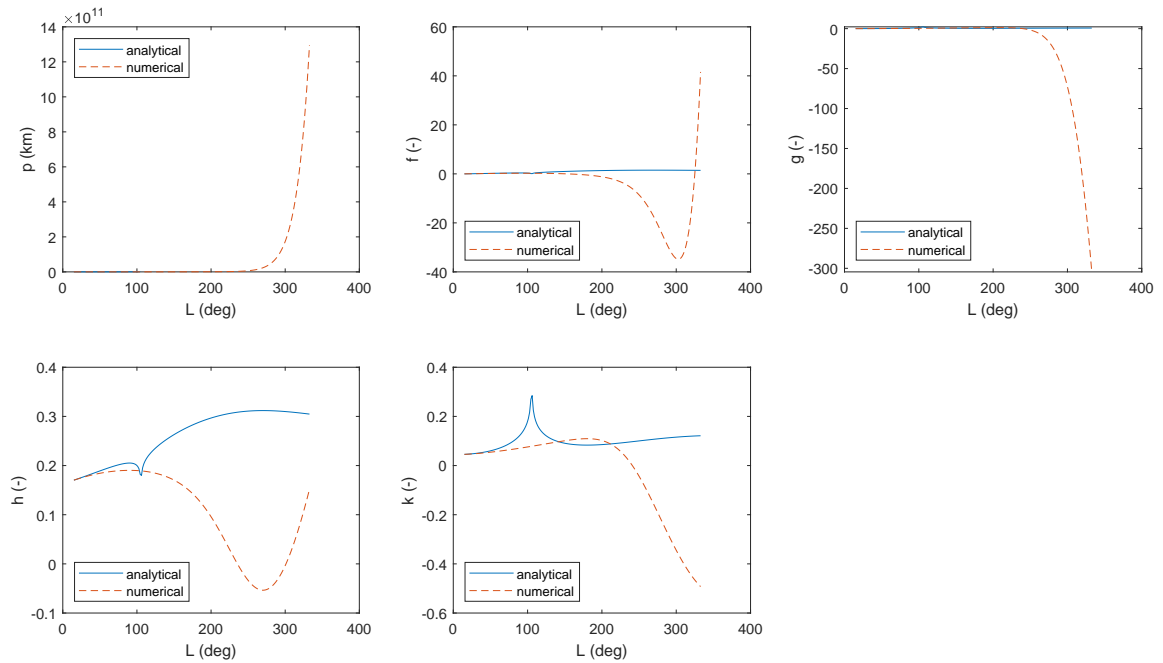


Figure 4.10: The modified equinoctial as a function of true longitude elements for a thrust acceleration of  $10^{-3} \text{ m/s}^2$ .

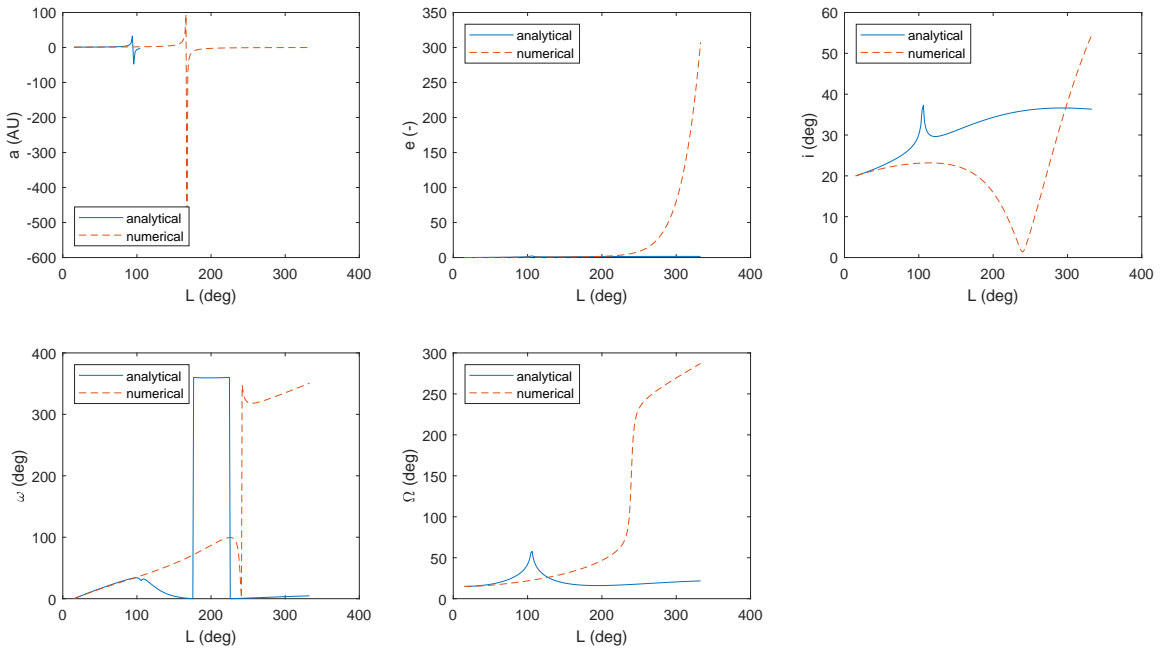


Figure 4.11: The Kepler elements as a function of true longitude for a thrust acceleration of  $10^{-3} \text{ m/s}^2$ .

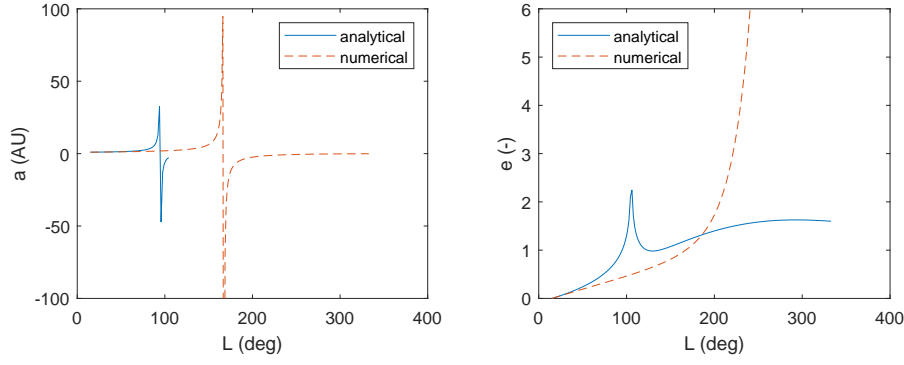


Figure 4.12: Zoom of the results for the semi-major axis and eccentricity for a thrust acceleration of  $10^{-3} \text{ m/s}^2$ .

Thus, it can be concluded that the analytical solution fails to portray the trajectory in the hyperbolic situation. This is not surprising, since one of the assumptions discussed in Chapter 3 was zero eccentricity. More importantly, the numerical solution shows that continuously thrusting at a level of  $10^{-3} \text{ m/s}^2$  for five years does not prove to be a realistic case, since a transfer that requires going from  $e = 0$  to  $e = 300$  is not expected to be part of a reasonable mission design. Therefore, this case will be omitted from further analysis.

For a better comparison of the remaining two cases (i.e.  $f_{tot} = 10^{-5}$  and  $10^{-4} \text{ m/s}^3$ ), the absolute and relative differences are summarized in Table 4.4 and 4.5, respectively. Both the differences in modified equinoctial elements and Kepler elements are presented. Note that since the argument of periapsis is theoretically undefined for circular orbits, erratic results can occur when converting to Kepler elements while the eccentricity is still very small. Therefore, the difference in argument of periapsis is only taken into account when  $e > 0.001$ .

Table 4.4: The maximum absolute differences between the numerical solution and the analytical solution based on true longitude for the modified equinoctial elements (MEE) and Kepler elements (KE), with a time of flight of 5 years.

MEE	$f_{tot} = 10^{-5} \text{ m/s}^2$	$f_{tot} = 10^{-4} \text{ m/s}^2$	KE	$f_{tot} = 10^{-5} \text{ m/s}^2$	$f_{tot} = 10^{-4} \text{ m/s}^2$
$\Delta p$ (m)	1.23E+07	3.46E+11	$\Delta a$ (m)	1.28E+07	8.84E+11
$\Delta f$ (-)	7.39E-05	2.91E-01	$\Delta e$ (-)	2.27E-04	2.89E-01
$\Delta g$ (-)	2.23E-04	1.85E-01	$\Delta i$ (deg)	2.56E-03	8.79E-01
$\Delta h$ (-)	1.16E-05	2.61E-02	$\Delta \omega$ (deg)	8.93	1.05E+01
$\Delta k$ (-)	1.30E-04	2.92E-02	$\Delta \Omega$ (deg)	4.16E-02	1.27E+01

Table 4.5: The maximum differences in percentages between the numerical solution and the analytical solution based on true longitude for the modified equinoctial elements (MEE) and Kepler elements (KE), with a time of flight of 5 years.

MEE	$f_{tot} = 10^{-5} \text{ m/s}^2$	$f_{tot} = 10^{-4} \text{ m/s}^2$	KE	$f_{tot} = 10^{-5} \text{ m/s}^2$	$f_{tot} = 10^{-4} \text{ m/s}^2$
$\Delta p$	0.0075	60.4	$\Delta a$	0.01	136.1
$\Delta f$	5.0	433.5	$\Delta e$	3.34	84.1
$\Delta g$	3.7	54.8	$\Delta i$	0.01	4.4
$\Delta h$	0.0068	16.0	$\Delta \omega$	4.1	13.6
$\Delta k$	0.28	40.6	$\Delta \Omega$	0.27	53.0

From Tables 4.4 and 4.5 it can be concluded that the results are satisfactory for  $f_{tot} = 10^{-5} \text{ m/s}^2$ , with a maximum difference of only a few percent. For  $f_{tot} = 10^{-4} \text{ m/s}^2$  however, where large differences are observed, there is room for improvement. In particular, the asymptotic behaviour of the solution for  $p$  may be postponed or bypassed when a time-based solution is derived. Also, other assumptions may lead to more accurate results. Thus, a few possible options to improve the results are:

- Derive a time-based analytical solution
- Derive the equations with  $h$  and  $k$  as variables
- Assume that  $f$  and  $g$  are equal to their initial values
- If the eccentricity becomes too high, start a coast arc, such that the thrust may be resumed at a point that decreases the eccentricity

The first three points will be discussed in the next chapter, where a time-based approach to the derivation of the analytical solution is discussed. The final point is further elaborated in Chapter 6, where the bang-bang control constraint is addressed.

# 5

## Analytical Solution using Time

The previous chapter discussed an analytical solution of Gauss' planetary equations as a function of the true longitude  $L$ . However, the results show a limitation due to extreme behaviour as  $L$  increases caused by the denominator of the expression for  $p$ . This chapter follows a different approach to the derivation of the analytical solution, by using the variable  $t$  rather than  $L$ . This different approach may lead to better results by following the numerical propagation more closely. The derivation of the analytical solution is discussed in Section 5.1. A limitation of the result is found when no in-plane thrust is applied, i.e.  $f_N = 0$ . A new derivation for this special case is discussed in Section 5.2. Section 5.3 elaborates on the results of this time-based analytical solution. Alternative variations to this solution are discussed in Section 5.4.

### 5.1. General Solution

Inspecting the simplified EoMs once more as shown in Equations 3.9, it is noticed that the differential equation  $dp/dt$  does not need a change of variables in order to be solved. Equation 3.9a is repeated below for convenience.

$$\frac{dp}{dt} = 2p \sqrt{\frac{p}{\mu}} f_N \quad (5.1)$$

As a separation of variables is possible, both the left-hand and right-hand side can be integrated:

$$\int \frac{\sqrt{\mu}}{2} p^{-1.5} dp = \int f_N dt \quad (5.2)$$

Integrating both sides results in:

$$-\sqrt{\frac{\mu}{p}} = f_N t + C_p \quad (5.3)$$

Rewriting the above equation leads to the following analytical result of the semi-latus rectum as a function of time:

$$p(t) = \frac{\mu}{(f_N t + C_p)^2} \quad (5.4)$$

The integration constant  $C_p$  can be determined using the initial state of the spacecraft. Then, from Equation 5.3 it follows that:

$$C_p = -\sqrt{\frac{\mu}{p_0}} - f_N t_0 \quad (5.5)$$

Having  $p$  expressed as a function of time, it can be substituted in the differential equation of  $L$ . This is shown in Equation 5.6.

$$\frac{dL}{dt} = \sqrt{\mu p} \left( \frac{1}{p} \right)^2 = \frac{\sqrt{\mu}}{p^{3/2}} = \frac{\sqrt{\mu}}{\left( \frac{\mu}{(f_N t + C_p)^2} \right)^{3/2}} \quad (5.6)$$

Since  $dL/dt$  is only dependent on  $p$ , and  $p$  is a function of time, the above differential equation can be directly integrated. The result is shown in Equation 5.7.

$$L(t) = \frac{\sqrt{\mu}(f_N t + C_p)}{4f_N \left( \frac{\mu}{(f_N t + C_p)^2} \right)^{3/2}} + C_L \quad (5.7)$$

This equation can be rewritten as:

$$L(t) = \frac{(f_N t + C_p)((f_N t + C_p)^2)^{3/2}}{4f_N \mu} + C_L \quad (5.8)$$

In the above equation, the numerator of the fraction requires some attention. At first glance, one expects that it can be simplified to  $(f_N t + C_p)^4$ , however great care has to be taken of which sign the final expression will have. Looking in more detail, the term  $((f_N t + C_p)^2)^{3/2}$  is equivalent to  $(f_N t + C_p)^2 \sqrt{(f_N t + C_p)^2}$ . Thus, it will always result in a positive value. Therefore, the sign of the numerator is determined by the first term  $(f_N t + C_p)$ . Then, the expression for  $L$  can be written as:

$$L(t) = \frac{\text{sign}(f_N t + C_p)(f_N t + C_p)^4}{4f_N \mu} + C_L \quad (5.9)$$

where the term  $\text{sign}(x)$  indicates which sign (+1 or -1) of  $x$  should be taken. The integration constant is given by:

$$C_L = L_0 - \frac{\text{sign}(f_N t_0 + C_p)(f_N t_0 + C_p)^4}{4f_N \mu} \quad (5.10)$$

Both the solution for  $p$  and  $L$  can now be substituted in the differential equations of  $f$ ,  $g$ ,  $h$ , and  $k$ . The resulting equations for  $f$  and  $g$  are shown in Equation 5.11 and 5.12.

$$\begin{aligned} \frac{df}{dt} &= \sqrt{\frac{p}{\mu}} 2 \cos(L) f_N = \\ &= \frac{2}{\sqrt{\mu}} \sqrt{\frac{\mu}{(f_N t + C_p)^2}} \cos \left( \frac{(f_N t + C_p)((f_N t + C_p)^2)^{3/2}}{4f_N \mu} + C_L \right) f_N \end{aligned} \quad (5.11)$$

$$\begin{aligned} \frac{dg}{dt} &= \sqrt{\frac{p}{\mu}} 2 \sin(L) f_N = \\ &= \frac{2}{\sqrt{\mu}} \sqrt{\frac{\mu}{(f_N t + C_p)^2}} \sin \left( \frac{(f_N t + C_p)((f_N t + C_p)^2)^{3/2}}{4f_N \mu} + C_L \right) f_N \end{aligned} \quad (5.12)$$

The equations for  $f$  and  $g$  are once again decoupled, and thus can be directly solved. Let

$$S = \text{sign}(f_N t + C_p) \quad (5.13)$$

then,

$$f(t) = C_f + \frac{1}{2} S \left[ \cos(C_L) Ci \left( \frac{S(f_N t + C_p)^4}{4f_N \mu} \right) - \sin(C_L) Si \left( \frac{S(f_N t + C_p)^4}{4f_N \mu} \right) \right] \quad (5.14)$$

and,

$$g(t) = C_g + \frac{1}{2}S \left[ \sin(C_L)Ci \left( \frac{S(f_N t + C_p)^4}{4f_N \mu} \right) + \cos(C_L)Si \left( \frac{S(f_N t + C_p)^4}{4f_N \mu} \right) \right] \quad (5.15)$$

Substituting  $p(t)$  and  $L(t)$  in the differential equations for  $h$  and  $k$  results in Equations 5.16 and 5.17, respectively.

$$\frac{dh}{dt} = \frac{1}{2} \sqrt{\frac{p}{\mu}} (1 + h^2 + k^2) \cos(L) f_W = \quad (5.16)$$

$$= \frac{1}{2\sqrt{\mu}} \sqrt{\frac{\mu}{(f_N t + C_p)^2}} (1 + h^2 + k^2) \cos \left( \frac{(f_N t + C_p)((f_N t + C_p)^2)^{3/2}}{4f_N \mu} + C_L \right) f_W$$

$$\frac{dk}{dt} = \frac{1}{2} \sqrt{\frac{p}{\mu}} (1 + h^2 + k^2) \sin(L) f_W = \quad (5.17)$$

$$= \frac{1}{2\sqrt{\mu}} \sqrt{\frac{\mu}{(f_N t + C_p)^2}} (1 + h^2 + k^2) \sin \left( \frac{(f_N t + C_p)((f_N t + C_p)^2)^{3/2}}{4f_N \mu} + C_L \right) f_W$$

Consistent with the assumption made in Chapter 4, the term  $(1 + h^2 + k^2)$  will be fixed as a constant that is set to its initial state, therefore also decoupling the differential equations for  $h$  and  $k$ . Integration then leads to the results shown in Equations 5.18 and 5.19. The integration constants  $C_f$ ,  $C_g$ ,  $C_h$  and  $C_k$  can be determined in a similar way as  $C_L$ , using the initial state.

$$h(t) = C_h + \frac{1}{8} \tan(\alpha) (1 + h_0^2 + k_0^2) S \left[ \cos(C_L)Ci \left( \frac{S(f_N t + C_p)^4}{4f_N \mu} \right) - \sin(C_L)Si \left( \frac{S(f_N t + C_p)^4}{4f_N \mu} \right) \right] \quad (5.18)$$

$$k(t) = C_k + \frac{1}{8} \tan(\alpha) (1 + h_0^2 + k_0^2) S \left[ \sin(C_L)Ci \left( \frac{S(f_N t + C_p)^4}{4f_N \mu} \right) + \cos(C_L)Si \left( \frac{S(f_N t + C_p)^4}{4f_N \mu} \right) \right] \quad (5.19)$$

## 5.2. Thrust Perpendicular to the Orbital Plane

In some cases it is beneficial to thrust only in the direction perpendicular to the orbital plane (e.g. when a change in inclination is required). In this case,  $\alpha = 90$  or  $270$  deg, and the normal thrust acceleration  $f_N$  equals zero (Equation 3.10). However, when examining the solution for  $L(t)$  (Equation 5.9) in the previous section more carefully, one can see that this introduces a singularity in the solution, because  $f_N$  is present as a factor in the denominator. Subsequently, the solutions for  $f$ ,  $g$ ,  $h$  and  $k$  contain this singularity too. Therefore, the derivation as presented in Section 5.1 is not suitable for this special case.

Another solution may be derived when evaluating the simplified planetary equations as laid out in Equations 3.9 once more, setting  $f_N = 0$ . The resulting EoMs are shown in Equations 5.20.

$$\frac{dp}{dt} = 0 \quad (5.20a)$$

$$\frac{df}{dt} = 0 \quad (5.20b)$$

$$\frac{dg}{dt} = 0 \quad (5.20c)$$

$$\frac{dh}{dt} = \sqrt{\frac{p}{\mu}} \frac{(1 + h^2 + k^2) \cos(L)}{2} f_W \quad (5.20d)$$

$$\frac{dk}{dt} = \sqrt{\frac{p}{\mu}} \frac{(1 + h^2 + k^2) \sin(L)}{2} f_W \quad (5.20e)$$

$$\frac{dL}{dt} = \sqrt{\mu p} \left(\frac{1}{p}\right)^2 \quad (5.20f)$$

The derivatives of the first three elements become zero, implying that these remain constant and equal to their initial value. This is as expected, as the semi-major axis and eccentricity do not change when no in-plane thrust is applied, and  $p$ ,  $f$  and  $g$  are entirely defined by these Kepler elements. Moreover, since  $p$  is constant,  $dL/dt$  is also constant, making the solution for  $L$  linear with time:

$$L(t) = \frac{\sqrt{\mu}}{p_0 \sqrt{p_0}} t + C_L \quad (5.21)$$

with,

$$C_L = L_0 - \frac{\sqrt{\mu}}{p_0 \sqrt{p_0}} t_0 \quad (5.22)$$

The expression for  $L$  can be substituted in the remaining two differential equations for  $h$  and  $k$ . These are then only dependent on time, so that they can be directly integrated. This leads to:

$$\frac{dh}{dt} = \sqrt{\frac{p_0}{\mu}} \frac{1}{2} (1 + h_0^2 + k_0^2) \cos\left(\frac{\sqrt{\mu}}{p_0 \sqrt{p_0}} t + C_L\right) f_W \quad (5.23)$$

so,

$$h(t) = C_h + \frac{p_0^2}{\mu} \frac{1}{2} (1 + h_0^2 + k_0^2) \sin\left(\frac{\sqrt{\mu}}{p_0 \sqrt{p_0}} t + C_L\right) f_W \quad (5.24)$$

and,

$$\frac{dk}{dt} = \sqrt{\frac{p_0}{\mu}} \frac{1}{2} (1 + h_0^2 + k_0^2) \sin\left(\frac{\sqrt{\mu}}{p_0 \sqrt{p_0}} t + C_L\right) f_W \quad (5.25)$$

which results in,

$$k(t) = C_k - \frac{p_0^2}{\mu} \frac{1}{2} (1 + h_0^2 + k_0^2) \cos\left(\frac{\sqrt{\mu}}{p_0 \sqrt{p_0}} t + C_L\right) f_W \quad (5.26)$$

### 5.3. Results and Discussion

The analytical solutions derived in the previous sections are once again compared with the numerical propagation as presented in Section 4.3. To make a fair comparison between the currently discussed analytical solution and the one presented in the previous chapter, the same input parameters are used for the simulation (see Table 4.2). Also, the same values for the thrust acceleration are used ( $10^{-5}$  and  $10^{-4}$  m/s<sup>2</sup>).

First of all, the results for a total thrust acceleration of  $10^{-5}$  m/s<sup>2</sup> are analyzed. The comparisons between analytical and numerical solution in modified equinoctial and Kepler elements are shown in Figures 5.1 and 5.2, respectively. The results show a slight improvement for the maximum difference in inclination, going from  $2.56 \cdot 10^{-3}$  to  $4.96 \cdot 10^{-4}$  degrees. The largest improvement is noticed for the element  $p$ , of which the maximum difference has decreased by a factor of 3. Also  $a$ , which is directly related to  $p$ , shows a similar improvement. The results for eccentricity are slightly worse, going from  $2.27 \cdot 10^{-4}$  to  $2.29 \cdot 10^{-4}$ . However, this difference is considered to be negligible. The sixth Kepler element can be compared as well, since time is the independent parameter in this case. The maximum difference for the argument of latitude is 0.79 degrees, which is just 0.43%.

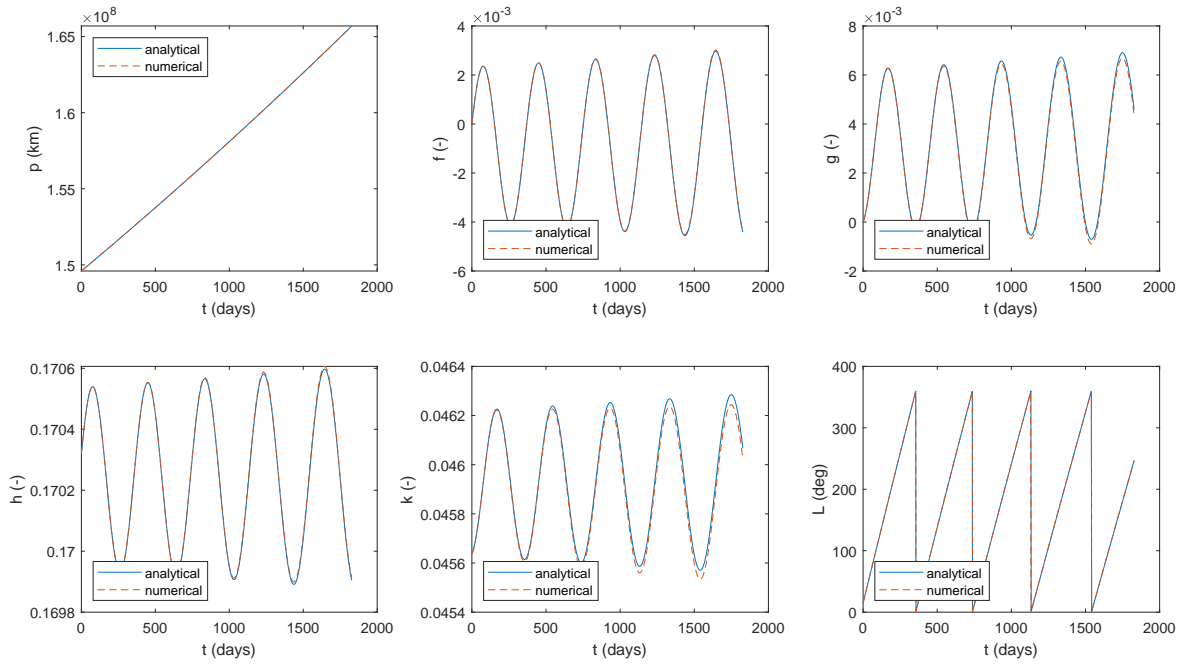


Figure 5.1: The modified equinoctial elements as function of time for a thrust acceleration of  $10^{-5} \text{ m/s}^2$ , with TOF = 5 years and  $\alpha = 20$  degrees.

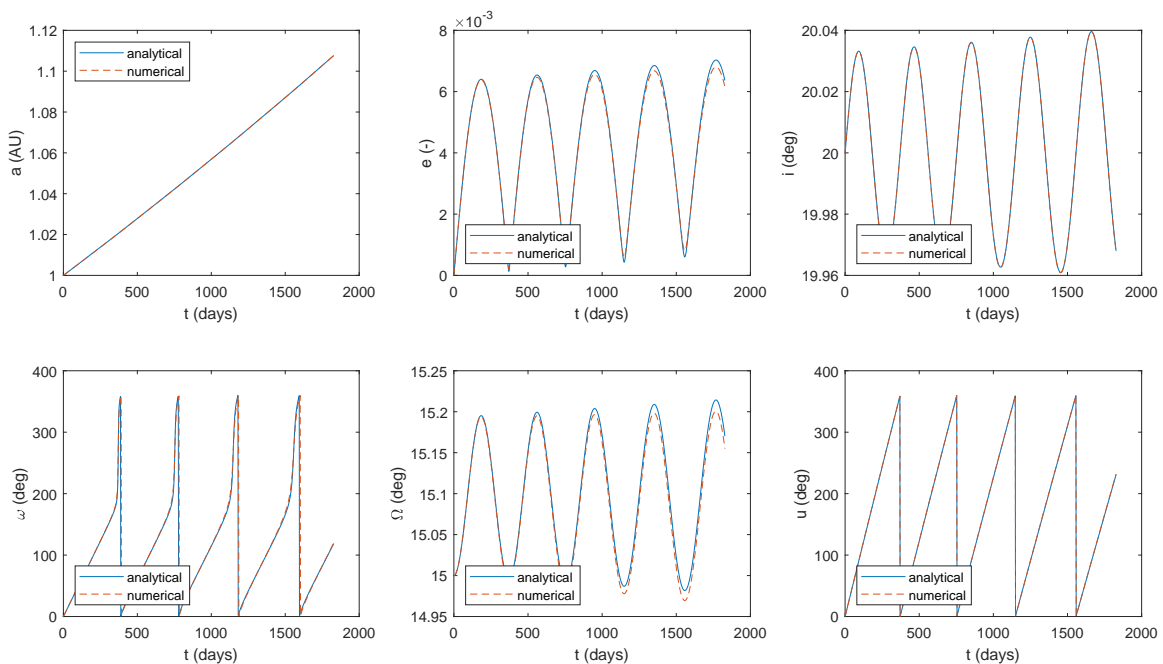


Figure 5.2: The Kepler elements as a function of time for a thrust acceleration of  $10^{-5} \text{ m/s}^2$ , with TOF = 5 years and  $\alpha = 20$  degrees.

More interestingly are the results for a total thrust acceleration of  $10^{-4} \text{ m/s}^2$ , since these results showed larger differences between numerical and analytical solution in the previous chapter. The results for the new analytical solution are shown in Figures 5.3 and 5.4.

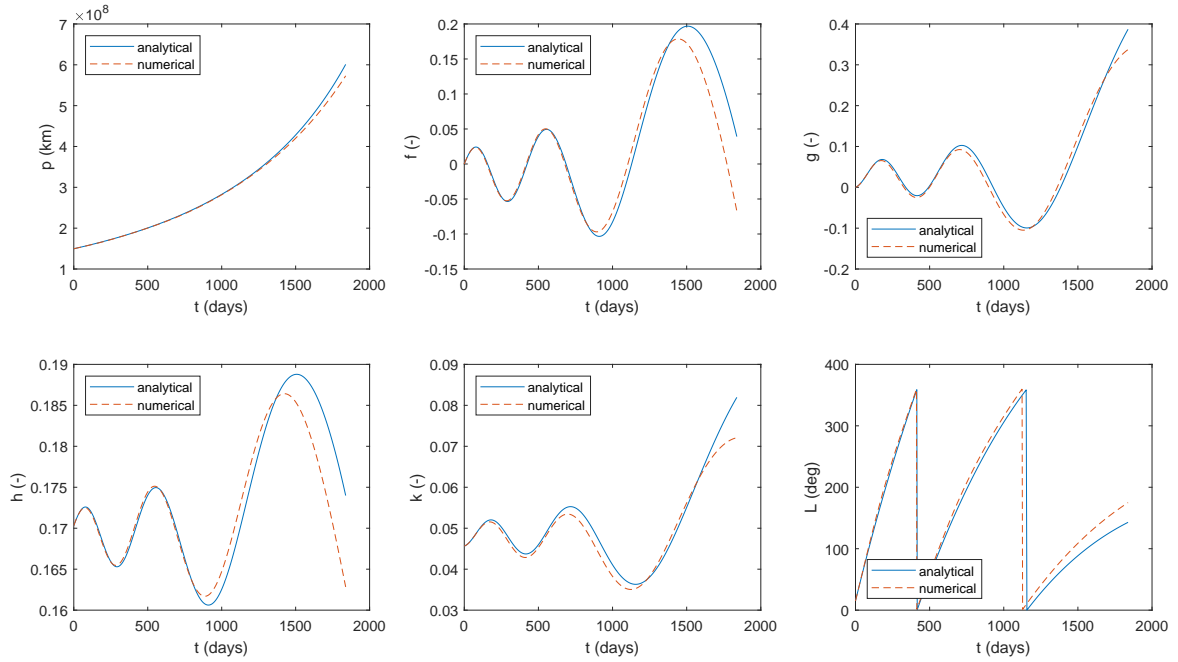


Figure 5.3: The modified equinoctial elements as a function of time for a thrust acceleration of  $10^{-4}$  m/s<sup>2</sup>, with TOF = 5 years and  $\alpha = 20$  degrees.

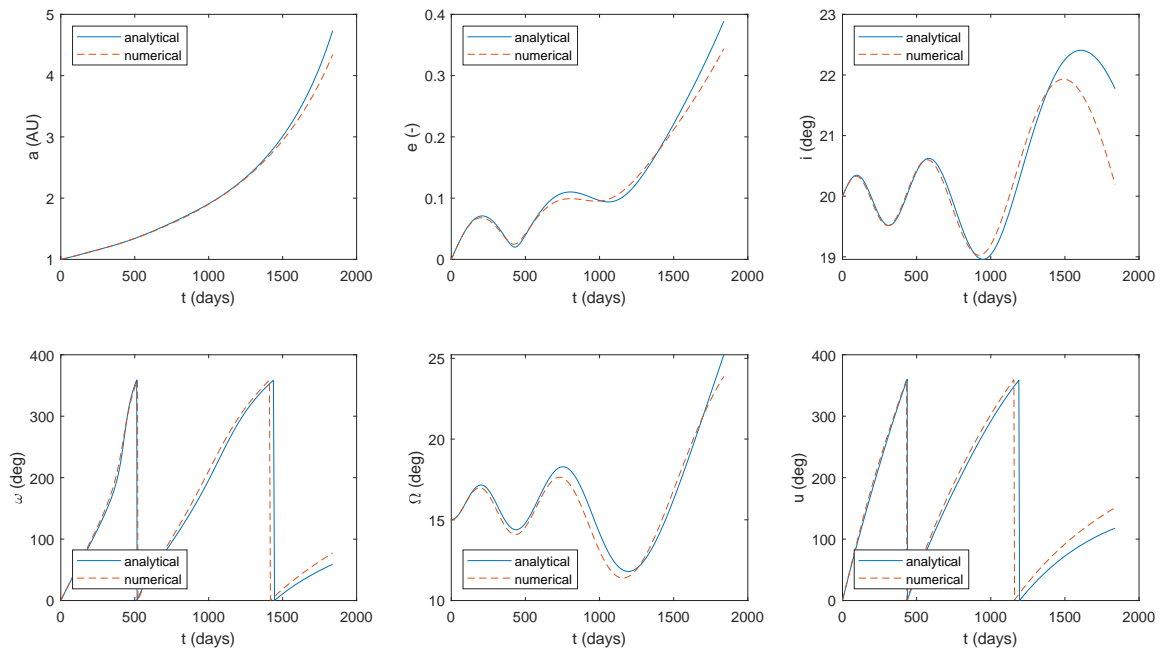


Figure 5.4: The Kepler elements as a function of time for a thrust acceleration of  $10^{-4}$  m/s<sup>2</sup>, with TOF = 5 years and  $\alpha = 20$  degrees.

When comparing Figure 5.3 with Figure 4.7, the time-based method shows a clear improved behaviour of the analytical solution. The analytical result for  $p$  follows the numerical result more closely and diverges less near the end of the simulation. The analytical solutions for  $f$  and  $g$  also seem to stay

closer to the values of the numerical solution, although a slight shift to the right is observed, especially for the element  $f$ . This also occurs in the results for  $h$  and  $k$ . When looking at the Kepler elements, also the behaviour of these results is improved (see Figures 5.4 and 4.8). In particular, the results for  $a$ ,  $e$  and  $\Omega$  are in better agreement. For  $i$  and  $\omega$ , the results seem to be slightly worse.

The maximum differences between the numerical and analytical solutions of the cases presented above are summarized in Tables 5.1 and 5.2 (absolute and relative, respectively). Overall, smaller differences are perceived compared to Tables 4.4 and 4.5, where the maximum errors of the true-longitude based analytical solution are shown. The improvement for  $a$  is evident, where the differences for  $f_{tot} = 10^{-4}$  m/s<sup>2</sup> differ by an order of magnitude. Also the  $e$  and  $\Omega$  show an improvement for this thrust value. The inclination however is slightly worse, going from 0.88 to 1.58 degrees. Also the argument of periaapsis, which goes from 10.5 to 18.4 degrees, is slightly less accurate. However, apart from these two values, the results show an overall increase in accuracy. Thus, the time-based analytical solution is to be preferred over the true-longitude-based solution.

Table 5.1: The maximum absolute differences between the numerical solution and the analytical solution based on time for the modified equinoctial elements (MEE) and Kepler elements (KE), with a time of flight of 5 years.

MEE	$f_{tot} = 10^{-5}$ m/s <sup>2</sup>	$f_{tot} = 10^{-4}$ m/s <sup>2</sup>	KE	$f_{tot} = 10^{-5}$ m/s <sup>2</sup>	$f_{tot} = 10^{-4}$ m/s <sup>2</sup>
$\Delta p$ (m)	3.69E+06	2.80E+10	$\Delta a$ (m)	4.21E+06	5.83E+10
$\Delta f$ (-)	5.78E-05	1.06E-01	$\Delta e$ (-)	2.29E-04	4.51E-02
$\Delta g$ (-)	2.53E-04	4.98E-02	$\Delta i$ (deg)	4.96E-04	1.58
$\Delta h$ (-)	1.06E-05	1.12E-02	$\Delta \omega$ (deg)	9.15	1.84E+01
$\Delta k$ (-)	4.56E-05	9.85E-03	$\Delta \Omega$ (deg)	1.51E-02	1.34
$\Delta L$ (deg)	7.75E-01	3.21E+01	$\Delta u$ (deg)	7.89E-01	3.34E+01

Table 5.2: The maximum differences in percentages between the numerical solution and the analytical solution based on time for the modified equinoctial elements (MEE) and Kepler elements (KE), with a time of flight of 5 years.

MEE	$f_{tot} = 10^{-5}$ m/s <sup>2</sup>	$f_{tot} = 10^{-4}$ m/s <sup>2</sup>	KE	$f_{tot} = 10^{-5}$ m/s <sup>2</sup>	$f_{tot} = 10^{-4}$ m/s <sup>2</sup>
$\Delta p$	0.0022	4.9	$\Delta a$	0.0025	9.0
$\Delta f$	7.2	158.1	$\Delta e$	3.4	13.1
$\Delta g$	5.8	14.8	$\Delta i$	0.0025	7.8
$\Delta h$	0.0062	6.9	$\Delta \omega$	4.2	23.8
$\Delta k$	0.10	13.7	$\Delta \Omega$	0.10	5.6
$\Delta L$	0.40	18.3	$\Delta u$	0.43	22.1

It seems that the solution for  $f_{tot} = 10^{-4}$  m/s<sup>2</sup> is not showing very extreme behaviour, but one has to keep in mind that the time period of five years was taken rather arbitrarily. If the time period were to be extended to ten years, the same pattern would show up as the results for  $f_{tot} = 10^{-3}$  m/s<sup>2</sup> in the previous chapter. In fact, the time at which the solutions reach their limit can be computed with Equation 5.27.

$$t_{limit} = \frac{-C_p}{f_N} \quad (5.27)$$

Using the definition for  $C_p$  as shown in Equation 5.5 and the initial conditions from Table 4.2 and setting  $f_{tot} = 10^{-4}$  m/s<sup>2</sup>, a limit time of 3668.5 days is computed. Looking at the results for a time period of ten years, which are shown in Figures 5.5 and 5.6, the plots indeed show a spike at this moment in time. As the orbit gets more and more hyperbolic, the semi-latus rectum increases more and more. At a certain point, the orbit will approach a straight line, and the semi-latus rectum will go to infinity. The limit of the analytical solutions thus represents a physical limit. However, this limit occurs much earlier than is seen from the numerical propagation, which does not yet show extreme behaviour. It has, however, reached an eccentricity of 4, and thus it has become a hyperbolic orbit. Taking into consideration that the analytical solution was derived for zero eccentricity, it is fair to say that the limit case is far outside its range of recommended operation.

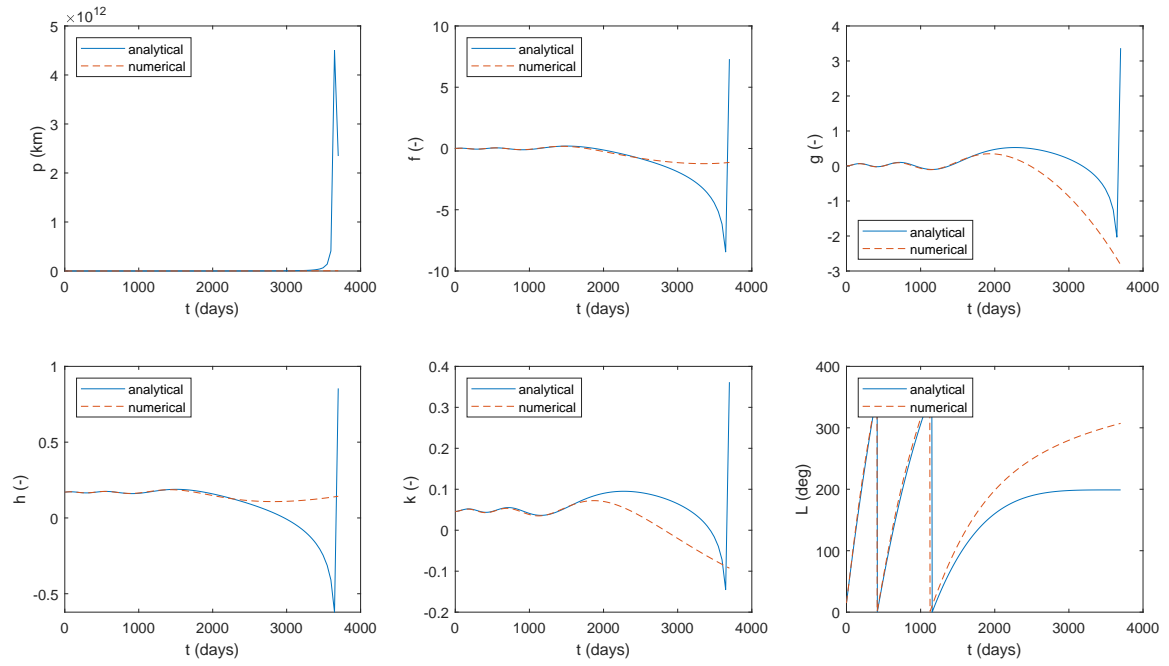


Figure 5.5: The modified equinoctial elements as a function of time for a thrust acceleration of  $10^{-4} \text{ m/s}^2$ , with TOF = 10 years and  $\alpha = 20$  degrees.

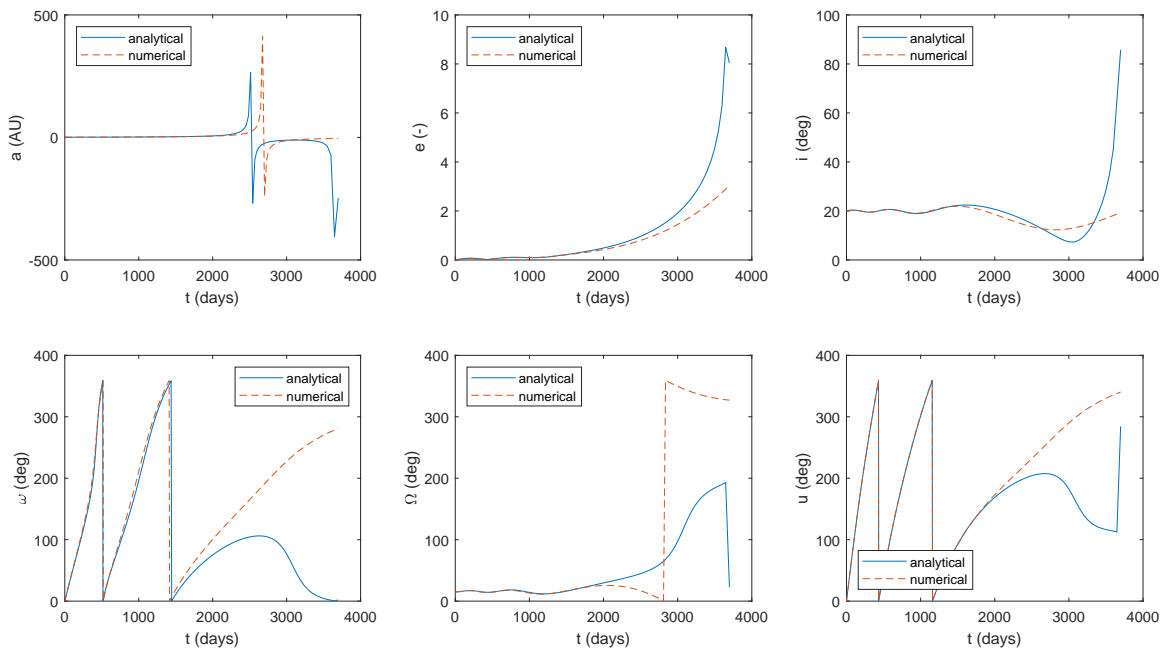


Figure 5.6: The Kepler elements as a function of time for a thrust acceleration of  $10^{-4} \text{ m/s}^2$ , with TOF = 10 years and  $\alpha = 20$  degrees.

So far, only outward motion has been considered for analysis. However, when  $\alpha$  is between 90 and 270 degrees, the semi-major axis of the orbit decreases as the spacecraft moves closer to the Sun. To also test this case,  $\alpha$  is set to 120 degrees. The results are shown in Figures 5.7 and 5.8.

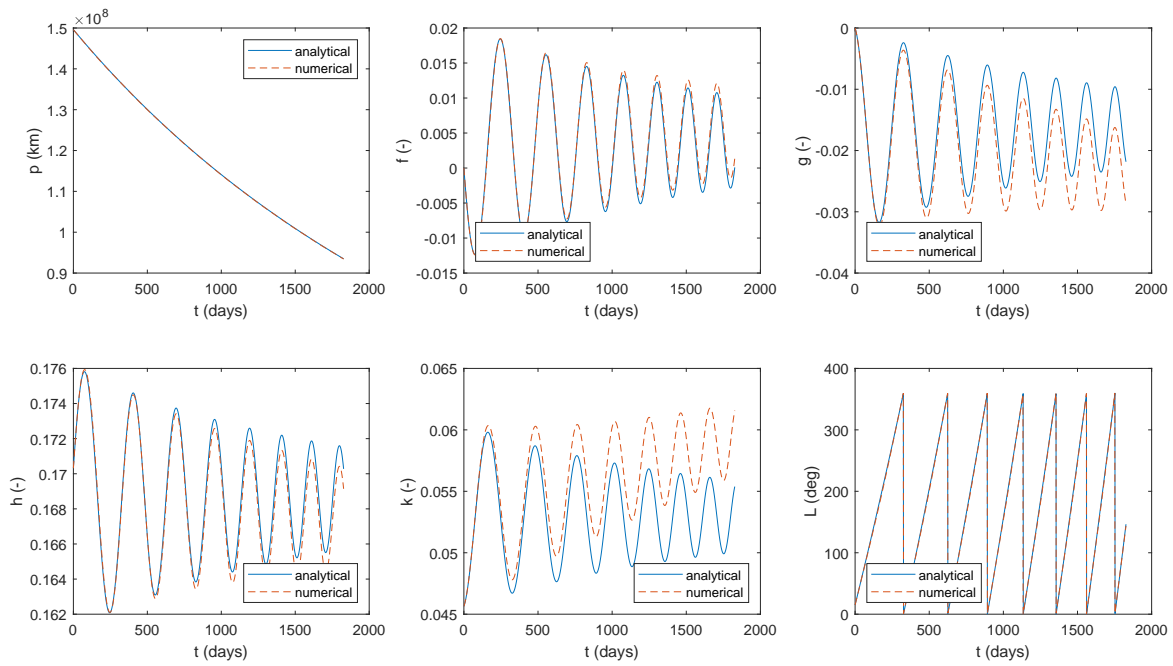


Figure 5.7: The modified equinoctial elements as a function of time for a thrust acceleration of  $10^{-4} \text{ m/s}^2$ , with TOF = 5 years and  $\alpha = 120$  degrees (inward motion).

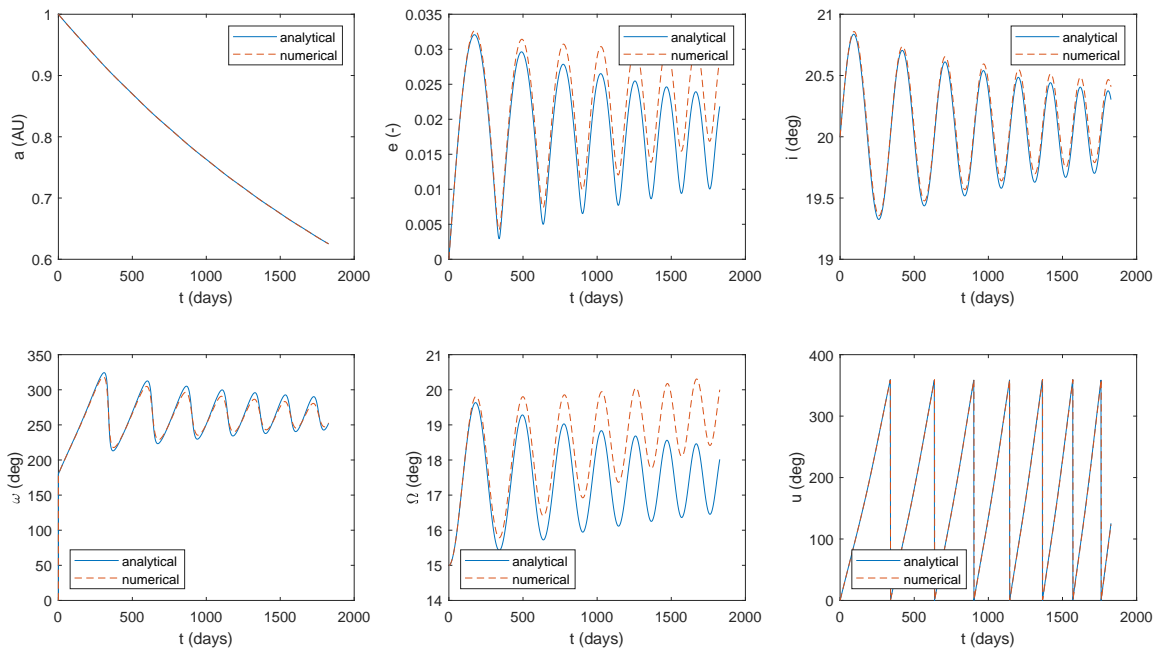


Figure 5.8: The Kepler elements as function of time for a thrust acceleration of  $10^{-4} \text{ m/s}^2$ , with TOF = 5 years and  $\alpha = 120$  degrees (inward motion).

The relative and absolute differences for both the modified equinoctial elements and the Kepler elements are shown in Table 5.3 for the case of inward motion ( $\alpha = 120$  deg). The most notable result is the eccentricity, that stays relatively contained compared to the results when  $\alpha = 20$  deg. Looking at Table 5.3, the absolute maximum error is indeed small, but the percentage error is 23.9%. These contrasting results can be explained by looking at Equation 4.34, with which the relative difference is computed. Since the eccentricity is near zero, the absolute difference, although being small, is also divided by a small number. This makes the resulting relative difference rather large, and is thus not a good measure of error. Therefore, the governing difference is the absolute one for the eccentricity.

Table 5.3: The maximum differences (absolute and in percentages) between the numerical solution and the analytical solution based on time for the modified equinoctial elements (MEE) and Kepler elements (KE), with a time of flight of 5 years and  $\alpha = 120$  degrees (inward motion).

MEE	absolute	relative	KE	absolute	relative
$\Delta p$ (m)	7.74E+07	0.054	$\Delta a$ (m)	7.21E+07	0.051
$\Delta f$ (-)	1.41E-03	-101.6	$\Delta e$ (-)	6.87E-03	23.9
$\Delta g$ (-)	6.84E-03	-23.8	$\Delta i$ (deg)	1.07E-01	0.53
$\Delta h$ (-)	1.18E-03	0.69	$\Delta \omega$ (deg)	1.04E+01	3.5
$\Delta k$ (-)	6.18E-03	10.0	$\Delta \Omega$ (deg)	1.98	9.9
$\Delta L$ (deg)	3.67	1.9	$\Delta u$ (deg)	1.98	1.6

Finally, the quality of the analytical solution derived in Section 5.2 for thrust perpendicular to the orbital plane is assessed. The results are shown in Figures 5.9 and 5.10. The numerical result closely follows the analytical result. For  $p$ ,  $f$  and  $g$ , the differences are negligible. The argument of periapsis is not taken into consideration, since this element is not defined for zero eccentricity. The maximum error in inclination is 0.05%, while the maximum error in  $\Omega$  is 0.12%. Thus,  $h$  and  $k$  are well approximated. The maximum error in  $u$  is 0.009%, which proves that the solution for true longitude is accurate as well.

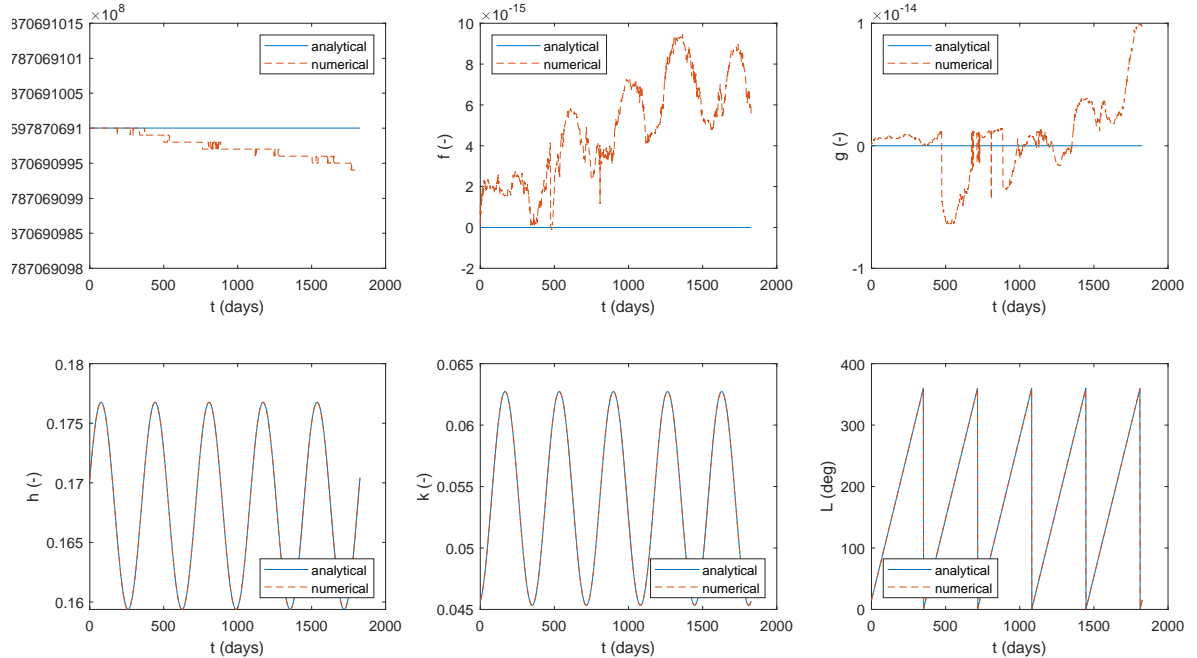


Figure 5.9: The modified equinoctial elements as a function of time for a thrust acceleration of  $10^{-4}$  m/s<sup>2</sup>, with TOF = 5 years and  $\alpha = 90$  degrees (analytical solution for thrust perpendicular to the orbital plane).

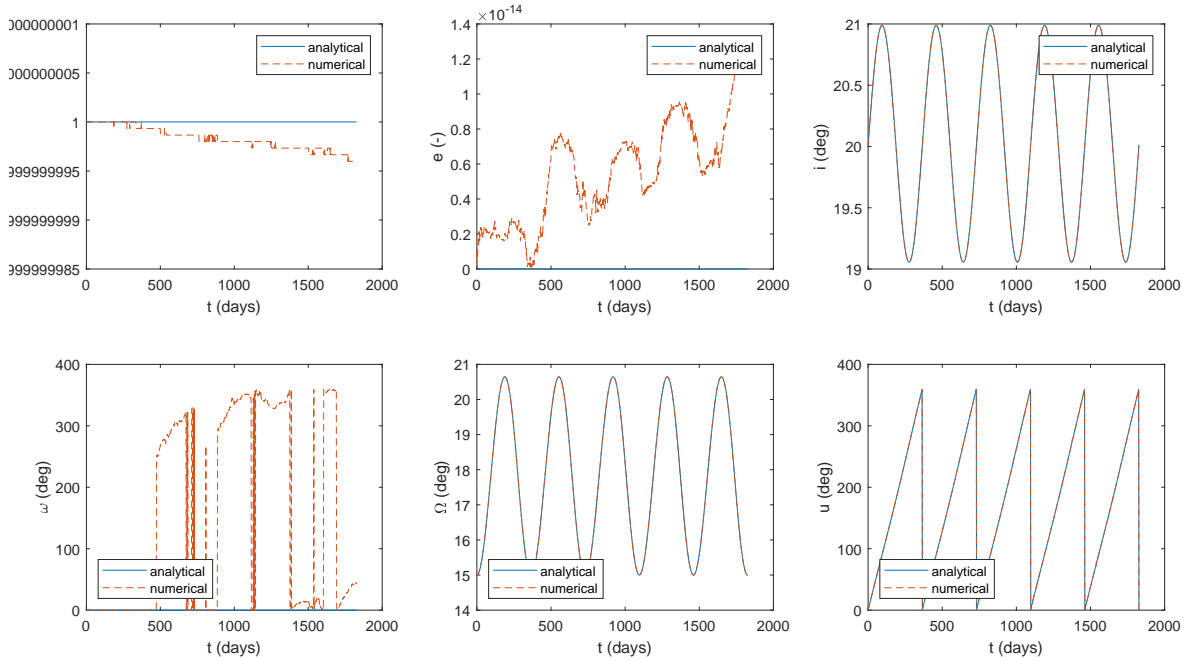


Figure 5.10: The Kepler elements as a function of time for a thrust acceleration of  $10^{-4}$  m/s<sup>2</sup>, with TOF = 5 years and  $\alpha = 90$  degrees (analytical solution for thrust perpendicular to the orbital plane).

In Section 2.2, an analytical method developed by Quarta and Mengali [17] was discussed, which modelled a transfer orbit with zero radial thrust acceleration. The radial distance was assumed to be approximately equal to the semi-latus rectum (Equation 2.34). It was concluded that the accuracy of the method depended on the magnitude of the applied thrust acceleration, as shown in Figure 2.7, and could be computed with Equation 2.37. For example, if the thrust acceleration was  $\tilde{a}_p = 0.5\%$ , then the maximum error would be  $\epsilon = 5\%$ , if  $r_m \approx 5$  ( $r_m = \sqrt{y_m}$ , with  $y_m$  being calculated numerically).

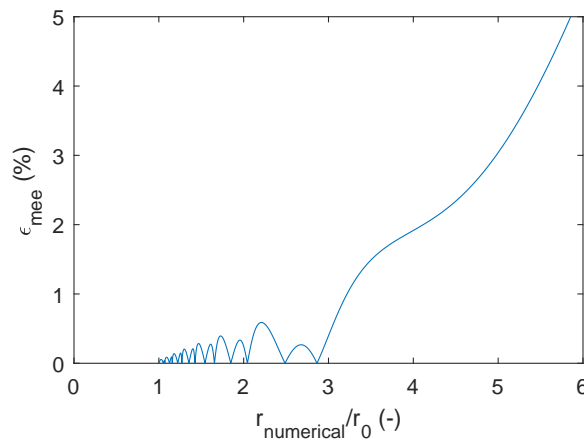


Figure 5.11: The error determined by Equation 5.28 as a function of the dimensionless radial distance.

To make the same comparison for the above developed analytical solution, the following equation could be used to compute the error:

$$\left| \frac{r_{numerical}}{p_{numerical}} - \frac{r_{analytical}}{p_{analytical}} \right| = \epsilon_{mee} \quad (5.28)$$

Using Equation 2.32c,  $\tilde{a}_p = 0.5\%$  corresponds for the heliocentric case with  $r_0 = 1$  AU to a thrust acceleration of approximately  $3 \cdot 10^{-5}$  m/s<sup>2</sup>. The steering angle is set to zero degrees, since only the planar case is addressed in [17]. Then, Equation 5.28 can be plotted against the dimensionless radial distance ( $r_{numerical}/r_0$ , which is equivalent to  $\tilde{r}_m$ ) as shown in Figure 5.11. For  $r_{numerical}/r_0 = 5$ ,  $\epsilon_{mee}$  is around 3%, which is less than 5%. Thus, the above derived analytical solution performs better than the analytical method developed in [17].

## 5.4. Variations

In an attempt to improve the results obtained in the previous section, variations of the solutions presented in Section 5.1 are investigated.

For the solutions of  $h$  and  $k$ , the term  $(1 + h^2 + k^2)$  was assumed to be constant in order to decouple the differential equations. An alternative way for decoupling is to assume just one of the variables constant, while the other is still allowed to vary, see Equations 5.29 and 5.30. By letting  $h$  be a variable in  $dh/dt$  and  $k$  be a variable in  $dk/dt$ , the two equations remain decoupled.

$$\frac{dh}{dt} = \sqrt{\frac{p}{\mu}} \frac{(1 + h^2 + k_0^2) \cos(L)}{2} f_W \quad (5.29)$$

$$\frac{dk}{dt} = \sqrt{\frac{p}{\mu}} \frac{(1 + h_0^2 + k^2) \sin(L)}{2} f_W \quad (5.30)$$

The differential equations can then be solved by separation of variables:

$$\frac{dh}{(1 + h^2 + k_0^2)} = \sqrt{\frac{p}{\mu}} \frac{\cos(L)}{2} f_W dt \quad (5.31)$$

$$\frac{dk}{(1 + h^2 + k^2)} = \sqrt{\frac{p}{\mu}} \frac{(1 + h_0^2 + k^2) \sin(L)}{2} f_W dt \quad (5.32)$$

Integration of Equations 5.31 and 5.32 leads to Equations 5.33 and 5.34, in which  $S$  is defined by Equation 5.13.

$$h(t) = \sqrt{1 + k_0^2} \tan \left( \sqrt{1 + k_0^2} \left\{ C_h + \frac{1}{8} \tan(\alpha) S \left[ \cos(C_L) Ci \left( \frac{S(f_N t + C_p)^4}{4f_N \mu} \right) - \sin(C_L) Si \left( \frac{S(f_N t + C_p)^4}{4f_N \mu} \right) \right] \right\} \right) \quad (5.33)$$

$$k(t) = \sqrt{1 + h_0^2} \tan \left( \sqrt{1 + h_0^2} \left\{ C_k + \frac{1}{8} \tan(\alpha) S \left[ \sin(C_L) Ci \left( \frac{S(f_N t + C_p)^4}{4f_N \mu} \right) + \cos(C_L) Si \left( \frac{S(f_N t + C_p)^4}{4f_N \mu} \right) \right] \right\} \right) \quad (5.34)$$

Figure 5.12 shows the resulting graphs from the numerical propagation, the analytical solution derived in Section 5.1 and its variation as depicted above. Again, the initial values from Table 4.2 are used. The inclination and longitude of the ascending node are also plotted, since these are directly influenced by  $h$  and  $k$ .

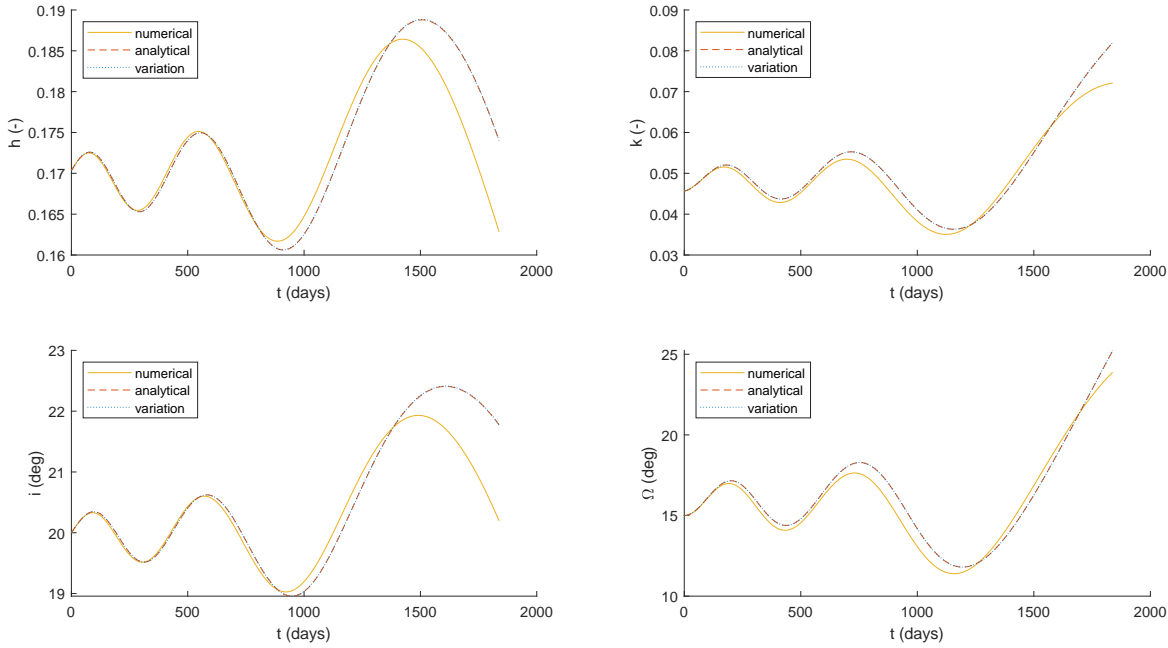


Figure 5.12: The behaviour of  $h$ ,  $k$ ,  $i$ ,  $\Omega$  resulting from the numerical propagation, the original analytical solution and the variation on the analytical solution with  $f_{tot} = 10^{-4} \text{ m/s}^2$ .

Figure 5.12 shows that the two analytical solutions lie very close together, thus the new approach on decoupling does not affect the results notably. When comparing both solutions with the numerical propagation, as seen in Table 5.4, the original analytical solution even proves to give slightly better results than its variation (although the difference is very small). Thus, no improvements have been reached by the alternative method of decoupling the differential equations for  $h$  and  $k$ .

Table 5.4: The maximum differences between the numerical propagation and the two analytical solutions for  $h$ ,  $k$ ,  $i$  and  $\Omega$ , both absolute and in percentages.

element	absolute differences		relative differences in %	
	original	variation	original	variation
$\Delta h$	1.12E-02	1.12E-02	6.9	6.9
$\Delta k$	9.85E-03	9.93E-03	13.7	13.8
$\Delta i$	1.58	1.58	7.8	7.8
$\Delta \Omega$	1.34	1.36	5.6	5.7

Inspired by the approach for  $h$  and  $k$  of setting variables to their initial values, the same assumption can be attempted for  $f$  and  $g$ . Of course, setting  $f$  and  $g$  to their initial values with the assumption that the eccentricity is equal to zero will naturally lead to the exact same results, since  $f_0 = g_0 = 0$ . However, when the eccentricity is slightly higher than zero, the analytical result starts deviating from the numerical result, as shown in Figure 5.13. In this figure, the eccentricity is set to 0.2, with the rest of the initial parameters being identical to the prior cases (with  $f_{tot} = 10^{-5} \text{ m/s}^2$ ). It seems that the numerical propagation shows a linear decrease as time increases, while the analytical solution continues to oscillate around the same equilibrium.

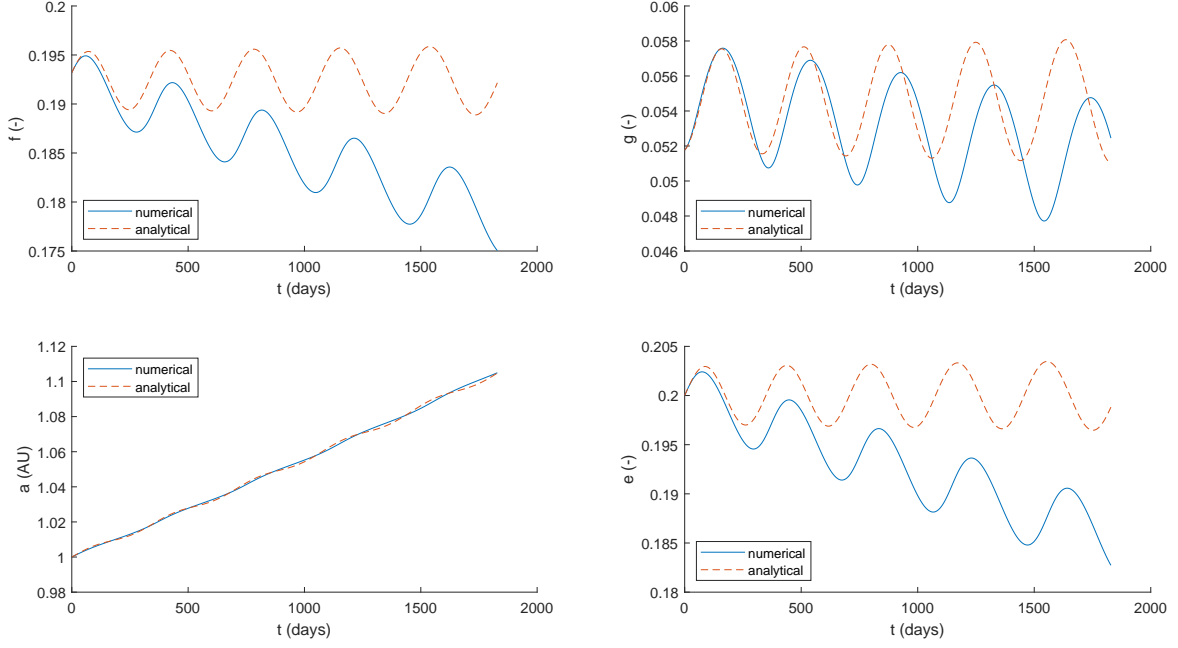


Figure 5.13: The behaviour of  $f$ ,  $g$ ,  $a$  and  $e$  resulting from the numerical propagation and the original analytical solution with  $f_{tot} = 10^{-5} \text{ m/s}^2$ .

Thus, if a linear term is introduced in the analytical derivation, the result may behave more similar to the numerical propagation. This linear term can be introduced by substituting the initial values of  $f$  and  $g$  in the first term on the right-hand side of their differential equations (Equations 3.6b and 3.6c). This leads Equations 5.35 and 5.36.

$$\frac{df}{dt} = \sqrt{\frac{p}{\mu}} \left[ \frac{1}{w_0} ((w_0 + 1) \cos(L) + f_0) f_N \right] \quad (5.35)$$

$$\frac{dg}{dt} = \sqrt{\frac{p}{\mu}} \left[ \frac{1}{w_0} ((w_0 + 1) \sin(L) + g_0) f_N \right] \quad (5.36)$$

Integrating the above expressions leads to Equations 5.37 and 5.38.

$$f(t) = C_f + \frac{(w_0 + 1)}{4w_0} S \left[ \cos(C_L) Ci \left( \frac{S(f_N t + C_p)^4}{4f_N \mu} \right) - \sin(C_L) Si \left( \frac{S(f_N t + C_p)^4}{4f_N \mu} \right) + \frac{4f_0}{(w_0 + 1)} \ln |f_N t + C_p| \right] \quad (5.37)$$

$$g(t) = C_g + \frac{(w_0 + 1)}{4w_0} S \left[ \sin(C_L) Ci \left( \frac{S(f_N t + C_p)^4}{4f_N \mu} \right) + \cos(C_L) Si \left( \frac{S(f_N t + C_p)^4}{4f_N \mu} \right) + \frac{4g_0}{(w_0 + 1)} \ln |f_N t + C_p| \right] \quad (5.38)$$

These new analytical solutions are plotted in Figure 5.14, together with the numerical propagation and the original analytical solution as a reference. The same input parameters have been used as for Figure 5.13.

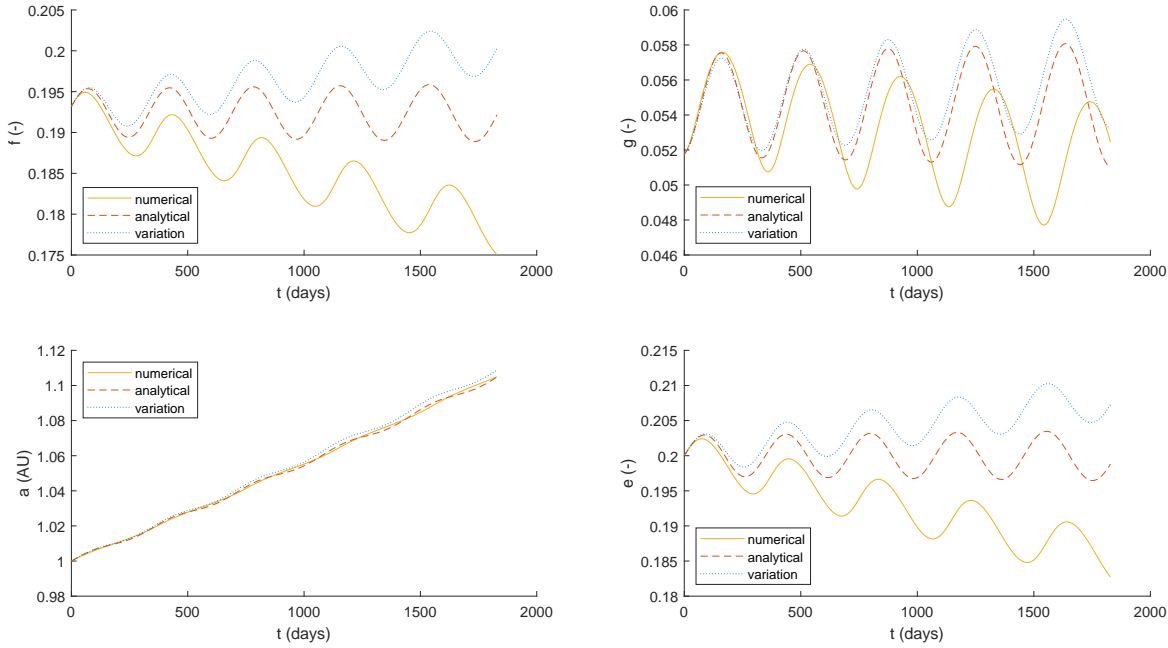


Figure 5.14: The behaviour of  $f$ ,  $g$ ,  $a$  and  $e$  resulting from the numerical propagation, the original analytical solution and the variation on the analytical solution with  $f_{tot} = 10^{-5} \text{ m/s}^2$ .

From the figures above it becomes immediately clear that the variation on the analytical solution shows not improvement over the original one. Moreover, the solution seems to deviate in the opposite direction. This is also confirmed by the absolute and relative differences shown in Table 5.5.

Table 5.5: The maximum differences between the numerical propagation and the two analytical solutions for  $f$ ,  $g$ ,  $a$  and  $e$ , both absolute and in percentages.

element	absolute differences		relative differences in %	
	original	variation	original	variation
$\Delta f$	1.71E-02	2.53E-02	9.8	14.4
$\Delta g$	8.29E-03	9.73E-03	17.1	20.1
$\Delta a$	2.98E+08	7.22E+08	0.2	0.4
$\Delta e$	1.71E-02	2.45E-02	9.2	13.4

In conclusion, none of the variations that have been attempted resulted in better results than what have been shown in Section 5.3 in Tables 5.1 and 5.2. However, the analytical solutions that have been obtained in Sections 5.1 and 5.2 provide results that are sufficiently satisfactory to continue developing this method. Looking back at the end of Chapter 4, the first three bullet points have been addressed in this chapter: a time-based analytical solution has been derived in Section 5.1, and the variations in the derivations for  $h$ ,  $k$ ,  $f$  and  $g$  have been addressed in this section. The final bullet point states that the increase in eccentricity can be stopped if coast arcs are introduced. The thrust will then restart at a different place in the orbit, causing the eccentricity to decrease. In this way, the eccentricity will be confined within bounds. This will be discussed further in the next chapter, where coast arcs are introduced in order to satisfy the bang-bang control constraint.



# 6

## Algorithm Development

In the previous chapters, an analytical solution for Gauss' form of Lagrange's planetary equations expressed in modified equinoctial elements was derived. However, apart from the absence of radial thrust, which was readily implemented in the analytical solution, another constraint on the acceleration set in Chapter 3 was that only bang-bang control would be allowed. Thus, besides thrust arcs, coasts arcs need to be introduced as well. Section 6.1 will explain in detail the steps taken to implement the bang-bang control into the algorithm. Thereafter, Section 6.2 will present and discuss the results. The algorithm will be analyzed in more detail in Chapter 7.

### 6.1. Bang-Bang Control

Bang-bang control implies that only two states of thrust exists; either the engine is on, and an acceleration is acting upon the spacecraft, or the engine is off, and the spacecraft will follow its Kepler orbit. In Chapter 5, an analytical solution has been found for the motion of the spacecraft during a thrust arc. Since the motion of the spacecraft during a coast arc is trivial (i.e. the elements remain constant, only the fast variable  $L$  needs to be propagated), the problem remains of determining the points at which the engines are switched on and off. If these switching points are chosen wisely, an efficient transfer orbit will result from the optimization process. As already mentioned in Chapter 4, the switching points can be chosen in such a way that the eccentricity stops to increase infinitely, but rather constrains itself to values close to zero. Keeping this in mind, a logical implementation would be to place the thrust arcs at 180 degrees from each other, such that the eccentricity increases at one end, but decreases at the other. Furthermore, from the figures shown in Chapters 4 and 5 (for example Figure 5.2), it can be seen that the inclination does not show a linear increase in time, rather, it oscillates around its initial value. Better insight is obtained when observing Gauss' form of the planetary equations expressed in Kepler elements, as shown in Chapter 3. The differential equation for the inclination is repeated here for convenience:

$$\frac{di}{dt} = f_w \frac{r}{\sqrt{\mu p}} \cos(u) \quad (6.1)$$

According to the above equation, the maximum change in inclination occurs when  $\cos(u) = 1$ , i.e. when  $u = 0$  or  $u = 180$  degrees. Furthermore, the direction of the thrust force should switch 180 degrees every time the spacecraft passes the nodes in order for the inclination to increase. Thus, when an inclination change is desired, the location of the thrust arcs can be set at these angles. One has to keep in mind that a variation in the longitude of the ascending node occurs in the exact opposite manner, with its largest changes occurring at  $u = 90$  degrees and  $u = 270$  degrees:

$$\frac{d\Omega}{dt} = f_w \frac{r}{\sqrt{\mu p} \sin(i)} \sin(u) \quad (6.2)$$

Taking the above discussion into consideration, an orbit can be divided into four arcs: two thrust arcs and two coast arcs alternating each other. This results in four switching points in total. The orbit is now defined by the following parameters:

- the lengths of the thrust and coast arcs
- the direction of the thrust force
- the timing of the switching points

For the implementation of the code, a few assumptions have been made on the above-mentioned points. First of all, the lengths of the two thrust arcs are the same, set as a design variable that is expressed as an angle (the thrust arc angle or  $taa$ ). As such, the length of the thrust arc can be used as a design parameter to optimize the transfer orbit. The coast arcs also have the same length, which follows directly from the length of the thrust arcs.

The direction of the thrust is determined by the steering angle  $\alpha$ , of which the definition was given in Chapter 3. In addition, the choice can be made whether the thruster points in the same direction during the entire orbit or it 'flips' its direction during the second thrust arc, thrusting in the opposite direction. This complies to the requirement that has been discussed above regarding a successful inclination change.

Finally, the timing of the switching points is determined by the argument of latitude  $u$ . The argument of latitude at which the first thrust arc is introduced is a design variable ( $u_1$ ); the second angle ( $u_2$ ) is automatically set 180 degrees further.

$$u_2 = u_1 + 180^\circ \quad (6.3)$$

The angles at which the switching points ( $swp$ 's) occur, are then determined as follows:

$$u_{swp1} = u_1 - taa/2 \quad (6.4)$$

$$u_{swp2} = u_1 + taa/2 \quad (6.5)$$

$$u_{swp3} = u_2 - taa/2 \quad (6.6)$$

$$u_{swp4} = u_2 + taa/2 \quad (6.7)$$

The switching points dividing an individual orbit into the thrust and coast arcs are visualized in Figure 6.1. Switch points 1 and 2 and 3 and 4 always enclose a thrust arc, while a coast arc lies between switch points 2 and 3 and 4 and 1.

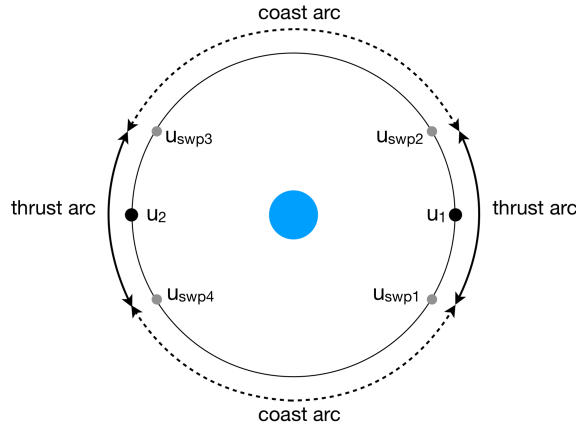


Figure 6.1: Sketch of the switching points for an individual orbit.

However, since the argument of latitude is not one of the modified equinoctial elements, a relation has to be found between  $u$  and one of the computed elements. Looking at its definition, the argument of latitude can be expressed in Kepler elements as follows [19];

$$u = \omega + \theta \quad (6.8)$$

The definition of the true longitude in terms of Kepler elements has already been shown in Chapter 3 and is repeated here for convenience:

$$L = \Omega + \omega + \theta \quad (6.9)$$

Thus, the following relation between the true longitude and argument of latitude can be found:

$$L_{swp} = \Omega + u_{swp} \quad (6.10)$$

The above expression is convenient, because the true longitude is available as a function of time. If  $\Omega$  is known, the switching time can be found with Equation 5.9 by solving for  $t$ . During a coast arc,  $\Omega$  is constant and can be computed with Equation 3.5e. During a thrust arc however,  $\Omega$  is subject to change: determining  $L_{swp}$  requires an iterative process. Keeping in mind that this algorithm will ultimately be used for optimization purposes, keeping the number of computations as low as possible is of great importance. Therefore,  $\Omega$  at the start of the thrust arc is used to compute the next switch time. The inaccuracies introduced by this assumption vary as  $u_1$  and  $u_2$  vary, since the change in  $\Omega$  is dictated by  $u$  (see Equation 6.2).

Finding the switching time with Equation 5.9 is not straightforward due to the sign-term, that in itself is dependent on time. However, when looking more carefully at Equation 5.13, a resemblance with the denominator in Equation 5.4 can be seen. As already mentioned, the denominator introduces a singularity in the solution when reaching zero, indicating a highly eccentric hyperbolic orbit (approaching a straight line). In Equation 5.13, the sign would switch at this point. Having declared this outside the scope of the developed method, the sign can be determined once at the start of the thrust arc, and remains unchanged for the rest of the thrusting period. Moreover, when substituting Equation 5.5 into Equation 5.13 and evaluating it at the initial time, the following observation is made:

$$S = \text{sign}\left(f_N t_0 - \sqrt{\frac{\mu}{p_0}} - f_N t_0\right) = \text{sign}\left(-\sqrt{\frac{\mu}{p_0}}\right) \quad (6.11)$$

Seeing that  $\mu > 0$  and  $p_0 > 0$ ,  $S = -1$  for all initial conditions. The switching time is then given by Equation 6.12.

$$t_{swp2,4} = -\frac{((C_L - L_{swp2,4})^4 f_N \mu)^{1/4} - C_p}{f_N} \quad (6.12)$$

If  $f_N = 0$ , Equation 5.21 describes the true longitude, rendering the switching time to be:

$$t_{swp2,4,perp} = (L_{swp2,4} - C_L) \frac{p\sqrt{p}}{\sqrt{\mu}} \quad (6.13)$$

For a coast arc, all the elements apart from the true longitude stay constant. Therefore, the same solution as for the perpendicular-thrust case is true for the true longitude, so that the times of the other two switching points can be expressed as:

$$t_{swp1,3} = (L_{swp1,3} - C_L) \frac{p\sqrt{p}}{\sqrt{\mu}} \quad (6.14)$$

In Chapter 5 it was stated that the integration constants  $C_p$ ,  $C_f$ ,  $C_g$ ,  $C_h$ ,  $C_k$  and  $C_L$  could be found using the initial state at the start of the transfer. However, by introducing coast arcs, the initial state is changed at the start of every thrust arc. Therefore, the integration constants are determined each time at the start of an individual thrust arc. For the coast arc, only  $C_L$  needs to be calculated, since the rest of the elements remains constant.

An extra stop criterion can be added to the algorithm, to facilitate targeting a final orbit. Instead of propagating until the final time has been reached, the simulation can be stopped when an orbital element has achieved a particular target value. After each thrust arc, the relevant element is checked. If its value has surpassed the target value, a secant root finder is used to find the exact time at which this has happened. This is then the total time of flight (TOF). Another parameter of interest is  $\Delta V$ , which is a measure of the required propellant. Because constant thrust is applied, the total  $\Delta V$  can be computed fairly simple with Equation 6.15, in which  $\Delta t_i$  is the time period of a thrust arc and  $n$  is the total number of thrust arcs of the transfer.

$$\Delta V = \sum_{i=0}^n f_{tot} \Delta t_i \quad (6.15)$$

## 6.2. Results and Discussion

The results of the algorithm described in the previous section are presented in Figure 6.2. The input parameters from Table 4.2 have been used, with a thrust acceleration of  $10^{-4}$  m/s<sup>2</sup>. Furthermore, the thrust arc angle has been set to 40 degrees,  $u_1$  is set to zero degrees and the thrust switches to the opposite direction at the start of each thrust arc. Comparing Figure 6.2 to Figure 5.4, it is noticed that the analytical solution lies closer to the numerical propagation once the bang-bang control has been implemented. The eccentricity does not increase exponentially, instead it stays rather close to zero. This allows the analytical solution to perform better, since it has been derived for zero eccentricity. Also, the inclination now shows a step-wise increase, because each thrust arc the thrust direction is flipped. At first glance, the solution for  $\Omega$  seems to diverge. However, when looking at the scale, the difference is relatively small. This is in agreement with Equation 6.2, which indicates that no change in  $\Omega$  occurs if the thrust is applied at  $u = 0$  or 180 degrees, as is the case here. Therefore, even if the two solutions are slightly different, the overall difference is not large. For  $\omega$ , at the start the results show rather erratic behaviour. Since the eccentricity at this moment is very low, the argument of periapsis is ill-defined. Later on, it shows a steady increase, and the numerical and analytical solution seem to lie close to each other.

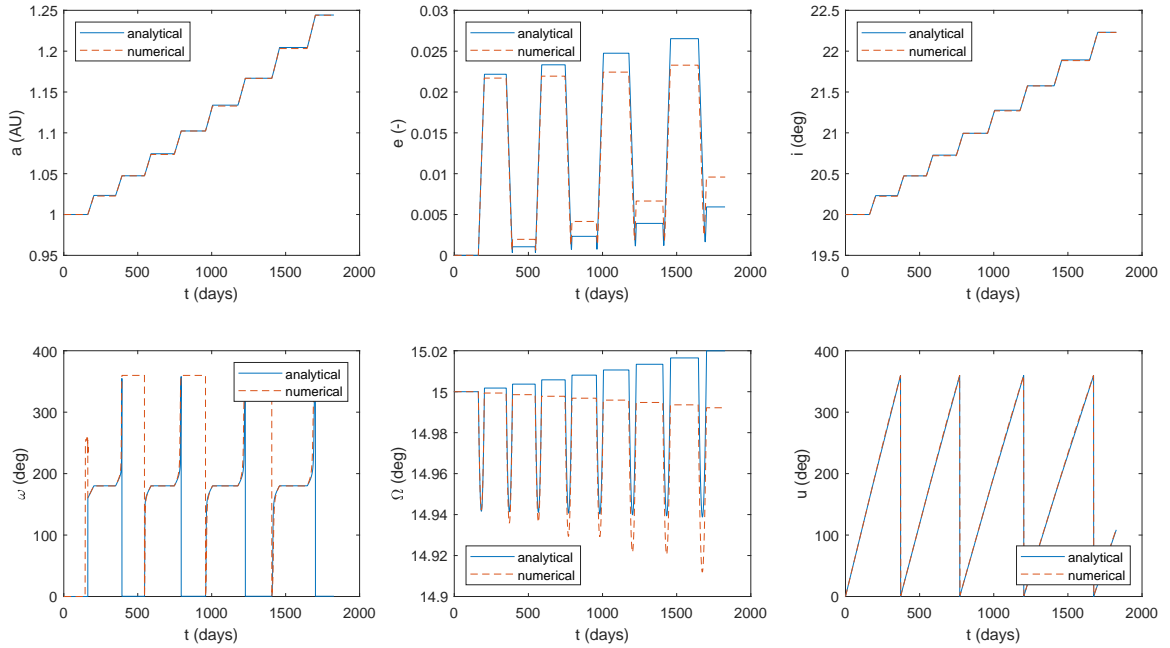


Figure 6.2: The Kepler elements for a thrust acceleration of  $10^{-4}$  m/s<sup>2</sup> for 5 years, with  $t_{aa} = 40$  deg and  $u_1 = 0$ .

In Table 6.1, the maximum error for each element is listed, together with the percentage difference. Furthermore, the analytical and numerical values at this point are also tabulated. The difference in  $\omega$  has only been computed when  $e > 0.001$ . This is to avoid the ill-defined argument of periapsis when the eccentricity is close to zero.

As expected, the difference in  $\Omega$  is relatively small, as well as the difference in  $a$  and  $i$ . However, the relative difference for the eccentricity is 43.9%. As explained in Section 5.3, this is because the eccentricity is used as a divider in Equation 4.34. Since the eccentricity is small, the percentage error is high. Therefore, the absolute error should be taken as the better measure of accuracy.

Further inspection of Table 6.1 reveals a relative difference of 27.8% for  $\omega$ . This does not seem to strike with Figure 6.2, where no large difference between the two solutions are observed. However, an explanation for this can be found by examining the last element  $u$ . Although the difference between the analytical and numerical result is not very large, differing at most by only 1.3 degrees, this does have a great impact on the remaining elements. This is because the switching times are based on  $u$ , thus a difference in this element causes a longer or shorter thrusting time. In Figure 6.2, this is most clearly seen in the plot for the eccentricity, where the analytical result constantly overshoots compared to the numerical result. The change in  $\omega$  is apparently so abrupt, that the small shift in  $u$  causes a large error. Thus, the analytical result for  $\omega$  is relatively inaccurate.

Table 6.1: The maximum differences between numerical and analytical solution for the Kepler elements for  $f_{tot} = 10^{-4} \text{ m/s}^2$ , TOF = 5 years,  $taa = 40 \text{ deg}$  and  $u_1 = 0$ .

element	analytical	numerical	abs. diff.	rel. diff. (%)
a (m)	1.80E+11	1.80E+11	1.93E+08	0.11
e (-)	5.30E-03	9.45E-03	4.15E-03	43.9
i (deg)	21.9	21.9	8.48E-03	0.039
$\omega$ (deg)	232.9	322.5	89.5	27.8
$\Omega$ (deg)	15.0	15.0	3.18E-02	0.21
u (deg)	108.5	109.8	1.30	1.2

To test the stop criterion for the target element, a transfer to  $a = 1.5 \text{ AU}$  (Mars' semi-major axis) is simulated. The results are shown in Figure 6.3. It can be seen that both the numerical and analytical solution reach 1.5 AU.

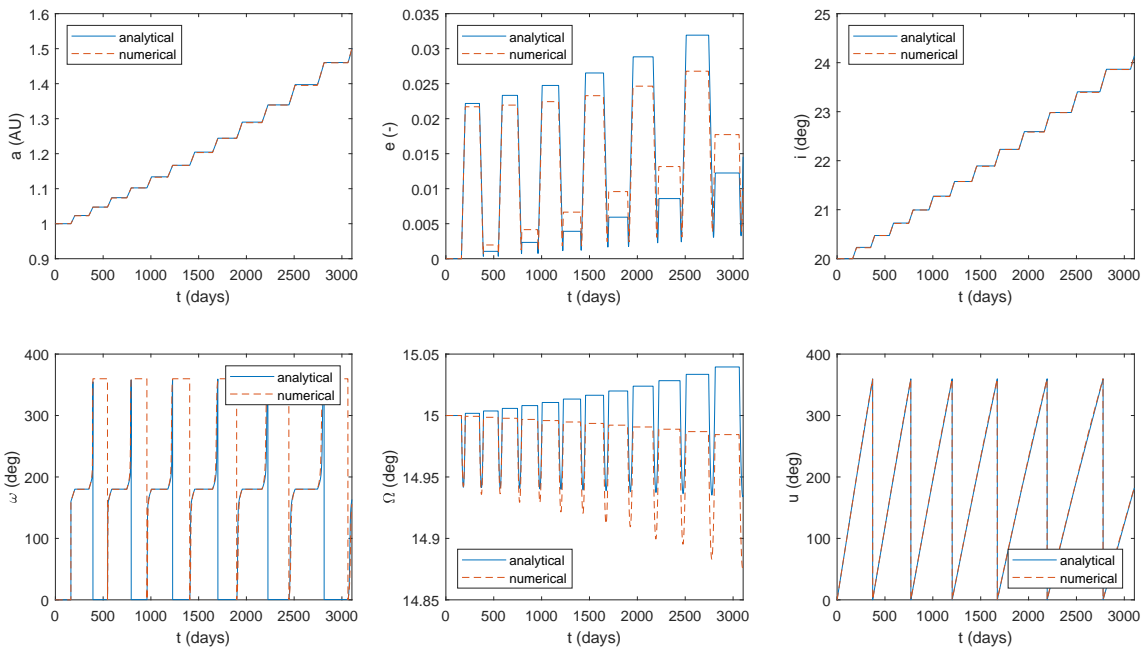


Figure 6.3: The Kepler elements for transfer orbit to  $a = 1.5 \text{ AU}$ , with  $f_{tot} = 10^{-4} \text{ m/s}^2$ ,  $taa = 40 \text{ deg}$  and  $u_1 = 0$ .

The differences are depicted in Table 6.2. These are computed differently than has been done so far. For an optimal transfer orbit, the most important task is to arrive at the right target orbit. Thus, the differences at the final TOF are computed. As expected and satisfying the stop criterion, the final semi-major axis of the numerical and analytical solution lie close together. Again, the percentage difference for the eccentricity is not a good representation of the error, but the absolute difference shows that the two results are in good agreement.

Table 6.2: The differences of the final state between numerical and analytical solution for the Kepler elements for a transfer orbit to  $a = 1.5$  AU, with  $f_{tot} = 10^{-4}$  m/s<sup>2</sup>,  $taa = 40$  deg and  $u_1 = 0$ .

element	abs. diff.	rel. diff. (%)
$\Delta a$	700.2	3.12E-07
$\Delta e$	4.49E-03	44.6
$\Delta i$	3.53E-03	0.01
$\Delta \omega$	7.51	4.8
$\Delta \Omega$	5.74E-02	0.39
$\Delta u$	0.44	0.24

# 7

## Performance Assessment

In the previous chapters, a method has been developed for simulating low-thrust transfer orbits without gravity losses and with bang-bang control. This chapter will elaborate on a more general assessment of the qualities of this method. As demonstrated in previous analyses, the method's inaccuracy increases as the transfer time increases. Thus, to visualize this increase in error, four time periods have been considered. The results will be discussed in Section 7.1. Hereafter, the method using a stop criterion has been assessed. This is discussed for various cases in Section 7.2.

During the assessment of the method, two limitations of the method have been established. Firstly, from the results found in Chapter 5 it can be seen that the results become less accurate as the eccentricity increases. This is a logical consequence of the assumption that has been made in Chapter 3, where the eccentricity was assumed to be zero. Therefore, in order to obtain relatively accurate results, an upper limit of  $e = 0.2$  has been set. Furthermore, as explained in Chapter 4, the modified equinoctial elements have a singularity at  $i = 180$  degrees. Thus, the analytical solution will not be able to provide good results. To prevent this, a limit has been set to  $i = 175$  degrees, and the algorithm will identify all results with a higher inclination as infeasible.

### 7.1. Fixed Time Periods

Four time periods are considered, namely 2.5, 5, 7.5 and 10 years. Two input parameters have been varied: the thrust arc angle within the range from 5 to 175 degrees (so the length of the coast arc is between 175 and 5 degrees), and the steering angle from 0 to 90 degrees. No thrust arc of 180 degrees is considered, since this would imply continuous thrusting, which does not comply with the bang-bang control constraint. Furthermore, the steering angle flips its direction at the start of each thrust arc. Finally, this has been repeated for three thrust acceleration values,  $f_{tot} = 10^{-5}$ ,  $10^{-4}$  and  $10^{-3}$  m/s<sup>2</sup>. As usual, the maximum errors are obtained by taking the difference between the analytical and the numerical trajectories.

The results for  $f_{tot} = 10^{-5}$  m/s<sup>2</sup> are shown in Figure 7.1. Overall, the errors are relatively small for this thrust value. For the semi-major axis, the largest errors occur at a small steering angle and high thrust arc angle. This is logical, since the largest change in  $a$  occurs when the thrust vector lies completely in-plane, and when the thrust acceleration is applied for a longer period of time. The largest errors for the eccentricity occur, just as for the semi-major axis, in the lower right corner. Again, the change in eccentricity is here the largest, resulting in the largest deviations with respect to the numerical propagation.

For the inclination, the area with the largest errors seems to have shifted upwards for a time of flight of 2.5 years. Here, the influence of the assumption on the eccentricity becomes visible; the more the eccentricity increases (and thus is less close to zero), the larger the errors of the solution. Since the eccentricity changes the most for the largest thrust arc angles, the largest errors are present at the right side of the error plot. However, the inclination hardly increases at small steering angles, because an out-of-plane acceleration component is required to do so. Thus, the largest errors occur at the center, where the steering angle has a considerable influence on both the eccentricity and the

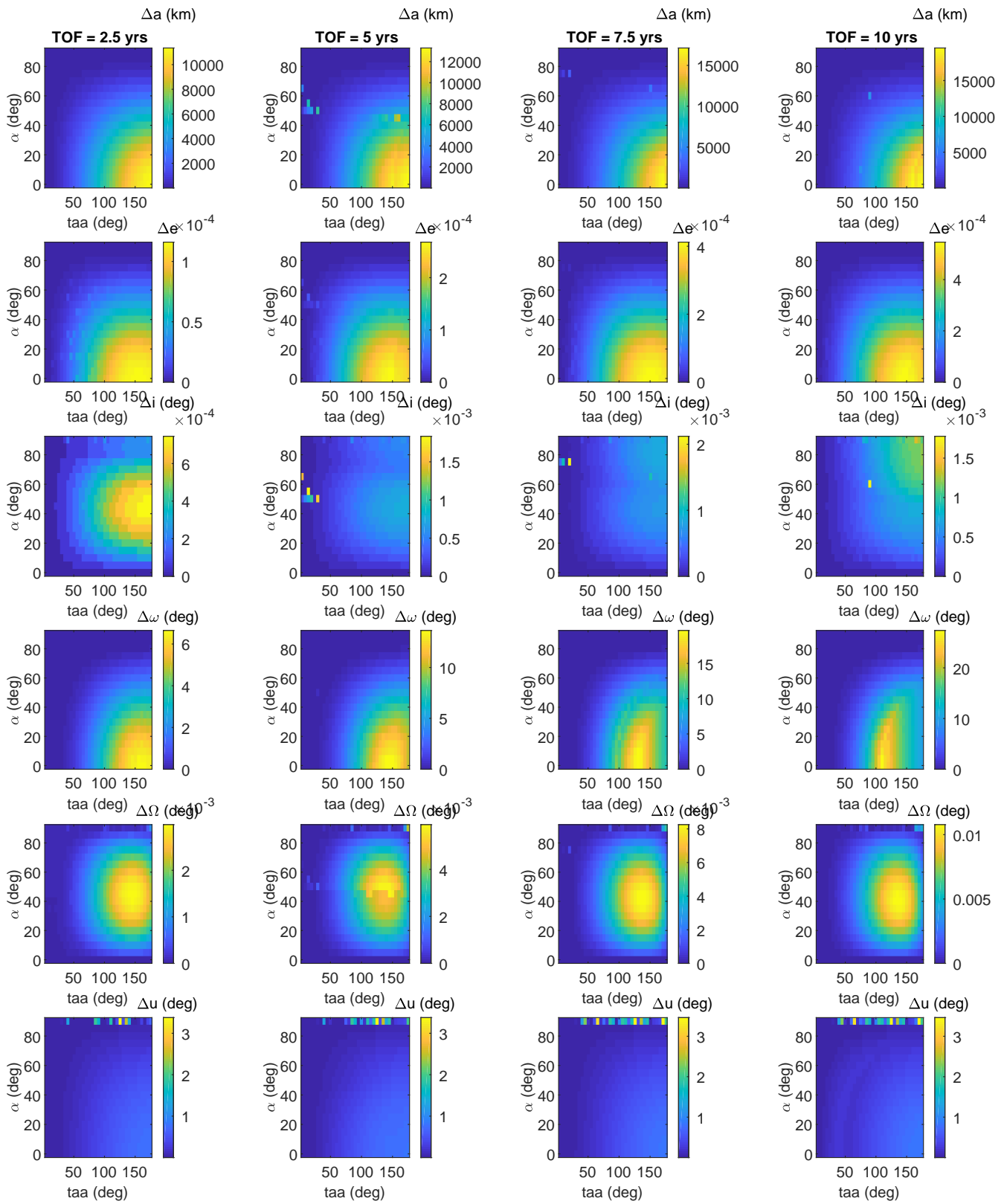


Figure 7.1: Maximum errors in elements for TOF = 2.5, 5, 7.5, 10 years ( $f_{tot} = 10^{-5}$  m/s<sup>2</sup>,  $u_1 = 0$  deg).

inclination. As the time of flight becomes larger, the maximum errors shift upwards, to the upper right corner. Apparently, here the increase in inclination becomes the more important error source, as the error builds up with every thrust arc. Nevertheless, the errors are still very small (in the order of  $10^{-3}$  degrees) and indeed negligible when compared relatively (0.6% in the maximum case).

The errors in argument of periapsis show similar behaviour to the eccentricity, which is as expected. However, as the time of flight increases, the area with the largest errors slightly shifts to the left. Also, the maximum error increases rapidly with increasing time of flight. These results can indicate that the argument of periapsis may not be very well estimated by the developed method. Before making a conclusion, the results for the thrust accelerations of  $10^{-4}$  m/s<sup>2</sup> and  $10^{-3}$  m/s<sup>2</sup> will be analyzed first.

For the longitude of the ascending node, the errors behave similarly to the errors of the inclination, which is as expected, since the change in this element is also caused by an out-of-plane component of the thrust acceleration (see also Equation 6.2). Note that the area with the largest errors stays at the center of the right side; unlike the inclination, the change in  $\Omega$  is the smallest at the chosen values of argument of latitude ( $u_1 = 0$  degrees and  $u_2 = 180$  degrees).

Finally, the argument of latitude shows relatively small errors for all time of flights. A few outliers are noticed at the top of the error plot, where the steering angle is 90 degrees. These could have been introduced by the numerical propagation. While a separate analytical solution has been derived for the case  $f_N = 0$ , forcing the elements  $a$  and  $e$  to remain constant over time, the numerical propagation deals with truncation inaccuracies, allowing (very small) variation over time. However, since the argument of latitude is computed using  $\omega$  and  $\theta$  (see Equation 6.8), and since these two elements are ill-defined for low eccentricities, erroneous results for the numerical propagation occur. Nevertheless, the largest error is around 3.5 degrees, which is deemed acceptable.

From Figure 7.2 it can be clearly seen that at a higher thrust value, the errors increase. This was expected, because larger orbit changes are achieved at larger thrust values. It is also noticed that at high thrust arc angles and steering angles, the solutions become infeasible, that is, the eccentricity increases to a value above 0.2. The algorithm discards these results, because the transfer orbit starts to deviate too much from the assumption made during the development of the analytical model (the eccentricity is equal to zero). These infeasible solutions are marked with white in the error plots. As the time of flight increases, the area of infeasible solutions becomes larger. As could be expected from Figure 7.1, the infeasible solutions occur at the lower right corner of the error plot, where the thrust arc angle is large and the steering angle is small. As already explained, the change in eccentricity is here the largest, as a large in-plane acceleration acts on the satellite. The errors in the semi-major axis might seem large, varying up to the order  $10^7$  km, but viewed from the perspective of the problem, namely a heliocentric orbit, the errors are relatively small (on average 0.65% for TOF = 10 years).

The errors in eccentricity can also be considered small. As the time of flight increases, a few combinations at the border of the infeasible white area show a high error compared to the rest of the results. This is where the eccentricity has come close to the limiting value of 0.2, but has not quite reached it. Still, the average error for TOF = 10 years is 0.008, yielding the results satisfactory. The results for the inclination are also satisfactory. Again, peaks in error are observed at the boundary of the infeasible area. For the inclination, these peaks are located at the upper side, rather than at the lower side for the eccentricity. This is because a higher steering angle has a higher impact on the inclination, while the eccentricity is influenced the most by a lower steering angle. Nevertheless, the average error is 0.17 degrees for the highest time of flight (10 years), which can be considered negligible.

The errors in argument of periapsis do not show a very clear pattern. They are small for small thrust arc angles or high steering angles, but show a sudden (very large) increase for thrust arc angles between approximately 20 and 45 degrees. These large errors could be explained by the phenomenon that has been explained in Section 6.2, where it has been said that  $\omega$  changes very abruptly when the rocket engine is turned on. Then, if the numerical and analytical results for  $u$  do not coincide exactly, the thrust arcs will start at different times, causing large errors in  $\omega$ . However, the errors in  $\omega$  decrease as the thrust arc angle increases, while one would expect that a larger thrusting time results in a larger error. Even so, the large errors, which are over 100 degrees, yield the analytical results for  $\omega$  as inaccurate and they are not recommended to be used as an indication for preliminary mission design. An exception could be made for small thrust arc angles (smaller than 20 degrees) or high steering angles (higher than 85 degrees). The errors in  $\Omega$  show similar behaviour to the inclination.

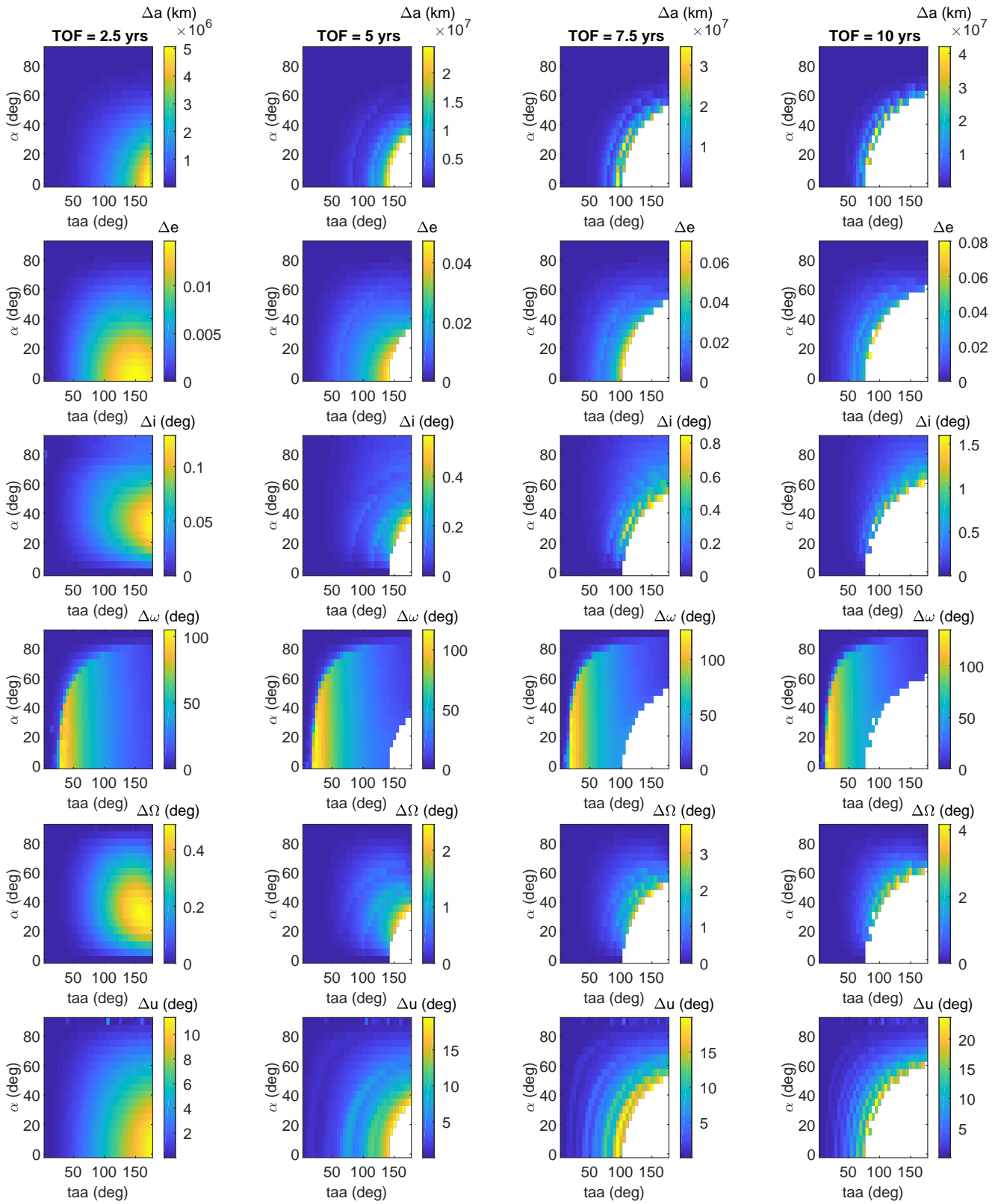


Figure 7.2: Maximum errors in elements for TOF = 2.5, 5, 7.5, 10 years ( $f_{tot} = 10^{-4}$  m/s<sup>2</sup>,  $u_1 = 0$  deg).

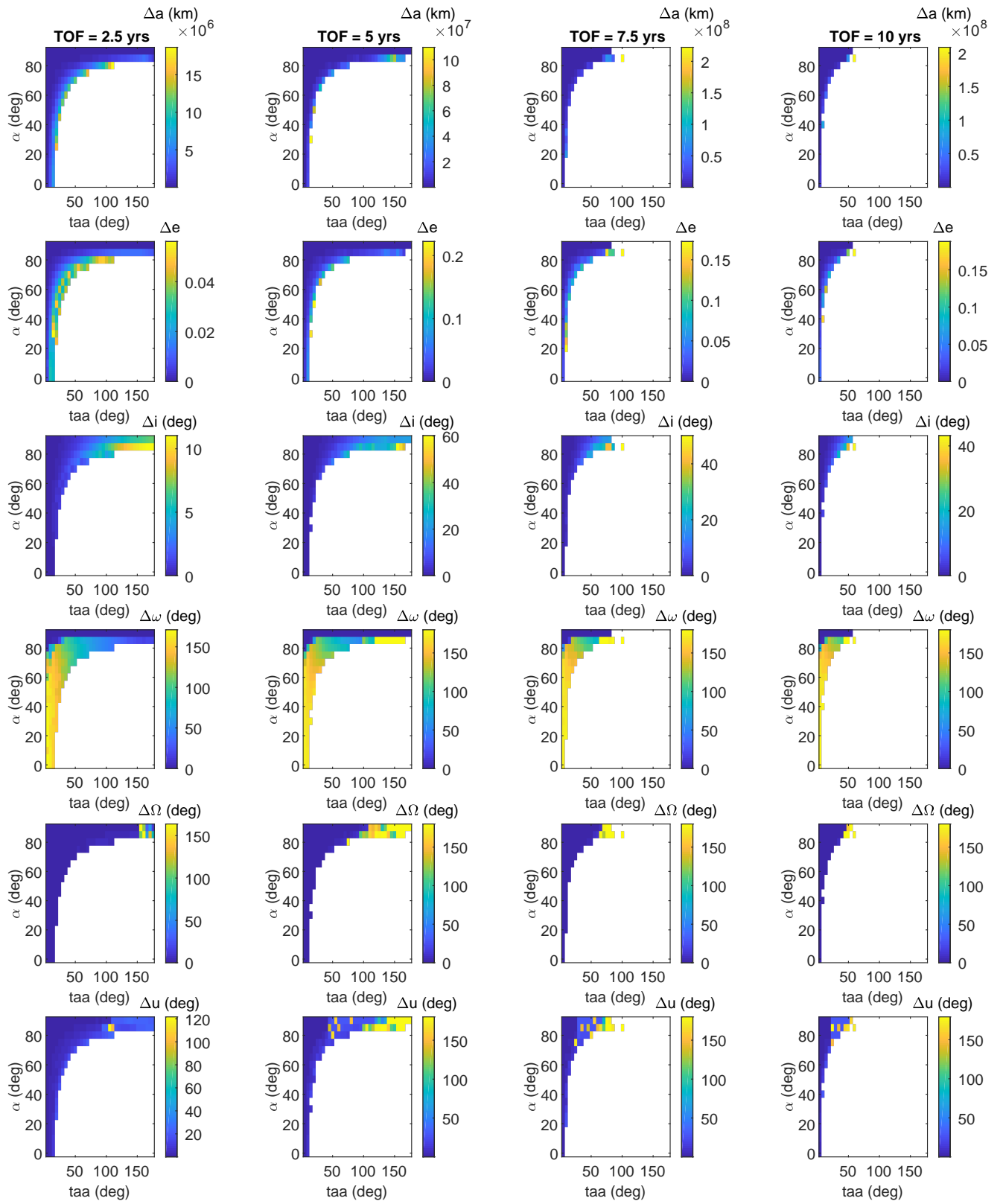


Figure 7.3: Maximum errors in elements for TOF = 2.5, 5, 7.5, 10 years ( $f_{tot} = 10^{-3}$  m/s<sup>2</sup>,  $u_1 = 0$  deg).

Again, peaks are noticed at the upper end of the infeasible area. The average error for TOF = 10 years is 0.045 degrees, making the overall results acceptable.

Looking at the results for  $u$ , a few relatively large errors are noticed, reaching over 20 degrees for a flight of time of 10 years. These large errors partly form the cause for the large errors perceived at the borders of the infeasible areas in the remaining elements. Because the analytical solution for the argument of latitude does not represent the numerical solution well, the thrust and coast arcs are started at different times, naturally inducing errors in the rest of the elements. On average though, the error in  $u$  is approximately 4 degrees (TOF = 10 years). This indicates that the analytical solution can be used well outside of this border area.

When the thrust acceleration is increased to  $10^{-3}$  m/s<sup>2</sup>, few combinations remain possible, as can be seen in Figure 7.3. The eccentricity increases rapidly and the orbit can become hyperbolic, as has already been established in Chapter 4. Feasible solutions occur at low  $t_{aa}$  or high  $\alpha$ . Again, these are the cases where the increase in eccentricity is relatively small, and the assumption on eccentricity is violated the least. As the time of flight increases, the results for a high  $\alpha$  become less and less feasible, such that the feasible solutions are mostly located in the upper left corner. For TOF = 2.5 years, the average relative error for the semi-major axis is 1.1%, while for TOF = 10 years this is 2.7%. The largest errors in eccentricity are high, some even reaching 0.2. The results of the analytical solution in these cases are clearly not acceptable, considering that the upper limit for the eccentricity was also set to 0.2. Looking at the average, the error for TOF = 5 years is around 0.02. Thus, on average the results are good, but some cases are not well filtered by the limits imposed on the analytical solution.

Similarly, the results for the inclination do not seem to perform well when looking at the maximum errors, especially at TOF = 5 years. However, when taking the average, the error is only around 8.8 degrees. In the discussion of the results for  $f_{tot} = 10^{-4}$  m/s<sup>2</sup>, it was concluded that the developed method does not yield good results for  $\omega$ . This is confirmed by the results in Figure 7.3, where some of the errors reach 180 degrees, thus meaning that the argument of periapsis is located at the opposite side of the orbit. Also some errors in  $\Omega$  and  $u$  are approaching 180 degrees, especially at higher thrust arc angles. For TOF = 2.5 years, the average error for  $\Omega$  is around 7.3 degrees and for  $u$  around 8.8 degrees. However, these averages quickly increase as the time of flight goes up. To obtain better averages, the results at the right side of the plots should be excluded from analysis (that is, the high thrust arc angles). Thus, for a thrust acceleration of  $10^{-3}$  m/s<sup>2</sup>, feasible results only occur at low thrust arc angles.

In conclusion, the developed method shows good results for the Kepler elements, apart from the results for  $\omega$ . However, some very high errors are noticed close to the infeasible area. In these cases, the eccentricity approaches the 0.2 limit, but does not reach it. This could mean that the limit for the eccentricity was not chosen correctly, and a lower limit should be imposed in order to eliminate the (few) peaks in errors.

## 7.2. Stop Criterion

To assess the influence of reaching a final destination, four cases have been analyzed. These cases are:

- Change in semi-major axis from 1 AU to 1.524 AU (Mars' semi-major axis).
- Change in semi-major axis from 1 AU to 5.2 AU (Jupiter's semi-major axis).
- Change in inclination from 20 degrees to 22 degrees.
- Change in inclination from 20 degrees to 40 degrees.

The maximum flight times have been set to 10 years, with the exception of 30 years for the mission to Jupiter. The remaining initial parameters are set as depicted in Table 4.2, and  $f_{tot} = 10^{-4}$  m/s<sup>2</sup>. A small and large inclination change have been chosen, to show the method's capability to model both. The results are shown in Figures 7.4 to 7.7. Rather than the maximum errors, here the differences between the final states from the numerical propagation and the analytical solution are compared. Furthermore, the required  $\Delta V$  and final TOF are computed as well. The results in the lower left corner

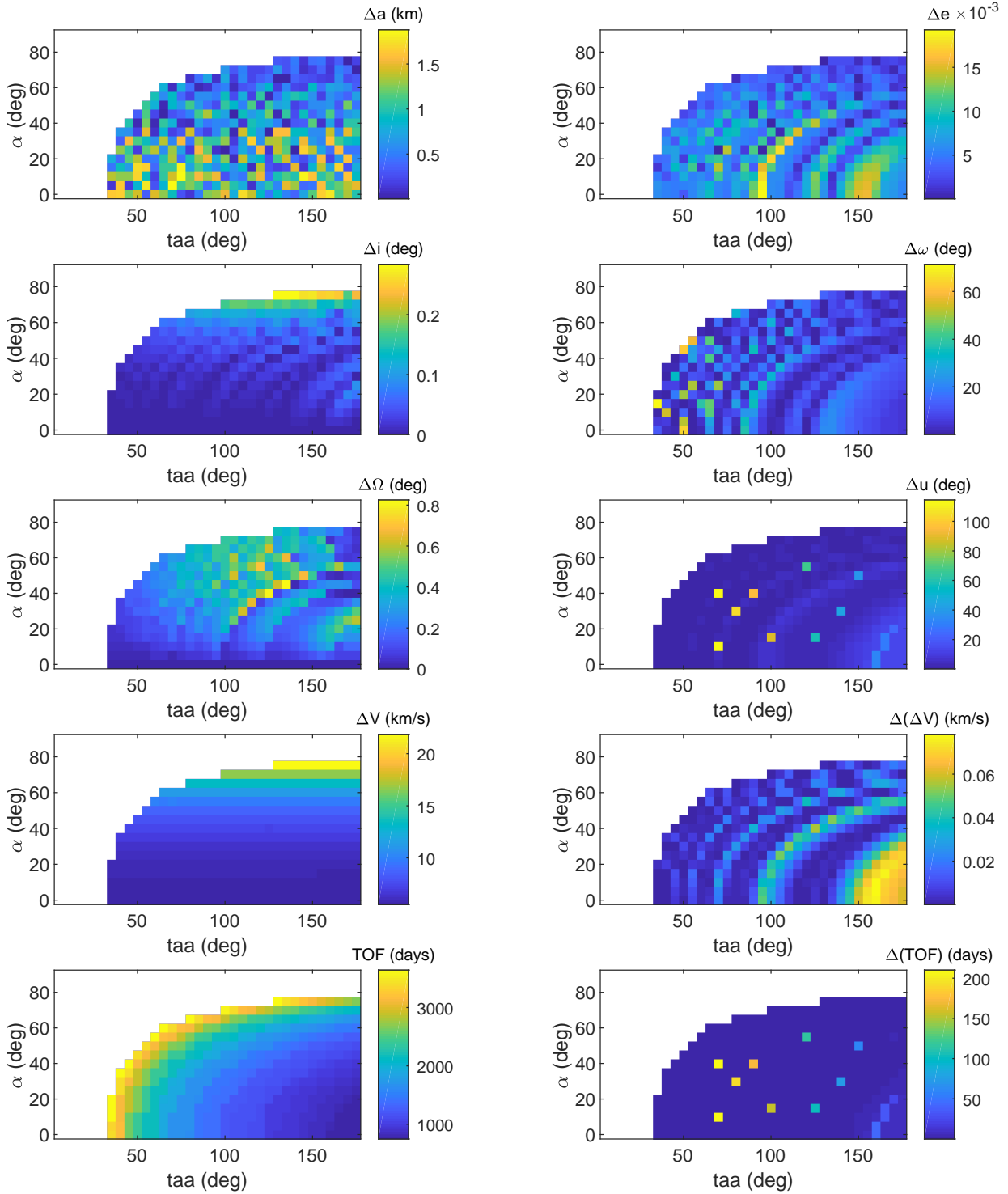


Figure 7.4: The errors between the final Kepler elements of the numerical and analytical solutions (upper six plots), the required  $\Delta V$  and TOF to achieve target orbit resulting from the analytical solution (lower left plots), and the errors between  $\Delta V$  and TOF of numerical and analytical solution (lower right plots) (stop criterion is  $a = 1.524$  AU,  $f_{tot} = 10^{-4}$  m/s<sup>2</sup> and maximum TOF = 10 years).

are given by the analytical solution. The lower right corner gives the difference with respect to the numerical propagation. The TOF is simply the time at which the propagation has been stopped due to the stop criterion. The  $\Delta V$  is computed by multiplying each thrust arc time period by the thrust acceleration, since the acceleration is constant. The  $\Delta V$ 's of each thrust arc are then added together (see Equation 6.15). The infeasible solutions include also the combinations where the target element has not been reached within the maximum TOF.

For the first case, Figure 7.4 shows that the results have a good accuracy. The difference in eccentricity and inclination are negligible, and also the average difference in  $\Omega$  is relatively small. For  $\omega$ , the difference does become significant for several combinations of input angles, and has a relatively high error in general. As already concluded before, the developed algorithm is not able to estimate  $\omega$  well. The difference in semi-major axis may be unexpected though, since the stop criterion has been set to a certain value of the semi-major axis. However, it is noticed that the numerical propagation and analytical solution use different methods to arrive at this final condition, therefore numerical errors are inevitable. While the analytical solution computes the final  $a$  in an exact way, the numerical propagation depends on the step size. Thus, a small overshoot can occur when the stop criterion is met. However, the final differences in  $a$  are also relatively small, when compared to the scale of the problem. This means that the erratic patterns of the  $\Delta a$  values can be ignored because of their insignificance.

The required  $\Delta V$  and TOF show expected behaviour. As the steering angle increases, the required  $\Delta V$  increases too. This is because the larger the out-of-plane component of the thrust acceleration, the smaller the change in semi-major axis. Thus, it also takes longer to arrive at the target orbit, which is reflected by the high TOFs for these input values. High TOFs are also noticed for small values of the thrust arc angle. Logically, if less thrust is applied during one revolution, the spacecraft will need a higher number of revolutions before arriving at the target orbit.

The differences of  $\Delta V$  show good accuracy as well, with the maximum error in  $\Delta V$  being just 1.4%. The differences in TOF however show some high peaks at specific combinations of thrust arc angle and steering angle. This is the result of the error in  $u$ , which causes the thrust and coast arcs to start and end at slightly different moments for the numerical and analytical results. Also, the elements of the numerical and analytical solution have already obtained an error at the end of the propagation. Therefore, it may happen that while the analytical solution has reached the target value just within the last thrust arc, the numerical propagation will introduce one extra coast arc before also arriving at the target value shortly after. The introduction of the coast arc therefore causes the TOF to differ significantly. When designing a mission, this difference can be neglected though, as the only adjustment would be to thrust for a slightly longer period during the last thrust arc.

For the second case (Figure 7.5), the combinations yielding feasible solutions are far more sparse. On the one hand, the restriction of 30 years for the TOF might have been too strict (10,000 days in the plot for TOF corresponds to 30 years, which is the upper limit). No feasible results are present when the thrust arc angle is small (i.e. the rocket engine is active for a shorter period of time), which indicates that not enough force is applied in order to change the orbit to the desired semi-major axis. On the other hand, the accuracy of the developed method decreases as the time increases, as concluded in Chapter 6. This is because the eccentricity becomes large, and therefore the assumption of zero eccentricity is no longer valid. Thus, large thrust arc angles yield infeasible results because the eccentricity crosses the upper limit. Finally, a higher steering angle results in less change of semi-major axis during one orbit, such that the target value cannot be achieved within the given TOF. For the combinations that are feasible, the results vary largely.

The largest relative error for the inclination is just over 3%, which is still acceptable. However, taking into account that the focus is on changing the semi-major axis, no large increase in the inclination is anticipated. Indeed, the results for the higher steering angles (where the inclination change is large) are mostly infeasible, because the required  $a$  cannot be reached. Similarly to previous results,  $\omega$  shows relatively large differences and is not considered to be a good approximation. The eccentricity reaches in some cases an error of 0.2, which is equal to the feasible range. This, of course, will yield inaccurate results. For the argument of latitude, some cases yield acceptable errors, but some also show very high deviations of the analytical solution. For an optimization process, this would be disadvantageous, since  $u$  is used to define the thrust profile (the start of the thrust and coast arcs). This also has a large impact on the required  $\Delta V$ , which is directly related to the thrust profile. Thus, the resulting preliminary

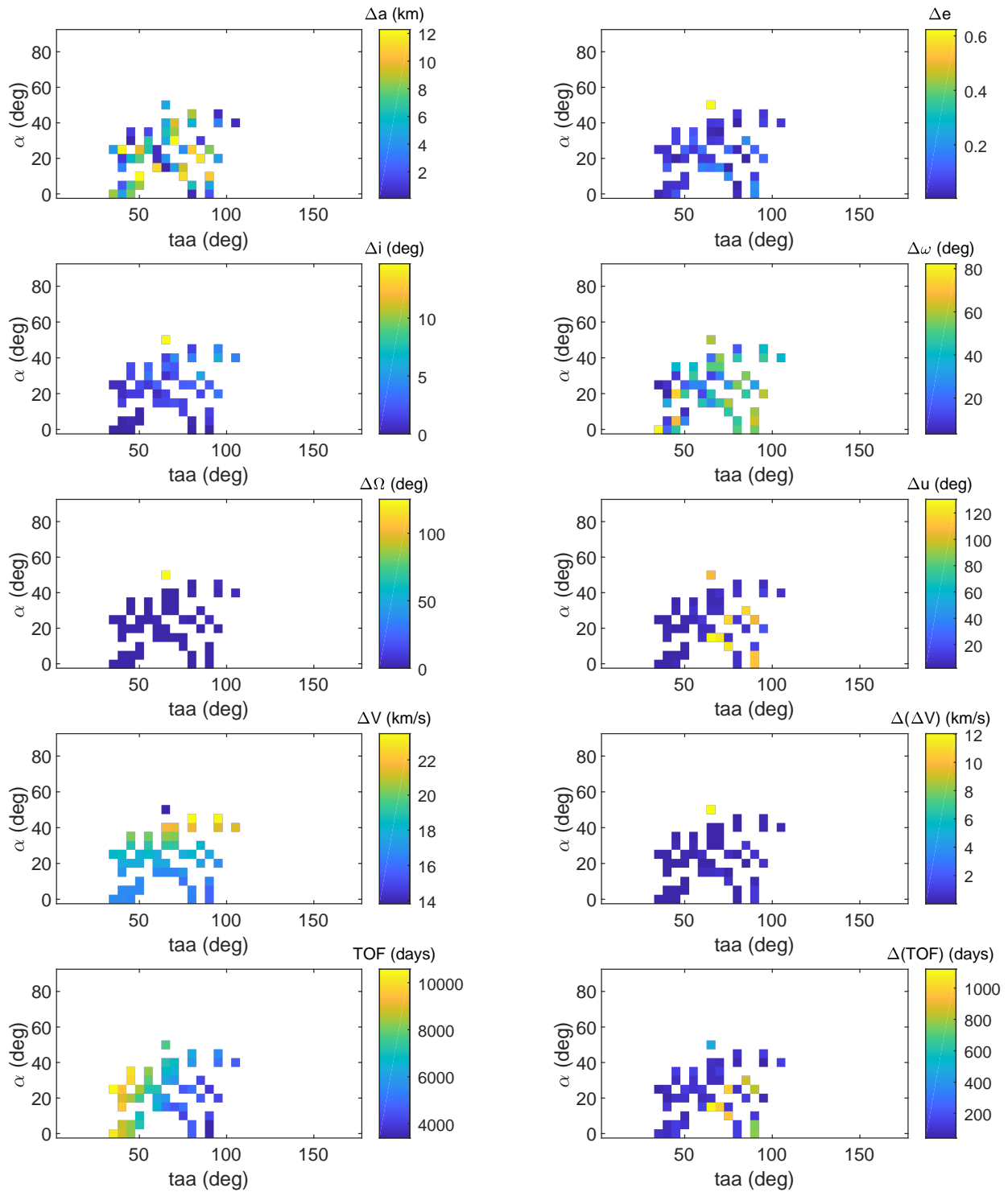


Figure 7.5: The errors between the final Kepler elements of the numerical and analytical solutions (upper six plots), the required  $\Delta V$  and TOF to achieve target orbit resulting from the analytical solution (lower left plots), and the errors between  $\Delta V$  and TOF of numerical and analytical solution (lower right plots) (stop criterion is  $a = 5.2$  AU,  $f_{tot} = 10^{-4}$  m/s<sup>2</sup> and maximum TOF = 30 years).

optimum mission may look very differently from the actual case, when the high-accuracy optimizers are used. In conclusion, while some combinations may yield good results with fair accuracies, the method does not occur to be reliable enough to design problems including large TOFs.

The results for the two-degrees inclination change are shown in Figure 7.6. It can be seen that the stop criterion for the inclination works better than for the semi-major axis, since the errors are in the order of  $10^{-4}$  degrees. It is also noticed that a large number of feasible solutions exist to arrive at the target orbit. Unfeasible solutions occur at low thrust arc angles, where the applied acceleration is not large enough to provide the required impulse, and at low steering angles, since an inclination change requires an out-of-plane thrust component. The overall accuracy of the elements is good. The relative average error for  $a$  is 0.06%. The eccentricity shows a maximum error of approximately 0.04, but the average error is 0.002. Also for  $\Omega$ , where a few distinct results achieve an error of around 0.5 degrees, the average error is far smaller, being around 0.07 degrees.

As could be expected from the results of the first case, the errors for  $u$  are relatively small, but show some very large values at specific combinations, caused by an extra coast arc inserted at the end of the transfer as explained for the first case. For the required  $\Delta V$  and TOF, the opposite behaviour is seen compared to Figure 7.4. Naturally, the largest inclination change occurs at the highest steering angle, unlike the change in semi-major axis. Therefore, the largest values for the required  $\Delta V$  and TOF appear at the lower part of the plot. Large TOFs are still noticed at low thrust arc angles, just as in the first case. The peaks in TOF for certain combinations are again attributed to the phenomenon as described for the first case, and coincide with the peaks found in the errors for  $u$ .

The final case is shown in Figure 7.7. The feasible solution space has visibly decreased compared to the previous inclination change. Since the input parameters are the same for both cases, it is reasonable that the higher inclination change will be achieved less often. Again, the results for  $\omega$  may be discarded, since these show large errors. The results for the inclination however are in good agreement, confirming that the algorithm works well when  $i$  is given as stop criterion. Apart from one result, with an error of around 0.22 degrees, the errors seem to be very small, with the average error being just 0.0012 degrees. The results for the semi-major axis also have good accuracies, with an average relative error of 0.14%. For  $\Omega$ , the average error is 1.26%.

Just as with the previous results,  $u$  shows small errors, except from some distinct cases, which are mimicked by the errors for the time of flight. The average error is nevertheless just 7.1 degrees, including the large errors. This shows that the remaining have a good accuracy. Also the required TOF shows a good accuracy, with an average errors of approximately 18 days. As explained above, the few large deviations for the TOF does not have to mean that the true optimum lies far from the preliminary optimum for these cases, since the last thrust arc can be slightly lengthened to a achieve the target element. Finally, the average error for  $\Delta V$  is 0.0564 km/s, which also indicates a good accuracy. For the total required  $\Delta V$ , the largest value occur at the largest thrust arc angles, which correspond to the longest thrusting times. The largest TOF is required at the smallest (feasible) thrust arc angle, as expected.

Since no optimization has been performed, it is difficult to make a comparison with the results from other methods as presented in Chapter 2. However, an indication can be provided using the algorithm with the stop criterion. In Section 2.3, a transfer from Earth to Mars has been optimized using bang bang control. An average thrust acceleration of  $1.6 \cdot 10^{-4}$  m/s<sup>2</sup> is applied on the spacecraft. This is used as the input acceleration for the developed algorithm. Furthermore, the initial Kepler elements are set to  $a = 1$  AU,  $e = 0.017$ ,  $i = 0$  degrees and  $\Omega = 0$  degrees, which are the Kepler elements of the Earth orbit around the Sun [38]. The element  $\omega$  has not been taken into account, since this element proved to be estimated inaccurately by the algorithm. Also, for the sake of simplicity, the time of transfer and the initial and final  $u$  have not been taken into account and it is assumed that Mars will be in position when the spacecraft reaches its orbit. Both  $\omega$  and  $u$  are therefore set to 0 degrees. The stop criterion is once again set to 1.524 AU, which is Mars's semi-major axis. Then, a similar grid search to the ones presented above is performed. The results are inspected not only on the lowest  $\Delta V$ , but also on the three remaining elements. Mars's orbit has the following Kepler elements:  $e = 0.093$ ,  $i = 1.85$  degrees and  $\Omega = 49.56$  degrees. When  $\alpha = 10$  degrees and  $taa = 120$  degrees, the differences between the final results of the algorithm and Mars's orbit are  $de = 0.0038$ ,  $di = 0.077$  degrees and  $d\Omega = 308.9$  degrees. The differences in  $e$  and  $i$  are acceptable, but the difference in  $\Omega$  seems high. However, this

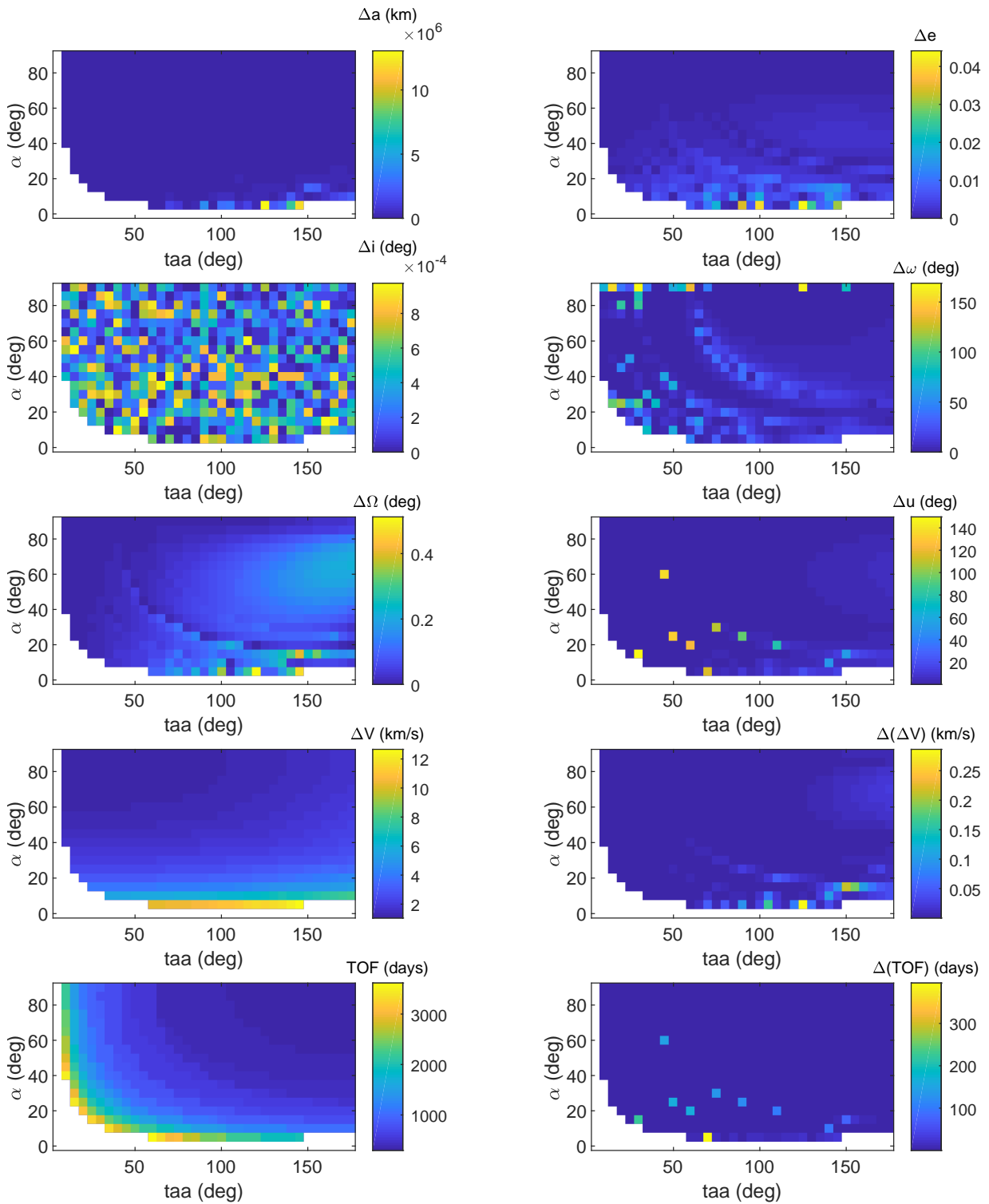


Figure 7.6: The errors between the final Kepler elements of the numerical and analytical solutions (upper six plots), the required  $\Delta V$  and TOF to achieve target orbit resulting from the analytical solution (lower left plots), and the errors between  $\Delta V$  and TOF of numerical and analytical solution (lower right plots) (stop criterion is  $i = 22$  degrees,  $f_{tot} = 10^{-4}$  m/s<sup>2</sup> and maximum TOF = 10 years).

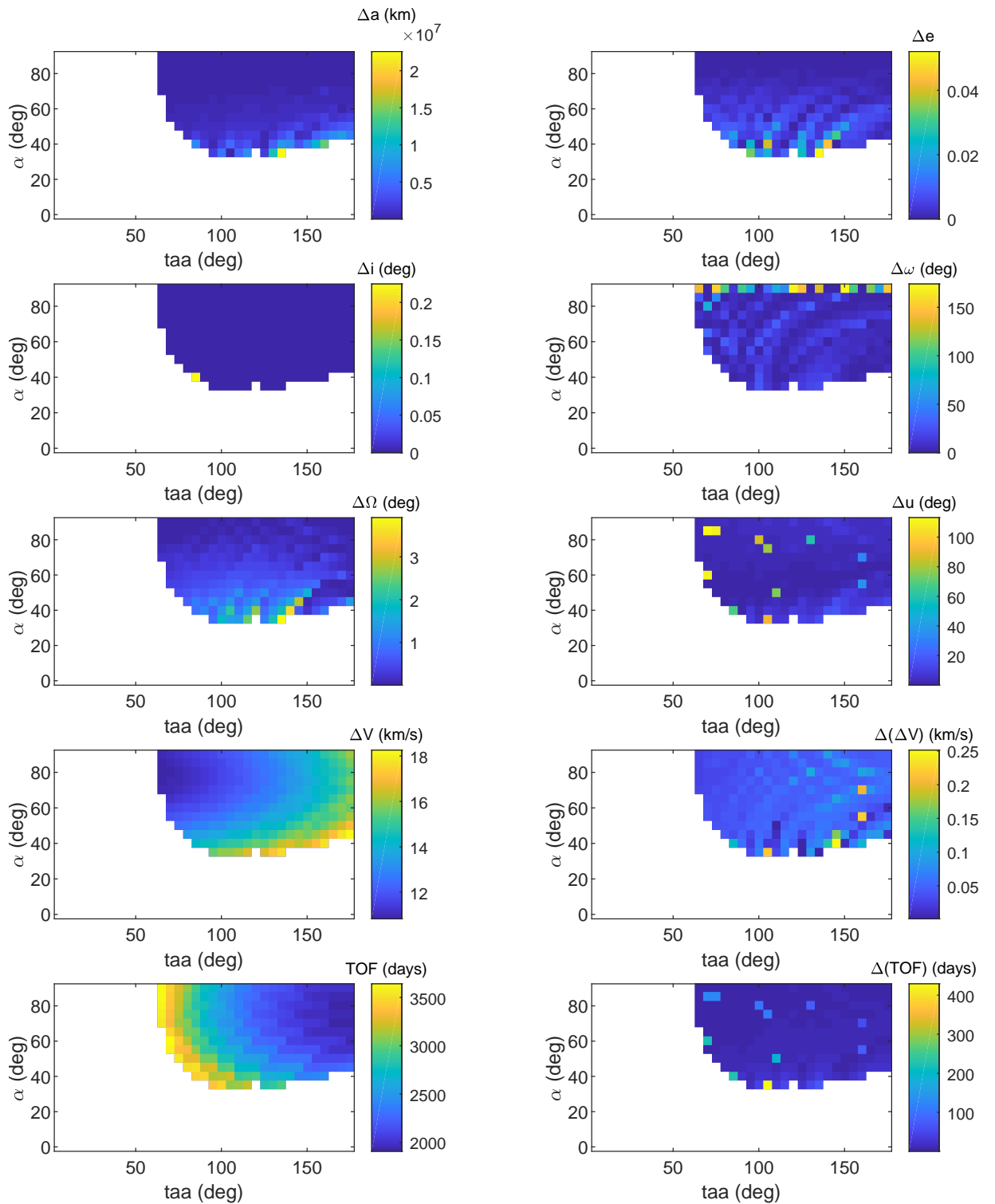


Figure 7.7: The errors between the final Kepler elements of the numerical and analytical solutions (upper six plots), the required  $\Delta V$  and TOF to achieve target orbit resulting from the analytical solution (lower left plots), and the errors between  $\Delta V$  and TOF of numerical and analytical solution (lower right plots) (stop criterion is  $i = 40$  degrees,  $f_{tot} = 10^{-4}$  m/s<sup>2</sup> and maximum TOF = 10 years).

difference could be expected, as the thrust is applied at the positions in orbit when the change in  $i$  is highest, but the change in  $\Omega$  lowest. Thus, the correct  $\Omega$  could be achieved by thrusting at  $u = 90$  and  $270$  degrees with  $\alpha = 90$  degrees. Nevertheless, this case serves as a good indication for the required  $\Delta V$ , which is equal to  $5.65$  km/s. This is similar to the result presented in Section 2.3, where the final  $\Delta V$  was  $5.68$  km/s. Also the TOF's are similar, being  $727$  days for the developed algorithm, compared to  $793$  days from Section 2.3.

In Section 2.1, a transfer from Earth to Mars was optimized using the Finite Fourier Series method with approximate on-off thrusting. From Figure 2.5 it can be seen that the approximate thrust acceleration is  $0.02$  DU/TU<sup>2</sup>, or  $1.2 \cdot 10^{-4}$  m/s<sup>2</sup>. The total  $\Delta V$  can be roughly estimated by assuming the rocket engine has turned on after  $5$  TU or  $291$  days and stayed on until  $13.5$  TU or  $785$  days, which results in  $\Delta V = 5.1$  km/s. Using the same initial parameters as above, but with the new thrust acceleration value, the total required  $\Delta V$  given by the algorithm is  $5.6$  km/s, with TOF =  $754.9$  days. The differences are  $de = 0.0012$  and  $di = 0.22$  degrees, while the corresponding angles are  $\alpha = 10$  degrees and  $taa = 145$  degrees. Although the calculations above only give a rough indication for the comparison with the optimized results, they still show that, even without a rigorous optimization process, the algorithm gives results that are similar to the optimized results from other low-thrust transfer methods.

In conclusion, the developed algorithm performs well provided that the TOF is not too large. Also, both small and large inclination changes can be modelled with good accuracy. The observed errors have different natures, and a summary of these possible sources of error is given below.

- The periodical variation of the true longitude is neglected for the analytical solution.
- The assumption that  $e = 0$  is only exact at the start of the transfer. Hereafter, the eccentricity will increase due to the thrust acceleration acting on the spacecraft.
- Within the code, several while-loops ensure that the solution converges to the desired result, e.g. the target  $u$  for the numerical propagation, or the target element for both analytical and numerical propagation. However, these are not always able to converge to the set tolerance, and therefore are terminated after a maximum number of loops. This introduces a variable inaccuracy which is difficult to quantify in general.
- The error in argument of latitude arising from the above error sources further deviates the results, as the switching times are dependent on this element. Differences will therefore result in difference thrusting periods, such that the change in elements is larger or smaller.
- In addition, for the computation of the switching time for the analytical solution, an approximate value for  $\Omega$  is used, which may cause the final  $u$  to deviate from the target  $u$ .



# 8

## Conclusions and Recommendations

The aim of this research was to develop an algorithm to analytically model low-thrust transfer orbits, with two constraints on the acceleration. The first one, bang-bang control, fixed the shape of the thrust profile by only allowing on-off thrusting. The second one implied that no radial thrust would be applied on the spacecraft, to reduce gravity losses. An analytical solution has been found to describe the motion of the spacecraft during the thrust arc. Section 8.1 discusses the main conclusions arising from this research, while Section 8.2 provides recommendations for future research.

### 8.1. Conclusions

For the derivation of the analytical solution for low-thrust transfer orbits, the modified equinoctial elements have been used. This set of coordinates is characterized by first-order differential equations, which makes the derivation significantly easier. Furthermore, these elements are free from singularities at zero eccentricity and zero inclination. Besides the low-thrust acceleration provided by the rocket engine, no other perturbations have been taken into account. Also, originating from the thrust constraints mentioned above, the radial thrust is set to zero. This was the starting point of the analytical derivation. The research question, as posed in the introduction, was:

*Is it possible to develop an analytical solution for low-thrust trajectories while assuming bang-bang control without gravity losses?*

If Lagrange's planetary equations are simplified by assuming that the eccentricity is zero, an analytical solution can indeed be found for low-thrust trajectories. This analytical solution has been implemented in an algorithm, which simulates bang-bang control thrust profiles by switching the thrust on and off at cleverly chosen points during the orbit.

Two sub-questions arised from the main research question:

- *What is the accuracy of the developed solution?*
- *To what extent is the developed solution applicable?*

The accuracy of the developed algorithm proved to be good. The differences have been assessed for steering angles ranging from 0 to 90 degrees and thrust arc angles ranging from 5 to 175 degrees. For a transfer of 10 years with a thrust acceleration of  $10^{-4}$  m/s<sup>2</sup>, an average relative difference of just 0.65% for the semi-major axis is perceived. The average difference for the eccentricity in this case is 0.006, while for the inclination it is 0.17 degrees. For the longitude of the ascending node and argument of pericenter the average errors are 0.045 and 4 degrees, respectively. The method failed however to make a good prediction of the argument of periapsis. Furthermore, it is noticed that as the thrust acceleration becomes higher, e.g.  $10^{-3}$  m/s<sup>2</sup>, the results become more inaccurate. This can be explained by a larger increase in elements, which also causes the eccentricity to deviate increasingly

from the assumption made. The same is true for a longer time of flight (TOF). As the time is increased from 2.5 to 10 years, less combinations of thrust arc angles and steering angles remain feasible.

With the addition of a stop criterion, the required  $\Delta V$  and TOF for different combinations of input parameters can be computed. The analytical results showed good correspondence with the numerical results, apart from some high errors that were noticed for the TOF. These have been attributed to the difference in switching times between the two methods, causing one method to arrive at the target value at the end of the final thrust arc, while the other achieves the final element at the beginning of the next; thus, an additional coast arc is inserted. This is also noticed in the final difference in  $u$ . In conclusion, the accuracy of the developed method is deemed to be fit for arriving at first-order guesses of an optimal solution.

The largest assumption that has been made to simplify the equations of motion directly influences the applicability of the method. Since zero eccentricity is assumed, the analytical solution only provides good results for relatively small eccentricities. Based on the comparison between the analytical and numerical methods, an upper limit of  $e = 0.2$  has been set. However, it is believed that a considerable range of mission design problems can still be achieved with the developed method, since there are several planetary bodies with orbits not exceeding this eccentricity. Moreover, it has been found that the accuracy of the method decreases if the time of flight increases. Therefore, the maximum time of flight needs to be restricted. From the results it could be concluded that a TOF of 30 years exceeds the applicable range of the method. Also, the planetary equations of the modified equinoctial elements do not offer a solution when the inclination is 180 degrees. Therefore, the algorithm should be stopped when a value for the inclination near this limit is achieved. Finally, the method did not yield accurate results for the argument of pericenter. However, since the eccentricities are assumed to be near-zero, this is not expected to form a large source of error for the final optimum result.

## 8.2. Recommendations

Although it has been proven that the developed method provides sufficiently accurate results, within certain limits, it still has to be implemented into an optimization scheme. The optimization process would then make a more rigorous search within the design space to arrive at the optimum solution. The design parameters include:

- the thrust acceleration  $f_{tot}$
- the steering angle  $\alpha$
- the thrust arc angle  $taa$
- the position of the switching points, determined by  $u_1$  and  $u_2$
- the maximum time of flight

In addition, the optimization could also be allowed to vary the steering angles and thrust arc angles. In the current method, these angles are fixed at the start of the simulation, and cannot be changed during the transfer. However, one could imagine cases where a change would be desirable. For example, if both a change in semi-major axis and inclination are required, a possible solution would be that the steering angle is mostly in-plane at the start, and gains an out-of-plane component as it reaches the target orbit. Moreover, if the change in inclination is small, the thrust arc angle can be reduced in the final stages of the transfer.

Since the method can not be used to directly constrain the solution to the boundary conditions, a forward targeting method should be used to arrive at the optimum. Two different parameters can be chosen to optimize, either the  $\Delta V$  or TOF, or a combination of these two. In addition, the differences between the achieved final elements and the target final elements should be minimized. This can be done by means of a penalty function. The weights are then varied depending on the requirements of the mission.

Finally, in the analysis of the developed method, only heliocentric transfers have been taken into account. However, the method is developed for a general transfer around any attracting body, requiring a different  $\mu$ . Interesting cases to further analysis would be transfers in Earth orbit, such as LEO-to-GEO transfers.

# Bibliography

- [1] G. P. Sutton and O. Biblarz. *Rocket Propulsion Elements*. John Wiley & Sons, ninth edition, 2017.
- [2] E. Y. Choueiri. A Critical History of Electric Propulsion: The First Fifty Years (1906-1956). *Journal of Propulsion and Power*, 20(2):193–203, 2004.
- [3] B. A. Conway. *Spacecraft Trajectory Optimization*. Cambridge University Press, 2010.
- [4] A. E. Petropoulos and J.M. Longuski. Automated Design of Low-Thrust Gravity-Assist Trajectories. *AIAA/AAS Astrodynamics Specialist Conference, AIAA Paper 2000-4033, Colorado*, pages 157–166, 2000.
- [5] P. De Pascale and M. Vasile. Preliminary Design of Low-Thrust Multiple Gravity-Assist Trajectories. *Journal of Spacecraft and Rockets*, 43(5):1065–1076, 2006.
- [6] B.J. Wall and B.A. Conway. Shape-Based Approach to Low-Thrust Rendezvous Trajectory Design. *Journal of Guidance, Control, and Dynamics*, 32(1):95–101, 2009.
- [7] B.J. Wall. Shape-Based Approximation for Low-Thrust Trajectory Optimization. *AIAA/AAS Astrodynamics Specialist Conference and Exhibit, Guidance, Navigation, and Control and Co-located Conferences, Hawaii*, 2008.
- [8] D.M. Novak and M. Vasile. Improved Shaping Approach to the Preliminary Design of Low-Thrust Trajectories. *Journal of Guidance, Control, and Dynamics*, 34(1):128–147, 2011.
- [9] E. Taheri and O. Abdelkhalik. Shape-Based Approximation of Constrained Low-Thrust Space Trajectories Using Fourier Series. *Journal of Spacecraft and Rockets*, 49(3):535–545, 2012.
- [10] O. Abdelkhalik and E. Taheri. Approximate On-Off Low-Thrust Space Trajectories Using Fourier Series. *Journal of Spacecraft and Rockets*, 49(5):962–965, 2012.
- [11] E. Taheri and O. Abdelkhalik. Fast Initial Trajectory Design for Low-Thrust Restricted-Three-Body Problems. *Journal of Guidance, Control, and Dynamics*, 38(11):2146–2160, 2015.
- [12] D. J. Gondelach and R. Noomen. Hodographic-Shaping Method for Low-Thrust Interplanetary Trajectory Design. *Journal of Spacecraft and Rockets*, 52(3):728–738, 2015.
- [13] A. E. Petropoulos. *A Shape-Based Approach to Automated, Low-Thrust, Gravity-Assist Trajectory Design*. PhD thesis, School of Aeronautics and Astronautics, Purdue University, West Lafayette, Indiana, 2001.
- [14] A. E. Petropoulos and J.M. Longuski. Shape-Based Algorithm for Automated Design of Low-Thrust, Gravity-Assist Trajectories. *Journal of Spacecraft and Rockets*, 41(5):787–796, 2004.
- [15] D. Izzo. Lambert’s Problem for Exponential Sinusoids. *Journal of Guidance, Control and Dynamics*, 29(5):1242–1245, 2006.
- [16] B. De Voogeleer. Automatic and Fast Generation of Sub-optimal and Feasible Low-Thrust Trajectories using a Boundary-Value Pseudo-Spectral Method. Master’s thesis, TU Delft Repository, Delft University of Technology, Delft, The Netherlands, August 2008.
- [17] A. A. Quarta and G. Mengali. Analysis of spacecraft motion under constant circumferential propulsive acceleration. *Acta Astronautica*, 105(1):278–284, 2014.
- [18] Z. Zhu, Q. Gan, X. Yang, Y. Gao. Solving fuel-optimal low-thrust orbital transfers with bang-bang control using a novel continuation technique. *Journal of Spacecraft and Rockets*, 137:98–113, 2017.

- [19] K. F. Wakker. *AE4874 Fundamentals of Astrodynamics. Lecture Notes*. Institutional Repository, Library, Delft University of Technology, The Netherlands, 2015.
- [20] H. D. Curtis. *Orbital Mechanics for Engineering Students*. Elsevier, 2005.
- [21] P. M. Sforza. *Theory of Aerospace Propulsion*. Elsevier, 2012.
- [22] H. J. Kramer. TET-1 (Technology Experiment Carrier-1). URL:<https://earth.esa.int/web/eoportal/satellite-missions/t/tet-1>. Accessed on 25 April 2018.
- [23] AMSAT-DL. AMSAT OSCAR-40. URL:<https://www.amsat-dl.org/p3d.html>. Accessed on 25 April 2018.
- [24] J. Climer. Boeing Defense, Space and Security, SES-15. URL:[http://www.boeing.com/resources/boeingdotcom/space/boeing\\_satellite\\_family/pdf/Bkgd\\_SES-15.pdf](http://www.boeing.com/resources/boeingdotcom/space/boeing_satellite_family/pdf/Bkgd_SES-15.pdf). Accessed on 25 April 2018.
- [25] D. Birschitzky et al. PEGASUS - An Austrian Nanosatellite for QB50. URL: <https://spacedatacenter.at/stg/img/PEGASUS%20European%20Geosciences%20Union%20FINAL%20Dissemination-1.pdf>. Accessed on 25 April 2018.
- [26] M.T. Domonkos, A.D. Gallimore, R.M. Myers, E. Thompson. Preliminary Pulsed MPD Thruster Performance. *AIAA*, (95-2674), 1995. 31st Joint Propulsion Conference and Exhibit.
- [27] AsiaSat Media Release. AsiaSat 9 fully operational at 122E. URL:<https://www.asiasat.com/sites/default/files/asiasat-9-operational-en.pdf>. Accessed on 25 April 2018.
- [28] R. Noomen. AE2-230-I Flight and Orbital Mechanics: Perturbations. Lecture Slides, December 9, 2015. TU Delft, The Netherlands.
- [29] C. Stover and E. W. Weisstein. Cartesian coordinates. From MathWorld—A Wolfram Web Resource. URL:<http://mathworld.wolfram.com/CartesianCoordinates.html>. Accessed on 6 March 2018.
- [30] E. W. Weisstein. Cylindrical coordinates. From MathWorld—A Wolfram Web Resource. URL:<http://mathworld.wolfram.com/SphericalCoordinates.html>. Accessed on 6 March 2018.
- [31] J. Ginsberg. *Engineering Dynamics*. Cambridge University Press, 2007.
- [32] M. J. H. Walker, B. Ireland and J. Owens. A set of modified equinoctial orbit elements. *Celestial Mechanics*, 36(4):409–419, 1985.
- [33] J.H. Jo, I.L. Park, N. Choe and M. Choi. The Comparison of the Classical Keplerian Orbit Elements, Non-Singular Orbital Elements (Equinoctial Elements), and the Cartesian State Variables in Lagrange Planetary Equations with  $J_2$  Perturbation: Part I. *Journal of Astronomy and Space Sciences*, 28(1):37–54, 2011.
- [34] L. C. Andrews. *Special Functions for Engineering and Applied Mathematicians*. Macmillan Publishing Company, tenth edition, 1985.
- [35] M. A. Abramowitz and I. A. Stegun. *Handbook of Mathematical Functions : with Formulas, Graphs, and Mathematical Tables*. Dover Publications, Inc., ninth edition, 1965.
- [36] N. N. Lebedev. *Special Functions and Their Applications*. Prentice-Hall, Inc., 1965.
- [37] F.G. Tricomi. *Integral Equations*. Courier Corporation, 1985.
- [38] J.J. Lissauer and I. de Pater. *Fundamental Planetary Science*. Cambridge University Press, 2013.